University of Alberta

Quantifying Greenhouse Gas Emissions from an Oil Sands Tailings Pond using Micrometeorological Flux Measurement Techniques

by

Casandra Brown

A thesis submitted to the Faculty of Graduate Studies and Research in partial fulfillment of the requirements for the degree of

Master of Science

Department of Earth and Atmospheric Sciences

Fall 2013
Edmonton, Alberta

Abstract

The focus of this thesis is the use of micrometeorological techniques to quantify the flux of trace gases from surface area sources to the atmosphere. In particular, it is an investigation into the feasibility of using such techniques, specifically the eddy covariance and inverse dispersion methods, as alternatives to the traditional flux chamber approach to measuring methane emissions from oil sands tailings ponds. Exploring such alternatives is of interest because these techniques effectively sample a larger surface area at higher temporal resolution than the flux chamber approach permits. This thesis shows the capability of the eddy covariance method in making flux measurements from tailings ponds, provided the flow is undisturbed and the flux footprint is over the source area of interest. Furthermore, it demonstrates the loss of accuracy incurred when the inverse dispersion method is applied in cases where site conditions deviate from the ideal assumed by the model.

Acknowledgements

I would like to sincerely thank my supervisors Dr. John D. Wilson and Dr. Zaher Hashisho for their supportive supervision of this program. Without their guidance, completion of this research project would not have been possible. I would also like to express my gratitude to Peter Carlson for his help in preparing for the field campaigns and with setting up the instruments at the oil sands site. Thanks are due to Alberta Environment and Sustainable Resource Development (AESRD) for funding this research and to the site operators for providing access to the sites for us to make our measurements.

Contents

List of Tables

List of Figures

List of Symbols

A	surface area covered by flux chamber
A_r	area bounded by contour
a	distance to downwind edge of isopleth
a_v	foreign gas broadening coefficient for water vapour relative to dry air
C_p	specific heat capacity of air
$C_{w\beta}$	cospectra for vertical velocity w and scalar concentration β
$C_{w\theta}$	cospectra for vertical velocity w and potential temperature θ
CF	flux correction factor
c	gas concentration
c_b	background gas concentration
c_E	gas concentration measured along eastern edge of test lagoon
c_{diag}	gas concentration measured along diagonal of test lagoon
c_{diag*}	expected gas concentration along diagonal of test lagoon
c_i	gas concentration in air entering flux chamber
$c_{LI-7700}$	gas concentration measured by LI-7700
c_{NW}	gas concentration measured by northwest laser gas detector
c_o	gas concentration in air leaving flux chamber
c_z	gas concentration at height z
d	maximum width of contour
e	distance to upwind edge of contour
f	flux footprint
f_i	normalized frequency ($f_i = nz/\overline{u}$, where $\overline{u}$ is mean velocity at height z)
f_p	normalized frequency ($f_p = np/\overline{u}$)
f_s	normalized frequency ($f_s = ns/\overline{u}$)
g	acceleration due to gravity
K_c	eddy diffusivity of gas
K_h	eddy diffusivity of heat
K_m	eddy diffusivity of momentum
k_v	von Karman constant (assumed equal to 0.4)
L	Obukhov length
N_p	total number of particles released from sensor in Lagrangian simulations
N_z	total number of heights measurements are made at
n	frequency
P	pressure
P_e	equivalent pressure
p	sensor path length
Q	flux

Q_E	latent heat flux
Q^{EC}	flux determined using eddy covariance technique
Q^{FC}	flux determined using flux chamber technique
Q^{FG}	flux determined using flux gradient technique
Q_H	sensible heat flux
Q^{ID}	flux determined using inverse dispersion technique
Q_L	flux of large lagoon
Q^{MB}	flux determined using mass balance technique
q	specific humidity
s	separation distance between two sensors
T	temperature
T_0	mean temperature of surface layer in Kelvin
T_s	sonic-derived temperature
T_i	transfer function, $i = s, p$ for sensor separation, scalar path averaging
T_*	temperature scale
t	time
$\overline{u}$	mean horizontal velocity, post-rotation
u_z or $u(z)$	wind component in x-direction at height z
u_*	friction velocity
V	volume of flux chamber head space
v	flux chamber volume flow rate
$\overline{v}$	mean wind component in y-direction
w	vertical wind component
w_0	vertical touchdown velocity
x	fetch
x_d	distance to the point where the contour is widest
x_m	distance to the maximum source location
$\overline{x_v}$	mole fraction of water vapour
z	height above the surface
z_0	surface roughness length

β	mean horizontal wind direction
Δy	horizontal extent of measurement plane (source width)
δ	depth of the atmospheric boundary layer
ζ	stability parameter, z/L
θ	rotation angle to set $\overline{v} = 0$
κ	corrects for spectroscopic effects of T, P, x_v
κ_T	rate of change of κ with T at constant $\overline{P_e}$
κ_{P_e}	rate of change of κ with P_e at constant $\overline{T}$
μ	ratio of dry air to water vapour molecular weight
ρ	air density
ρ_c	measured methane mass density, before correction
ρ_d	mass density of dry air
ρ_v	water vapour density
σ	ratio of water vapour mass density to dry air mass density
σ_i	standard deviation of velocity components, $i = u$, v, w
σ_β	standard deviation in wind direction

τ_0	surface stress
ϕ	rotation angle to set $\overline{w} = 0$
φ	dimensionless MO universal similarity function

Chapter 1

Introduction

1.1 Background Information

This thesis focuses on the use of micrometeorological techniques to quantify methane emissions from well defined area sources into the atmosphere, specifically the application of these techniques to quantify the flux over an oil sands tailings pond. Methane (CH_4) is a greenhouse gas and as such it has the capacity to absorb a fraction of the infrared radiation emitted by the surface that would otherwise escape into space. It is one of the most important greenhouse gases resulting from human activities in terms of its global warming potential (GWP) (Yusuf et al., 2012).[1] Methane has a 100 year global warming potential of 25 times that of carbon dioxide (CO_2) (IPCC, 2007). This means that 1 kg of methane has the same impact on climate as 25 kg of carbon dioxide, over a 100 year period. In addition to the direct effect methane has on climate through its role as a greenhouse gas, several indirect radiative effects of CH_4 emissions have been identified. Methane enhances its own lifetime through its impact upon the concentration of the hydroxyl radical (OH), leads to changes in tropospheric ozone, enhances stratospheric water vapour levels, and produces carbon dioxide (IPCC, 2007). The GWP reported here includes the first three of these indirect effects.

---

[1] The global warming potential is a useful metric for comparing the radiative forcing of greenhouse gases over a specified period from a unit mass pulse emission (IPCC, 2007).

Anthropogenic sources of atmospheric methane include, but are not limited to, rice agriculture, livestock, landfills and waste treatment, and fossil fuel mining and distribution. Globally, natural methane emissions are dominated by methanogenesis in wetlands (IPCC, 2007). Present atmospheric levels of CH_4 are unprecedented in at least the last 650,000 years, with the global atmospheric concentration reaching 1774 ppb in 2005 (IPCC, 2007).

The Alberta Ambient Air Data Management System (AAADMS), more commonly known as the CASA Data Warehouse, is a central repository for ambient air quality data collected in Alberta. Air quality is monitored by a network of stations across Alberta operated by Alberta Environment, air quality management zones, Environment Canada, and industry stations. Stations reporting methane concentration measurements for the year 2012 are limited to central Alberta. Continuous monitoring of hydrocarbons (like CH_4) is performed by a hydrogen flame ionization detector and data is stored in one-hour time blocks. Typical maximum and minimum diurnal methane levels differ by 0.2-0.3 ppm, with concentration typically higher at night. The annual average atmospheric methane concentration reported by these stations was 1.93 ppm in 2012, with concentrations highest in the winter and lower in the summer.

Since the 1700's, anthropogenic activities, particularly those related to fossil fuel use, agriculture, and waste disposal, have more than doubled atmospheric methane concentrations (Wuebbles and Hayhoe, 2002). A period of near-zero growth in methane concentration from 1999 to 2006 (implying that emissions approximately matched removals), has been followed by a renewed growth in methane levels since 2007 (Schneising et al., 2011). Removal of methane is primarily a result of atmospheric oxidation by the hydroxyl radical in the troposphere. Other minor sinks include reaction with free chlorine, destruction in the stratosphere, and soil uptake (IPCC, 2007). Reaction with the hydroxyl radical is responsible for almost 90% of the removal of CH_4, making the concentration of OH the most important determinant for the removal rate of methane from the atmosphere (Wuebbles and Hayhoe, 2002). Hydroxyl concentrations are affected by both the direct emission of methane and by its oxidation products, especially carbon monoxide (CO). CH_4, CO, and OH are involved in a positive chemical feedback cycle wherein a rise in CH_4 levels reduces OH and increases CO. The carbon monoxide produced by the oxidation of CH_4 will in turn be oxidized by OH, further decreasing OH levels. This feedback cycle is outlined in the following chemical reactions:

$$CH_4 + OH \rightarrow CH_3 + H_2O \rightarrow \ldots CO + products$$

$$CO + OH \rightarrow CO_2 + H$$

Increasing methane emissions can lead to an overall decrease in the oxidizing capacity of the troposphere, thereby slowing the removal of methane and leading to a build-up of methane concentration (IPCC, 2007).

It is estimated that fugitive methane emissions from the oil and gas sector (including the oil sands) make up 5.2% of the total greenhouse gas emissions from Canada (Hayes, 2004). North-eastern Alberta has the largest oil sands reserves in the world, with an estimated 2.5 trillion barrels of recoverable bitumen (Penner and Foght, 2010). Each cubic metre of oil sands mined produces about 4 m^3 of slurry waste, which must be held on site because the companies operate under a zero-discharge policy (Fedorak et al., 2002). This slurry is deposited into tailings ponds to mature, through settling of solids. The resulting mature fine tailings comprise slightly alkaline water, fines (silts and clays), unrecovered bitumen, and solvent (used for the extraction and transportation of bitumen) (Siddique et al., 2008). As of 2011, more than 170 km^2 of the oil sands region is covered by tailings ponds (Siddique et al., 2011). What little knowledge exists as to the emission of greenhouse gases, such as methane, from oil sands tailings ponds is currently based on limited snapshots and localized measurements. Traditional methods of measuring methane fluxes involve the use of static chamber techniques. Mildred Lake Settling Basin (MLSB), the oldest and largest of Syncrude Canada Ltd.'s mature fine tailings deposits, contains more than 400 million m^3 of fine tailings. Methane emission rates from the surface of MLSB have been measured in situ using isolation flux chambers. These emission rate estimates ranged from approximately 43 million L day^{-1}

(3.0 x 10^4 kg day^{-1}, 1.2 x 10^{-2} kg m^{-2}day^{-1}) in 2000 to 3-30 million L day^{-1} (0.2-2.1 x 10^4 kg day^{-1}, 0.9-8.6 x 10^{-3} kg m^{-2}day^{-1}) in 2007 (Siddique et al., 2008). The flux chamber sampling method samples the air at a point in space over a short time frame. This approach involves placing a small chamber on the pond, which disturbs the surface and decouples it from the natural atmosphere, potentially impacting the processes controlling the flux being measured. Estimates of emissions based on this method of sampling are compromised by the heterogeneity of the source due to the spatial and temporal variability of the emissions. For this reason, it is of interest to explore other means of measuring emissions that would sample a larger area at higher temporal resolution, without interfering with the surface. Micrometeorological flux measurement techniques are in principle ideally suitable in these respects.

1.2 Objectives of Research

The eddy covariance technique was used in a preliminary field campaign at a biosolids lagoon to measure fluxes of methane, allowing for familiarization with the sensors and methodology involved with this technique. It also provided an opportunity to identify potential limitations with the methodology that needed to be improved upon for future field campaigns. The experience gained was later applied to a second field campaign at an oil sands tailings pond, which served as the main objective of this research project. Eddy covariance measurements of methane flux from the tailings pond were accompanied by the analysis of methane concentration measurements using inverse dispersion to provide independent estimates of the source strength. These measurements were carried out so as to explore the feasibility of using a micrometeorological flux measurement technique as an alternative to the traditional flux chamber approach to trace gas flux measurements from tailings ponds.

1.3 Thesis Outline

The first chapter of this thesis has provided background information on methane emissions from Canada and the oil sands tailings ponds in particular. In Chapter 2, a summary of the atmospheric boundary layer and details of various flux measurement techniques are given, including the eddy covariance and inverse dispersion methods that were used in the research reported in this thesis. Chapter 3 gives the specifics of the instrumentation and methodology used during the field campaigns. Chapter 4 gives the results of the preliminary field campaign at the biosolids lagoon that was used as a learning experience in preparation for the campaign at the oil sands tailings pond. The results of the field campaign at the oil sands tailings pond are discussed in Chapter 5.

Chapter 2

Relevant Micrometeorological Theory

This chapter briefly covers the theory of the atmospheric boundary layer (ABL), across which there is a constant exchange of mass, momentum and energy between the surface and the free troposphere. The flux measurement techniques that are used in the study of this exchange in the lowest layer of the ABL are described, including the two methods used in this thesis: eddy covariance and inverse dispersion.

2.1 Atmospheric Boundary Layer & Surface Layer

The atmospheric boundary layer is the layer directly above the ground surface in which exchange of momentum, heat, and mass takes place rapidly (i.e., on a timescale with an order of magnitude of about 10 minutes) between the surface and the overlying atmosphere (Stull, 1988). In the ABL, air flow is generally turbulent. Vertical transport is due to eddies, ranging in size from just a few millimetres to something of the order of the depth of the boundary layer. The rates of transfer and mixing due to turbulence are many orders of magnitude greater than the rate of molecular diffusion (that is to say, we are concerned here to measure convective fluxes). Atmospheric properties, such as temperature, velocity, and scalar concentrations, fluctuate quickly. Due to these fluctuations, of necessity statistical measures must be used to describe the turbulence structure of the flow and the distribution of properties such as (for instance) methane concentration or methane flux. Standard deviations and variances are simple measures of the fluctuations. The ratio of standard deviations of velocity fluctuations to the mean wind speed gives the turbulence intensities, which are measures of the relative fluctuation levels in different directions. Covariances of components of the wind and scalars, such as temperature or gas concentration, give the turbulent convective fluxes of momentum, heat, etc. (Arya, 2001).

The atmospheric boundary layer can be notionally subdivided into an outer layer and an inner layer. The outer layer consists of generally weakly sheared flow whose character is scarcely affected by the specific structure of the underlying surface, whereas the flow in the inner layer (or surface layer) is very strongly influenced by the surface characteristics. The surface layer is the region at the bottom of the boundary layer within which turbulent fluxes vary with height by less than (nominally) 10% of their surface values (Stull, 1988), leading to the layer frequently being termed the "constant flux layer" or "constant stress layer". Provided the surface layer is in a state of horizontal homogeneity (where statistical properties are constant on horizontal planes, and therefore vary only with height and time), the mean flow and turbulence statistics of this layer are adequately described by the Monin-Obukhov Similarity Theory.

2.2 Reynolds Averaging

A common approach to studying turbulence is to separate variables, such as temperature (T) and vertical wind speed (w), into their mean and fluctuating parts: $T = \overline{T} + T'$ and $w = \overline{w} + w'$ (where the averages are denoted by overbars and the fluctuating components by primes). By definition, the mean of the fluctuation is zero ($\overline{w'} = 0$). According to the Reynolds averaging rules the average of the product of two variables is the product of the averages plus the average of the product of the fluctuations:

$$\overline{wT} = \overline{(\overline{w} + w')(\overline{T} + T')} = \overline{w}\overline{T} + \overline{w'T'}.$$

The second term on the right hand side is the covariance between the vertical velocity fluctuation and the temperature fluctuation, and represents the vertical turbulent kinematic heat flux density.

2.3 Monin-Obukhov Similarity Theory

As described in Arya (2001), the Monin-Obukhov Similarity Theory (MOST) provides a suitable framework for describing the mean and turbulence structure of the horizontally-homogeneous surface layer. MOST is applicable in the layer $z_0 \ll z \ll \delta$, where z_0 is the surface roughness length and δ is the depth of the boundary layer. The mean flow and turbulence characteristics of a horizontally homogeneous surface layer are assumed to be governed by four independent variables: the height above the surface (z), the surface drag (τ_0/ρ), the surface kinematic heat flux ($\overline{w'T'} = Q_H/(\rho C_p)$), and the buoyancy parameter g/T_0, where g is the acceleration due to gravity and T_0 is the mean Kelvin temperature of the layer. One independent dimensionless combination can be made of the four independent variables, the stability parameter:

$$\zeta = z/L \tag{2.1}$$

where L is the Obukhov length given by:

$$L = \frac{-u_*^3}{k_v (g/T_0)\overline{w'T'}} \tag{2.2}$$

k_v is the von Karman constant ($k_v = 0.4$, dimensionless), included in the definition of L by convention. L is negative in unstable conditions, positive in stable conditions, and infinite at neutral stratification, thus the range in values for the stability parameter is from $-\infty$ to ∞. In magnitude, $|L|$ represents the thickness of the layer near the surface in which shear or friction effects are important.

From the governing parameters, the following characteristic scales of length, velocity, and temperature are used in the Monin-Obukhov similarity theory to form dimensionless groups:

$$\begin{aligned}&\text{Length scales: } z \text{ and } L\\ &\text{Velocity scale: } u_* = \sqrt[4]{\overline{u'w'}^2 + \overline{v'w'}^2}\\ &\text{Temperature scale: } T_* = -Q_H/\rho C_p u_*\end{aligned}$$

The similarity prediction of MOST is that any mean flow or averaged turbulence quantity, when normalized by some combination of the above-mentioned scales, is a unique function of the stability parameter. For example, the vertical gradient in mean wind speed can be expressed as

$$\frac{k_v z}{u_*}\frac{\partial \overline{u}}{\partial z} = \varphi_m\left(\frac{z}{L}\right) \tag{2.3}$$

where $\varphi_m({}^z/_L)$ is the dimensionless MO universal similarity function and (again) the von Karman constant is included out of convenience such that $\varphi_m(0) = 1$. This expression for the gradient in mean wind can be used to determine the flux of momentum if the form of the dimensionless function (φ_m) is known.

Determination of this function has been the subject of a number of major micrometeorological flux gradient experiments. The analysis by Dyer and Bradley (1982) of the International Turbulence Comparison Experiment (ITCE) recommends the following form for the similarity function in unstable stratification

$$\varphi_m = (1 - 28{}^z/_L)^{-1/4}. \tag{2.4}$$

In stable stratification, the result of Webb (1970) is commonly used:

$$\varphi_m = 1 + 5{}^z/_L. \tag{2.5}$$

Integration of the expression for the gradient of mean wind with respect to height gives the wind profile:

$$\overline{u}(z) = \frac{u_*}{k_v}\left[\ln\frac{z}{z_0} - \psi_m\left(\frac{z}{L}\right) + \psi_m\left(\frac{z_0}{L}\right)\right] \tag{2.6}$$

where ψ_m is another similarity function given in terms of φ_m as:

$$\psi_m = 2\ln\left(\frac{1+\varphi_m^{-1}}{2}\right) + \ln\left(\frac{1+\varphi_m^{-2}}{2}\right) + 2\arctan\left(\varphi_m^{-1}\right) + \frac{\pi}{2}. \tag{2.7}$$

The above equations allow for the computation of the variation in mean wind speed with height, and similar reasoning gives rise to profile laws for other turbulence statistics.

MOST plays a significant role in the determination of source strength when using the inverse dispersion technique (described in Chapter 2.4.3). This technique involves the estimation of source strength from a measured concentration rise, requiring the computation of an ensemble of particle trajectories from each concentration sensor to the source. These paths must be computed such that they reflect the true wind statistics in the layer through which the particles travel. MOST relationships are unreliable in extreme stabilities and low winds (Flesch et al., 2005). Flesch et al. (2007) suggest that the horizontally homogeneous surface layer is well-described by MOST provided that $u_* \geq 0.15$ m s^{-1} and $|L| \geq 10$ m, but this is not to say that profiles during intervals with smaller u_*, $|L|$ necessarily and always deviate from MOST.

2.4 Flux Measurement Techniques

Numerous techniques are available for the measurement of the exchange of heat, momentum, and trace gases in the surface layer. The choice of which technique to apply is dependent on the site conditions and the instruments available. Methods capable of making measurements of fluxes of trace gases with concentration c between the surface and the atmosphere are described in the following sections in order of landscape scale. Flux chambers, representing the smallest scale of measurements, are the most commonly used. Mass balance techniques are suitable for small, well-defined area sources, as is the inverse dispersion method. Techniques suitable for making flux measurements on large landscape scales, specifically the flux gradient and eddy covariance approaches, are described. This thesis focuses on the use of the eddy covariance and inverse dispersion techniques to measure trace gas fluxes from an oil sands tailings pond, as possible alternatives to the more traditional flux chamber approach.

2.4.1 Flux Chambers

Flux chambers represent the smallest scale (< 1 m^2) for measuring trace gas fluxes. This technique has a simple operating principle, is highly sensitive, and of low cost. The general principle is to restrict the volume of air within which gas exchange occurs so as to magnify the changes in concentration of gas in the head-space of the chamber (Denmead, 2008). Chambers are classified according to whether they are open to the atmosphere (flow-through chambers) or are closed chambers.

In flow-through chambers, a constant flow of outside air is maintained through the head-space of the chamber and the concentration difference between the air entering and leaving the head-space is measured. The flux of gas at the surface (Q^{FC}) is calculated according to (Denmead, 2008):

$$Q^{FC} = v(c_o - c_i)/A \tag{2.8}$$

where v is the volumetric flow rate, c_o is the gas concentration in the air leaving the chamber, c_i is the gas concentration of the air entering the chamber, and A is the surface area covered by the chamber.

In closed chambers, replacement of air in the head-space is minimal and the gas concentration continuously increases. The rate of increase in gas concentration is monitored and the flux is calculated according to (Denmead, 2008):

$$Q^{FC} = (V/A)\left(\frac{dc}{dt}\right) \tag{2.9}$$

where V is the volume of the head-space and t is time.

The small surface area measured by flux chambers does not allow for the spatial variability of trace gas fluxes from large area sources to be accurately measured. This is an issue for large source areas like the oil sands tailings pond of this research project, which covered an area of ~4 km^2. As such, an alternative technique that would result in flux measurements representative of a larger surface area is of interest.

2.4.2 Mass Balance Technique

In the mass balance approach, the source strength is determined by the upwind-downwind difference in the horizontal flux of mass (Wilson et al., 2001). Required data includes the profile of gas concentration on the downwind boundary of the source area, the wind speed profile, and the background concentration (or concentration profile). The mean horizontal flux of the emitted gas (Q_h^{MB}) at any height z on the downwind boundary is given by (Denmead, 2008):

$$Q_h^{MB} = \overline{u_z[c_z - c_b]} \tag{2.10}$$

where u_z is the horizontal wind speed at height z, c_z is the measured gas concentration at height z downwind of the source, c_b is the background concentration of the gas (assumed height independent to derive Eq. 2.10), and the overbar denotes a time average. The total emission rate (Q^{MB}) is then given by (Gao et al., 2009):

$$Q^{MB} = \Delta y \int_0^h \overline{u_z[c_z - c_b]} dz \tag{2.11}$$

where h is the top of the cloud of emitted gas, which depends on atmospheric stability and distance travelled by the wind, and Δy is the horizontal extent of the measurement plane (i.e., the source width). In practice, the concentration and wind speed measurements are made at multiple discrete heights downwind of the emitting area at a sufficient number of heights to define the concentration profile. The total emission rate is calculated using the following equation:

$$Q^{MB} = \sum_{i=1}^{N_z} \overline{u_i}(c_{zi} - c_b)\Delta z_i \tag{2.12}$$

where N_z is the total number of heights that measurements are made at. Figure 2.1 gives a schematic representation of the experimental set-up in the mass balance experiment of Gao et al. (2009).

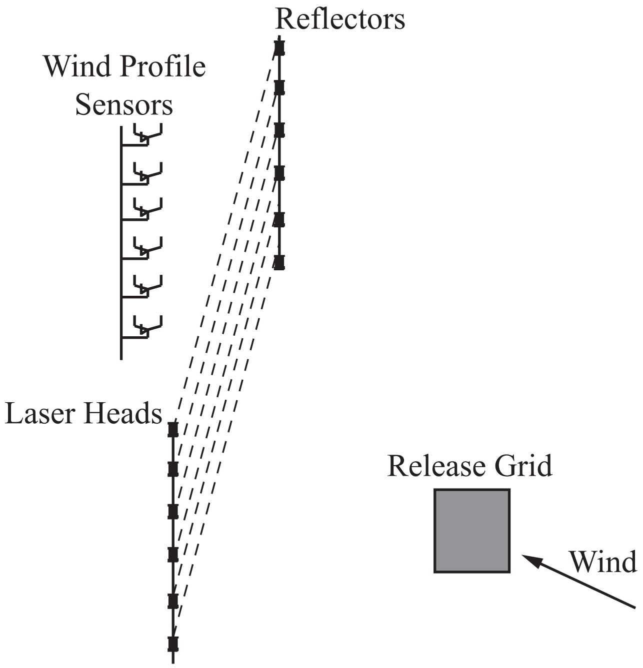

Figure 2.1: Schematic representation of source-laser set-up in the mass balance experiment of Gao et al. (2009) with multiple laser paths at a location downwind of the source.

A key advantage to using this method is that it is insensitive to any inhomogeneity of the source, and instruments can be simple and slow response. This technique is suitable for measuring emissions from small, well-defined source areas (Denmead, 2008), but would not be feasible for the field site of this thesis due to the large size of the source, requirement of many instruments to define the concentration and wind profiles, and site restrictions on the possible locations for instruments.

2.4.3 Inverse Dispersion Technique

The inverse dispersion method infers an unknown flux (Q^{ID}) from a measured mean concentration rise ($\overline{c}$) of the gas of interest. The ratio of the horizontal wind speed ($\overline{u}$) and this concentration rise to the source strength results in a dimensionless quantity (n):

$$n \equiv \frac{\overline{uc}}{Q^{ID}}. \tag{2.13}$$

A theoretical value for this dimensionless quantity (n^t) can be computed using any suitable theory or model of atmospheric transport and dispersion in conjunction with meteorological measurements defining the wind field. The backward Lagrangian stochastic method predicts the ratio of concentration to surface flux by tracing particle trajectories backwards from the sensor to the source area and the touchdowns on the ground surface and corresponding vertical velocities are recorded. Flesch et al. (1995) give

$$n^t = \frac{1}{N_p} \sum \left| \frac{2}{w_0/\overline{u_z}} \right| \tag{2.14}$$

where the summation refers to the touchdowns occurring within the source boundary, N_p is the total number of particles released from the sensor, and the vertical touchdown velocities (w_0) have been normalized by the mean horizontal wind speed measured at height z ($\overline{u_z}$, height chosen is arbitrary). Once n^t has been calculated for the given conditions and source area geometry, the flux can be calculated using Eq. 2.13 with the measured gas concentration and horizontal wind speed. The background concentration of the species being measured must be subtracted from the measured gas concentration prior to determining the emission rate.

There are two key assumptions underlying this approach: the emission rate is uniform within the (known) perimeter of the source, and the flow is horizontally homogeneous (Flesch et al., 1995). When these criteria are not met, some error in the flux estimate will result. There are multiple practical advantages to this approach, including that only one observation of the horizontal wind speed and gas concentration is necessary and slow response sensors can be used, unlike in the eddy covariance method (Flesch et al., 1995).

2.4.4 Flux Gradient Technique

The flux gradient technique determines the vertical transport of gas in the surface layer by measuring the associated vertical mean concentration gradient, and multiplying it by the eddy diffusivity of the gas, K_c (Laubach and Kelliher, 2004):

$$Q^{FG} = -K_c \frac{\partial \overline{c}}{\partial z} \tag{2.15}$$

where Q^{FG} is the turbulent convective flux ($\overline{w'c'}$) of the concentration c at height z. This method requires an estimate of K_c. According to some published interpretations of flux gradient experiments designed to test MOST (Dyer, 1974), the diffusivities of momentum, heat, and gas concentration are equal in neutral stratification (i.e., $K_m = K_h = K_c$). At stabilities other than neutral, the diffusivities are related through the use of the universal stability functions (ϕ_m, ϕ_h, ϕ_c) that are functions of the stability parameter z/L (Laubach and Kelliher, 2004). Using this theory, K_c can be inferred from the diffusivity of another variable for which flux and gradient can both be measured (e.g., heat flux and temperature gradient). The gas flux is then given by (Laubach and Kelliher, 2004):

$$Q^{FG} = \frac{-k_v u_* z}{\phi_c(z/L)} \frac{\Delta \overline{c}}{\Delta z} \tag{2.16}$$

where the concentration gradient in Eq. 2.15 is approximated by a finite difference in mean concentration between two measurement heights, z_1 and z_2, as $\Delta \overline{c}/\Delta z$ (where $\Delta z = z_2 - z_1$) and z is the intermediate height between z_1 and z_2. By limiting the measurement heights to within the surface layer, the fact that the concentration footprints of z_1 and z_2 differ does not matter. The flux gradient method requires a large fetch upwind, limiting its applicability.

2.4.5 Eddy Covariance Technique

The eddy covariance approach to flux measurements assumes stationary, horizontally homogeneous flow over a horizontally uniform surface that uniformly releases a gas whose concentration is given by $c = c(x, y, z, t)$, such that the mean vertical convective flux density is

$$Q^{EC} = \overline{wc} \tag{2.17}$$

where w is the vertical wind speed. Since wind speed, temperature, and gas concentration are inherently turbulent, these variables need to be regarded as the sum of their mean and fluctuating parts. Applying this to vertical wind speed and concentration gives

$$w = \overline{w} + w',$$
$$c = \overline{c} + c'.$$

Eq. 2.17 can then be rewritten as

$$Q^{EC} = \overline{wc} + \overline{w'c'}. \tag{2.18}$$

So, the total flux of any scalar is the sum of a component carried by the mean wind and an eddy flux (Moncrieff et al., 1997). With the assumption that the mean vertical velocity is zero over the averaging period, the vertical flux of gas is given by

$$Q^{EC} = \overline{w'c'}. \tag{2.19}$$

(Corrections to this formula will be specified below.)

The eddy covariance technique requires fast response sensors that can detect very small changes in gas concentration and have a small sampling volume. The upwind area contributing to the measured flux must be small enough so that the flux measured pertains only to the area of interest and not other nearby sources. This is the flux footprint problem discussed in Chapter 2.5. If the assumptions of this technique hold, it is the most direct and accurate approach to flux measurement. Later in this thesis, practical refinements to the eddy covariance technique will be outlined.

2.5 Flux Footprint

When flux measurements are made at an elevated point, the upwind source area (footprint) sensed by the instruments must be determined. The flux footprint f relates the vertical flux measured at height z_m, $Q(x, y, z = z_m)$, to the spatial distribution of the surface flux, $Q(x, y, z = 0) = Q_0(x, y)$ (Horst, 1999):

$$Q(x, y, z_m) = \int_{-\infty}^{\infty} \int_{-\infty}^{x} Q_0(x', y') f(x - x', y - y', z_m) dx' dy' \tag{2.20}$$

where the separation between the measurement point and the site of each elemental surface emission in the streamwise direction is $x - x'$ (with the wind blowing in the positive x-direction) and in the crosswind direction this separation is $y - y'$. The degree to which any source upwind of the measurement point contributes to the measured flux varies with the distance from the source, the elevation of the observation, as well as with characteristics of the turbulent boundary layer and atmospheric stability (Schuepp et al., 1990). Schmid (1994) provides a parameterized model of the 50% source area boundary of a scalar flux. The area within the 50% contour contributes 50% of the measured flux. By specifying the atmospheric stability (i.e., unstable or stable), the dimensions of the 50% source area can be determined (see Appendix C-1 for details). Hsieh et al. (2000) developed an equation for determining the 90% flux fetch, or upwind range of the surface contributing 90% of the measured flux (the other 10% originating from points even farther upstream). It was found that the fetch was a function of the measurement height, the roughness length, and the atmospheric stability (see Appendix C-2 for details).

Chapter 3

Methodology

3.1 Instrumentation

3.1.1 Eddy Covariance Instruments

The eddy covariance system comprised: a 3-D sonic anemometer (CSAT3; Campbell Scientific, Logan, UT, USA), an LI-7700 CH_4 open-path gas analyzer (LI-COR Biosciences, Lincoln, NE, USA), an LI-7500A CO_2/H_2O open-path gas analyzer (LI-COR Biosciences), and a temperature and relative humidity probe (HMP155A; Vaisala Inc., Finland), interfaced to a datalogger (CR3000 micrologger; Campbell Scientific).

The CSAT3 sonic anemometer measures all three velocity components of the wind and temperature, averaged along its 10 cm path, up to about 20 times per second. It measures the speed of sound in air using the difference in time it takes for an ultrasonic signal to travel the same path in opposite directions. This manifested travel time is the speed of sound in static air plus or minus the speed of the wind. The speed of sound in static air depends largely on the temperature, and to a lesser extent, on humidity. The "sonic temperature" can also be calculated from the speed of sound measured by the anemometer, and differs from the true temperature by a small amount that relates to humidity.

The LI-7700 is an open-path CH_4 gas analyzer that provides methane concentration measurements with frequencies up to 40 Hz. The air temperature in the sampling path and fast atmospheric pressure are also measured. The LI-7700 uses wavelength modulation spectroscopy to make high speed, precise measurements, with RMS noise of 5 ppb (c.f. ambient mean concentration $\sim$ 2 ppm) at 10 Hz in typical ambient CH_4 concentration (LI-COR, Inc., 2010). The analyzer employs a Herriott cell with a 0.5 m length and a 30 m folded optical path length in an open configuration (McDermitt et al., 2011). The laser signal strength, reported as a dimensionless number called RSSI (Received Signal Strength Indicator) is continuously monitored at the detector. This allows for measurement quality to be monitored and considered during post-processing of data, and provides a means to determine when the sensor mirror needs to be cleaned with the LI-7700's self-cleaning mechanism.

The LI-7500A is an open-path infrared CO_2/H_2O gas analyzer. This instrument makes fast carbon dioxide and water vapour density measurements, with RMS noise of 0.11 ppm for CO_2 and 0.0047 ppt for H_2O measurements at 10 Hz (LI-COR, Inc., 2009). The LI-7500A uses nondispersive infrared (NDIR) detection and provides data outputs with frequencies up to 40 Hz.

With the eddy covariance technique, the gas density measurements made by these gas analyzers are used in conjunction with the sonic anemometer wind speed measurements to determine the fluxes of CH_4, CO_2, and H_2O, as described in Chapter 2.4.5.

3.1.2 Open-path Infrared Laser Gas Detectors

The open-path, infrared laser gas detectors (Boreal Laser's GasFinder 2.0) use an integrated transmitter/receiver unit and a remote passive reflector (placed up to hundreds of metres from the source) to measure the line average concentration of an absorbing gas, such as methane. The output interval is adjustable (here the interval was set at about 5 seconds). These concentration measurements can be combined with atmospheric conditions (atmospheric stability, friction velocity, and wind direction) measured by a sonic anemometer, along with the (presumed) perimeter of the source area, to get an estimate of the emission rate from the source using the inverse dispersion method described in Chapter 2.4.3 and the *WindTrax* software (described below).

Application of Inverse Dispersion Method: *WindTrax*

The software *WindTrax*, developed by Thunder Beach Scientific (B. Crenna), is a GUI that simulates the turbulent transport of trace gases in the atmospheric surface layer over a short range using a Lagrangian stochastic model. A Lagrangian stochastic model describes the paths of fluid particles in turbulent flow, based on knowledge of the velocity statistics (Wilson and Sawford, 1996). Lagrangian models follow individual particles along their paths through the air. This differs from Eulerian models, which perform calculations at fixed locations in space. The term "stochastic" implies that the model mimics the random, turbulent motion of the atmosphere. The "well-mixed condition", described by Thomson (1987), determines the values for several coefficients in a generalized Langevin equation that will ensure the computed ensemble of trajectories is consistent with the measured Eulerian velocity statistics (which, in the context of this thesis, were provided by a sonic anemometer and height-extrapolated using MOST). The well-mixed condition states that the model must ensure that if initially the particles are well-mixed (in velocity and position), they remain well-mixed.

WindTrax allows one to calculate both the unknown flux from sources emitting these gases and the unknown concentration in the vicinity of the sources. A satellite image of the field site is used to provide a background for drawing sources and positioning sensors, which are connected to an input data file containing concentration data and meteorological information. An output data file is connected to store the desired results, such as the unknown flux or unknown concentration. Each line of data in the input file represents one averaging interval and generates one line of results in the output file. In order to calculate the unknown flux and/or concentrations, *WindTrax* requires information describing the atmospheric surface layer. The necessary atmospheric inputs include: the surface roughness length z_0, the friction velocity u_*, the Obukhov length L, and the mean horizontal wind direction β. Observations of other wind statistics (σ_u, σ_v, σ_w) can also be provided if they are available, otherwise the program estimates them using MOST formulae. If the concentration was measured in mixing ratio units (ppm), mean air temperature and pressure are also required inputs.

To perform the simulation and deduce an emission rate or rates, there must be at least as many known concentration measurements c_i as there are unknown fluxes Q_j. If the number of concentration measurements is less than the number of unknown sources, the problem is "under-determined" and cannot be solved. If the opposite is true (there are more concentration measurements than unknown sources), the problem is "over-determined" and can be solved to obtain several different estimates of the flux. In this case, *WindTrax* gives a solution that will be the "best fit in the least squares sense." When the number of known concentrations is equal to the number of unknown sources, *WindTrax* solves the following system of equations for the unknown quantities:

$$\begin{aligned} a_{11}Q_1 + a_{12}Q_2 + \cdots + a_{1n}Q_n + c_b &= c_1 \\ a_{m1}Q_1 + a_{m2}Q_2 + \cdots + a_{mn}Q_n + c_b &= c_m \end{aligned} \tag{3.1}$$

where the subscripts m and n are the number of concentration measurements and unknown source strengths, respectively, c_b is the background concentration, and the coefficients a_{ij} relating fluxes Q_j to measured concentrations c_i are obtained from the particle models.

3.2 Eddy Covariance Post-Processing Corrections

A program was written in R to perform post-processing of the eddy covariance data to refine or correct the eddy flux. The code for this program is given in Appendix A and specific details of the corrections applied are given in Appendix B. A summary follows.

A coordinate rotation was applied to correct for sonic anemometer tilt using the double rotation method, as described in Wilczak et al. (2001). This correction must be applied because in the field the sonic anemometer cannot be leveled perfectly so as to ensure that the vertical axis is always perpendicular to the mean wind streamline. Instead, the vertical wind speed signal is liable to be contaminated by the other two wind components. Frequency response corrections were applied to compensate for the flux losses at different frequencies of turbulent transport (Moore, 1986) resulting from sensor separation and finite path length of the gas sensors. The WPL density correction was applied to the data to account for fluctuations in temperature and water vapour, which affect the measured gas fluctuations (Webb et al., 1980). A correction to account for the use of the sonic virtual temperature that is derived from the measurement of the speed of sound by the sonic anemometer (Schotanus et al., 1983) was also applied. The LI-7700-specific corrections were applied to the methane concentration measurements made by the LI-7700 to adjust the spectroscopic light absorption measurements for correlated fluctuations in temperature and water vapour density (LI-COR, Inc., 2010).

Chapter 4

Preliminary Field Campaign at Biosolids Lagoon

Eddy covariance measurements of CH_4 and CO_2 fluxes were made during a brief preparatory campaign at a biosolids lagoon. A single open-path, infrared laser gas detector was also employed at this lagoon, giving additional methane concentration measurements to be used in the application of the inverse dispersion method using the *WindTrax* software. This field campaign was carried out to gain experience using the sensors involved with these techniques and to provide an opportunity to process collected data to estimate methane emissions from an area source. Similar measurements were made at an oil sands tailings pond, which is the main focus of this thesis and will be discussed in Chapter 5. The measurement site and the specific methodology employed during this field campaign are described. Methane and carbon dioxide fluxes determined using eddy covariance and methane fluxes estimated using the inverse dispersion method are presented, as well as a footprint analysis of the flux measurements. Site limitations are discussed and improvements upon the methodology for the subsequent field campaign at the tailings pond are outlined.

4.1 Site Description

The site of this field campaign was a biosolids lagoon at a municipal waste treatment centre. The test lagoon is one of six lagoons storing biosolids from a distant wastewater plant (Figure 4.1). The biosolid material is nutrient-rich solid organic matter that is produced after wastewater sludge stabilization and dewatering at the wastewater plant. The test lagoon had an area of 3.8 x 10^4 m^2, with dimensions 115 m x 340 m. It was selected because it offered a suitable (albeit far from ideal) place for instrument set-up on a concrete jetty extending approximately 9 m from the edge of the lagoon towards the centre, and it allowed a southeast orientation of the sonic anemometer (the predominant wind direction during the measurement period). At the eastern edge of the chosen lagoon, there was a large topographic flow disturbance, compromising any assumption of horizontal homogeneity regarding the flow. A second, larger lagoon located upwind and east of the test lagoon would have been a more desirable choice for the site location, as it was believed to be a much stronger source of methane. However, site operations during the measurement period prohibited choosing that larger lagoon.

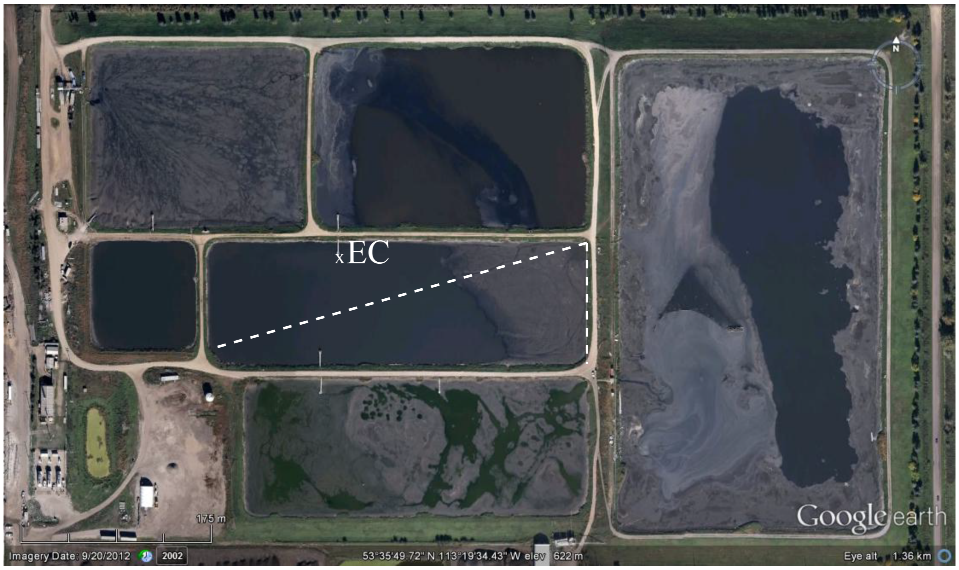

Figure 4.1: Aerial image of test lagoon (located in centre) and surrounding lagoons. Location of eddy covariance instruments and laser paths (dashed lines) across the diagonal and along the eastern edge of the lagoon are shown.

The eddy covariance instruments were mounted on the concrete jetty such that the sonic anemometer was positioned with a bearing of 109° in the compass convention (the direction of maximum fetch over the lagoon) and the instrument height above the surface of the lagoon was 1.68 m. This height above the surface was far from ideal. At such a low height, a significant component of the vertical flux is carried by eddies too small and rapid to be detected given the path lengths and separations of the individual sensors, resulting in flux losses. Limited resources and time forbade mounting the instruments higher above the lagoon surface. Furthermore the proximity of the instruments to the concrete face of the jetty disturbed the flow, and resulted in sizeable vertical velocities seen by the sonic anemometer. The distance from the centre of the sonic path to the centre of the LI-7700 light path was 45.5 cm. The distance from the centre of the sonic path to the LI-7500A light path was 23 cm (Figure 4.2).

Figure 4.2: Eddy covariance instruments mounted on concrete jetty at biosolids lagoon field site: LI-7500A (left), CSAT3 sonic anemometer (centre), and LI-7700 (right). Separation distance between sensors is noted.

An open-path, infrared laser gas detector was positioned at the northeast corner of the lagoon and reflectors were positioned at the southwest and southeast corners.

The diagonal path to the reflector placed at the southwest corner had a path length of 360.9 m, while the path length from the detector to the reflector at the southeast corner along the eastern side of the lagoon was 113.2 m (Figure 4.1). The height of the beam was 1.75 m above the surface of the lagoon.

4.2 Field Campaign Specific Methodology

Measurements were made starting on 26 April and ending 5 May 2012. During this period, data was not recorded 57% of the time due to power loss or non-ideal conditions. For measurements made on 26 April, the distance from the sonic to the concrete jetty was 110.5 cm. On 30 April, the sonic was retracted 16.5 cm closer to the jetty, bringing it closer to the gas analyzers, and it remained there for the remainder of the measurements.

Measurements made with the eddy covariance instruments were recorded onto a datalogger at a 10 Hz acquisition frequency. A program written in CRBASIC (provided by Campbell Scientific, altered slightly to give desired outputs) to direct measurement, processing, and data storage operations was loaded onto the datalogger prior to the field campaign. The datalogger computed averages, standard deviations, and covariances of the measurements and output the results to a data table every 30 minutes.

During post-processing, application of the coordinate rotation was essential because the close proximity of the instruments to the concrete face of the jetty resulted in sizeable vertical velocities, with a median value of 0.34 m s^{-1}. Performing this coordinate rotation resulted in computed fluxes that were systematically different from those given directly by the datalogger program. However, without this rotation, and as they should be, the fluxes computed in post-processing were consistent with those reported by the datalogger. To calculate gas fluxes from the covariances, a program in R was developed (see Appendix A for program code) to perform the corrections outlined in Chapter 3 and Appendix B. Methane flux values associated with spikes resulting from signal loss or instrument malfunction due to rain were removed.

The open-path, infrared laser gas detector was intermittently run during the field campaign. Usually the laser gas detector was aligned diagonally across the lagoon, but for two separate two hour periods it was aligned along the eastern edge. Methane concentration measurements made with this detector were averaged over 30-minute periods. Periods of low light level and rain were removed. Methane emission rates were estimated from these concentrations and the meteorological conditions measured at the eddy covariance system using the inverse dispersion method.

4.3 Results

4.3.1 Meteorology

Wind was generally light to moderate, with speeds never exceeding 6 m s^{-1} (Figure 4.3a). Generally, the wind was close to the ideal direction that maximized fetch over the lagoon, taken to be the bearing of the sonic anemometer, 109° (Figure 4.3b). Temperatures were typical of spring conditions, with minimum temperatures occurring in the early morning and maximum temperatures occurring just after mid-day. Temperatures ranged from 1.5°C to 14.8°C, with a median temperature of 8.3°C (Figure 4.3c). The sensible heat flux over the lagoon ranged from -17.8 W m^{-2} to 145 W m^{-2}, with a median value of 15.2 W m^{-2}. A diurnal pattern in sensible heat flux can be seen (Figure 4.3d), with maximum diurnal values obtained just after midday and minimum values just after sunset. Precipitation was frequent during the measurement period. Approximately 30% of the 30-minute averaging intervals occurred during rain. Rain results in erroneous data because water on the mirrors of the open-path gas analyzers interrupts the sensor optical path. For this reason, periods of rain were removed, producing gaps in both the flux and concentration results.

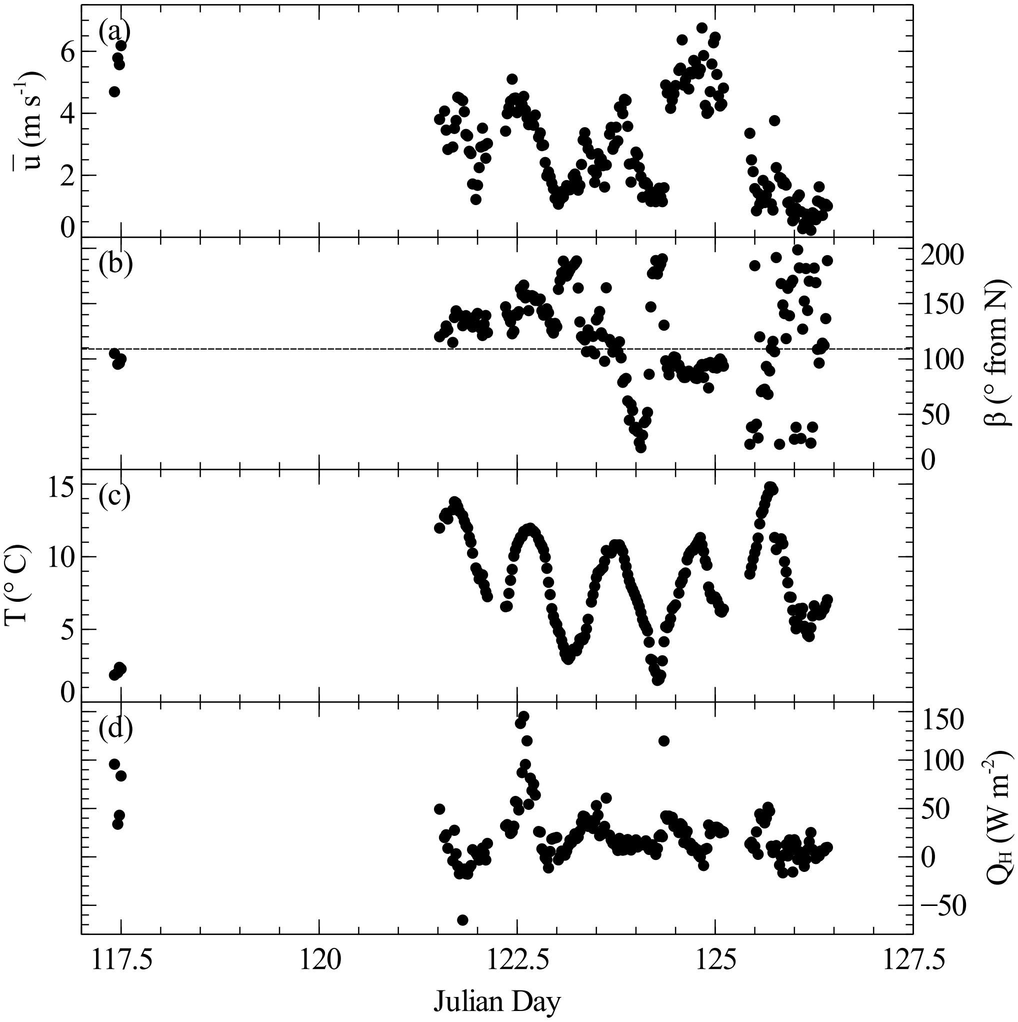

Figure 4.3: Meteorological observations from sonic anemometer measurements made during the field campaign: (a) mean horizontal velocity post-rotation, $\overline{u}$ (m s^{-1}); (b) wind direction, β (° from North), with dashed line showing bearing of sonic anemometer; (c) temperature, T (°C); (d) sensible heat flux, Q_H (W m^{-2}).

4.3.2 Methane Concentration

After the data had been filtered to remove heavy rain events, the methane concentration measured by the LI-7700 ranged from 2.67 ppm to 10.9 ppm, with a median value of 3.65 ppm. Methane concentrations were found to be higher at night than during the day (Figure 4.4), which is consistent with earlier experiments (Mahzabin, 2012) and probably reflects reduced nocturnal mixing. The methane concentration measurements made with the laser gas detector aligned across the diagonal of the test lagoon agreed well[2] with the LI-7700 concentration measurements when compared during the same 30-minute time periods (Figure 4.5). The methane concentration measured using the laser gas detector in this position ranged from 2.69 ppm to 4.67 ppm, with a median value of 3.64 ppm. When this detector was aligned along the eastern edge of the test lagoon, the methane concentration was much higher than that measured along the diagonal across the lagoon (see Figure 4.1), with concentrations ranging from 5.21 ppm to 9.55 ppm and a median value of 6.42 ppm. Given that the predominant wind direction over the measurement period was from the southeast, the higher concentrations measured by the laser gas detector when aligned along the eastern edge can plausibly be assumed to reflect the presence of the large lagoon upwind of the detector acting as a stronger source of methane.

4.3.3 Methane Flux using the Eddy Covariance Technique

The methane fluxes[3] using eddy covariance ranged from 1.40 x 10^{-3} kg $m^{-2}day^{-1}$ to 1.43 x 10^{-2} kg $m^{-2}day^{-1}$, with a median value of 7.77 x 10^{-3} kg $m^{-2}day^{-1}$, after the data had been filtered to remove rain events. These results were also filtered for the deviation of the mean wind from the direction of maximum fetch over the lagoon (109°). Data were selected such that they met the criterion wherein the mean wind direction during that 30-minute period was within ±30° of the direction

---

[2] The signals are not expected to be identical, of course, for the instruments sampled distinct volumes.

[3] The sign convention of the fluxes reported in this thesis is positive away from the surface and negative towards the surface.

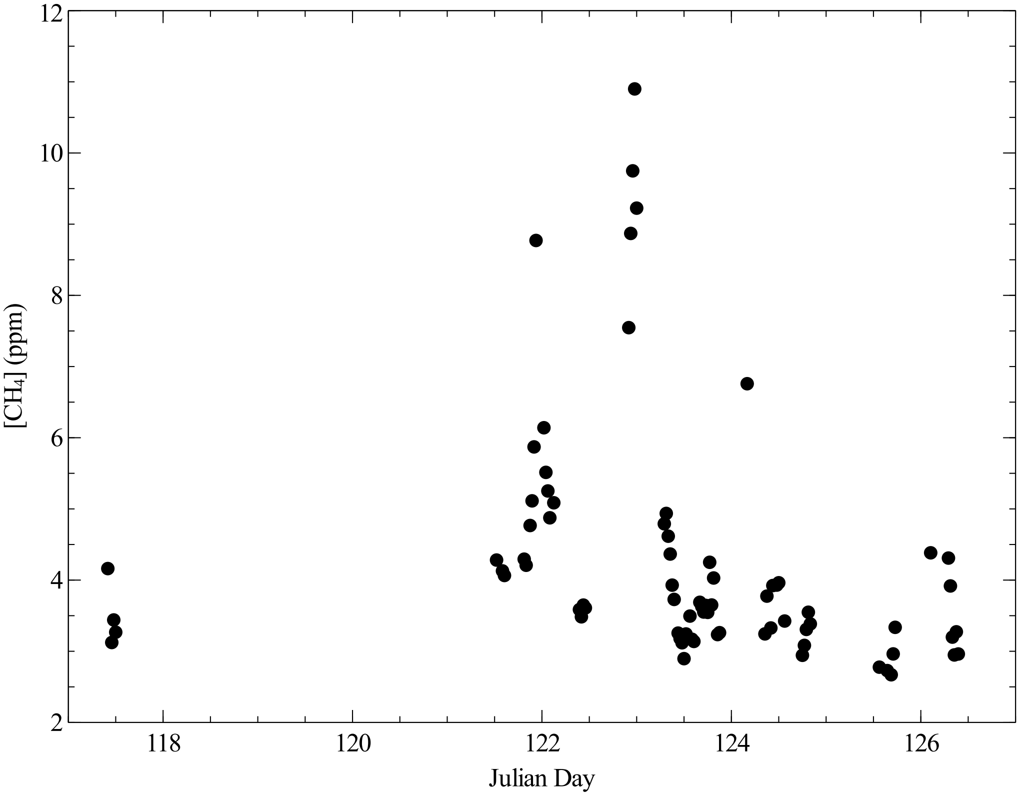

Figure 4.4: Time series of methane concentration (ppm) measurements made with the LI-7700 at the biosolids lagoon.

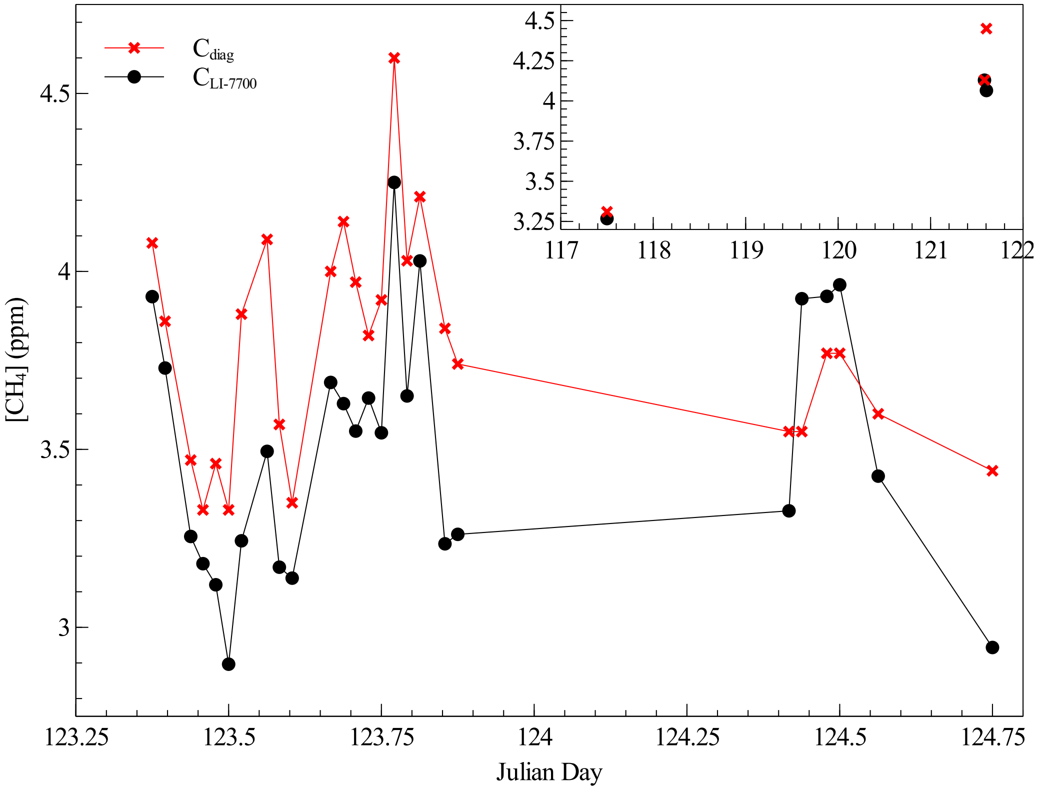

Figure 4.5: Time series of methane concentration (ppm) measurements made with the LI-7700 and laser gas detector aligned along the diagonal of the biosolids lagoon. Only the time periods when there were measurements from both the LI-7700 and the diagonal detector were selected.

of maximum fetch. When this wind direction filter is applied, the influence of other potential sources of methane nearby is minimized. Given that the test lagoon was surrounded by other lagoons that were potentially emitting methane, applying this wind direction filter to the measurements is necessary. Methane fluxes corresponding to these time periods of ideal wind direction spanned a much narrower range of values than when this filter was not applied. The methane emission rate (calculated using the estimated area of the lagoon) ranged from 2.22 kg hr^{-1} to 22.6 kg hr^{-1}, with a median value of 12.3 kg hr^{-1} (Figure 4.6).

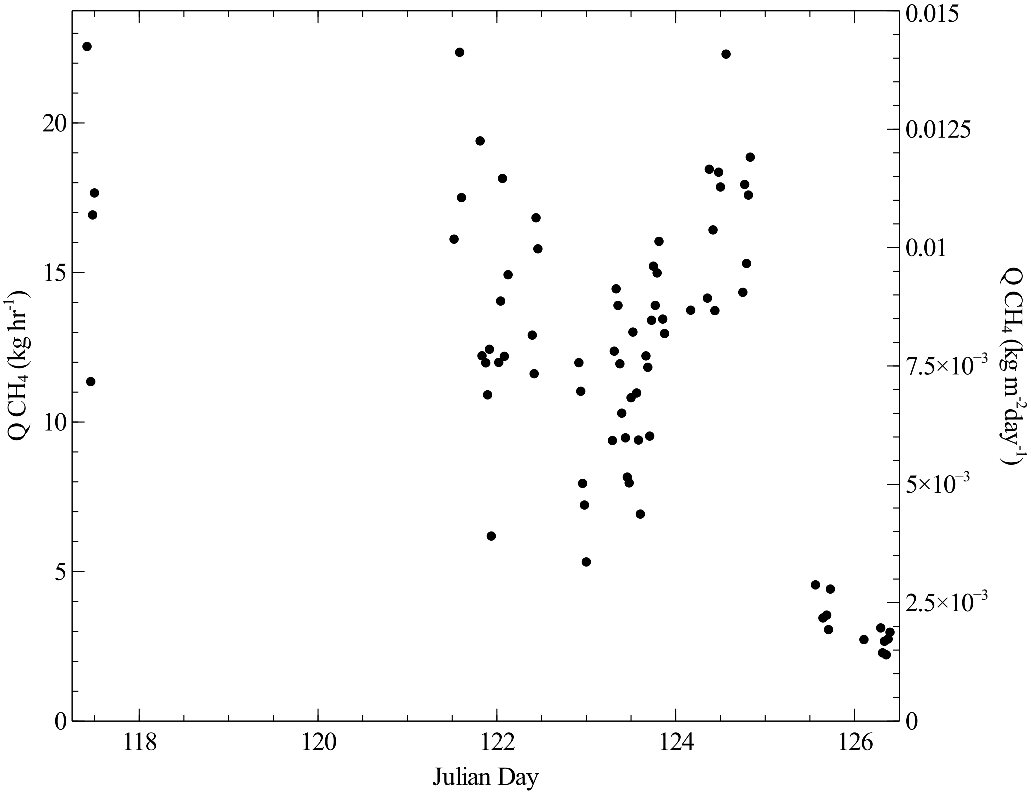

Figure 4.6: Time series of methane emission rate (kg hr^{-1}) and flux (kg m^{-2}day^{-1}) measurements made using the eddy covariance technique. Data has been filtered to remove rain events and only include periods when the mean wind direction during the 30-minute sampling period was in an ideal direction (109° ± 30°).

4.3.4 Methane Flux using the Inverse Dispersion Technique

The line-average methane concentration measurements made by the open-path, infrared laser gas detector and the meteorological measurements made by the sonic anemometer were used as inputs to *WindTrax* to estimate the emission rate of methane using the inverse dispersion method (specifics of how *WindTrax* is used as an application of the inverse dispersion method are given in Chapter 3.1.2). The *WindTrax* simulation incorporated methane concentration measurements made on the diagonal and eastern edge of the lagoon that were as close in time as possible (simultaneous concentration measurements were not possible, as only one laser gas detector was used at the site). Meteorological conditions corresponding to the time period when the laser gas detector was aligned along the diagonal were used. Since the detector was only positioned along the eastern edge of the test lagoon twice during the measurement period, the *WindTrax* simulation could only be performed for two data periods: measurements made at 12:00 MDT on 26 April and 15:00 on 30 April for the diagonal methane concentration and sonic anemometer data, and at 11:30 on 26 April and 15:30 on 30 April for the methane concentration measured along the eastern edge of the test lagoon. The wind direction during these measurement periods and the alignments of the laser paths allow *WindTrax* to estimate the emission rates from both the test lagoon and the larger lagoon to the east. The methane concentration measurements, roughness length, friction velocity, wind direction, Obuhkov length, temperature, and pressure for the averaging interval (30 minutes) were used as inputs to *WindTrax* (Table 4.1). In all cases, the background concentration was assumed to be 1.9 ppm (Mahzabin, 2012).

Table 4.1: Meteorological conditions used as input parameters for the *WindTrax* simulations, including temperature (T), pressure (P), wind direction (β), roughness length (z_0), friction velocity (u_*), and Obukhov length (L).

Time Period	T (°C)	P (kPa)	β (°from N)	z_0 (cm)	u_* (m s^{-1})	L (m)
26 April	2.27	93.6	100	0.26	0.39	-93.8
30 April	12.6	92.6	126	2.37	0.27	-350

The *WindTrax* backward trajectory simulation (referred to as Simulation A) was performed with $N_p = 50,000$ particles released from each sensor location at a height of 1.75 m above the test lagoon. In order to represent a line average concentration, 50 source points along the laser path were used. Figure 4.7 gives a schematic representation of Simulation A and Figure 4.8 is a screenshot of *WindTrax* while running this simulation. Table 4.2 gives the results from Simulation A. Despite both time periods having the diagonal methane concentration lower than that measured along the eastern edge of the test lagoon, the estimated emission rates were of opposite sign for the two intervals.

These lagoons have been the subject of previous studies focused on estimating methane fluxes using the inverse dispersion technique (Mahzabin, 2012). Methane flux estimates made by Mahzabin (2012) for the large lagoon were of the same order of magnitude as the values reported in Table 4.2, with average methane flux values ranging from 1.4 x 10^{-2} kg $m^{-2}day^{-1}$ to 1.9 x 10^{-2} kg $m^{-2}day^{-1}$.

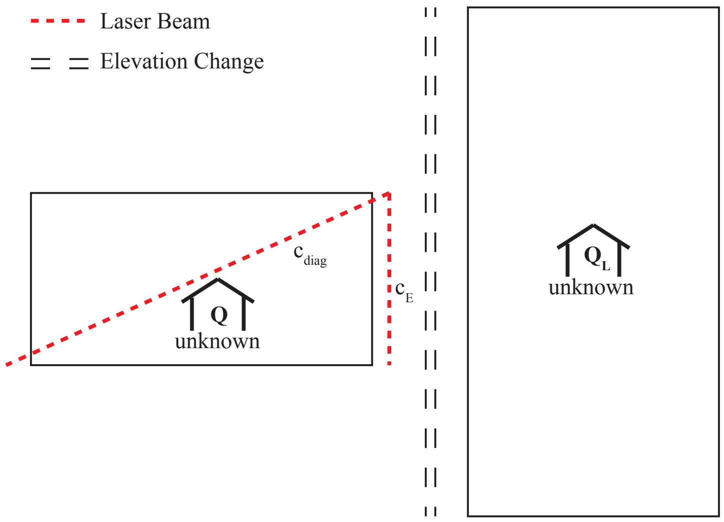

Figure 4.7: Schematic representation of *WindTrax* Simulation A used to estimate the methane fluxes from the test lagoon (Q) and large lagoon to the east (Q_L) using the methane concentration measurements made along the eastern edge of the test lagoon (c_E) and along the diagonal of the test lagoon (c_{diag}). Background concentration (c_b) is assumed to be 1.9 ppm.

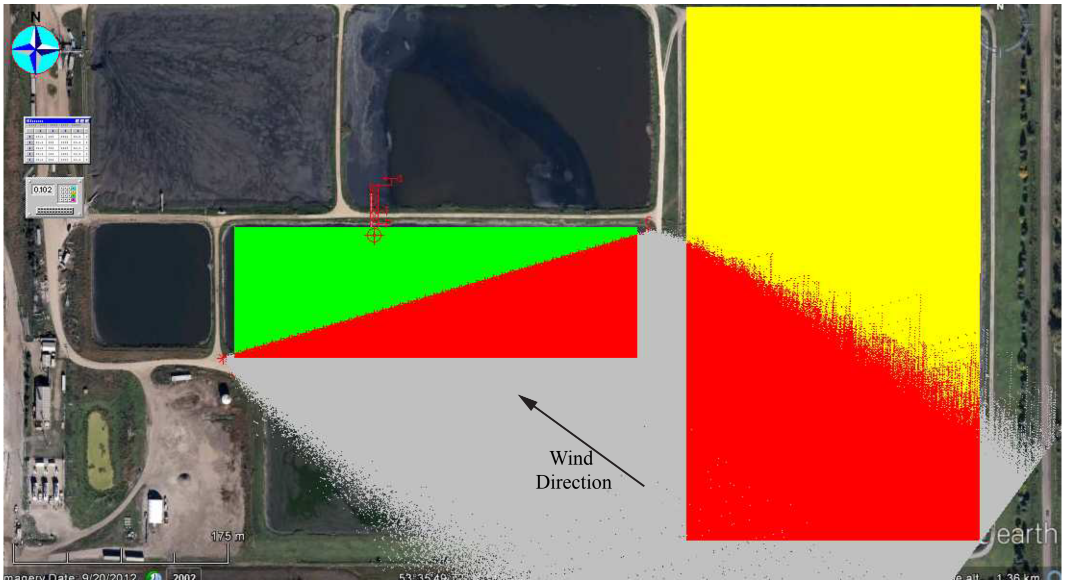

Figure 4.8: Screenshot of *WindTrax* Simulation A at the biosolids lagoon. A single plume of touchdown points is visible, emanating from the laser gas detector aligned along the diagonal of the test lagoon (plotted in red when touching down within the boundary of a source area or in grey outside the boundaries).

Table 4.2: Results of *WindTrax* Simulation A for 26 April and 30 April data periods. Methane flux estimates for the test lagoon (Q) and the large lagoon to the east (Q_L) are given, as well as the corresponding methane concentrations for those time periods.

Time Period	Methane Flux (kg $m^{-2}day^{-1}$)		[CH_4] (ppm)	
	Q	Q_L	c_{diag}	c_E
26 April	-3.97 x 10^{-3}	3.46 x 10^{-2}	3.31	5.21
30 April	9.50 x 10^{-3}	4.15 x 10^{-2}	4.67	7.95

In an effort to explore the validity of the methane flux estimates resulting from Simulation A, further simulations were performed, varying the mix of measured inputs (c_{diag}, c_E) and unknowns (Q, Q_L). Simulation B (single unknown, single measured input) required *WindTrax* to first infer the source strength of the large lagoon (Q_L) from the concentration reported by the laser gas detector at the east end of the test lagoon (c_E), with background concentration, $c_b = 1.9$ ppm, imposed (Figure 4.9a). The laser gas detector at the east end of the lagoon was at the base of a berm, but there was no option other than to ignore this flow disturbance. As expected, the resultant flux estimates for Q_L were the same as when both the flux from the test lagoon and large lagoon were treated as unknowns (Simulation A). In the second phase of Simulation B, the unknown flux from the test lagoon was calculated given the (now) known Q_L, the diagonal concentration c_{diag}, and the background concentration c_b (Figure 4.9b). The flux estimates for the test lagoon resulting from Simulation B for the first and second time periods are given in Table 4.3, and are almost perfectly consistent with Simulation A performed with two unknown source strengths.

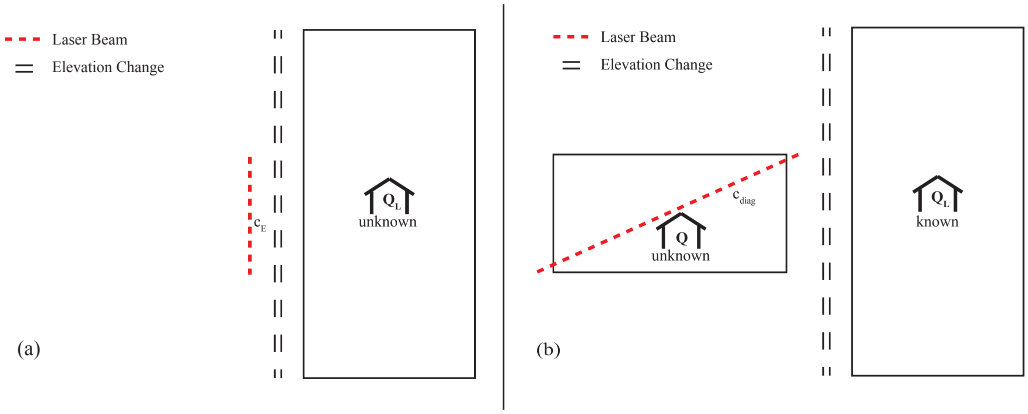

Figure 4.9: Schematic representation of *WindTrax* Simulation B: (a) Methane flux from the large lagoon (Q_L) is estimated from the assumed background concentration (c_b) and concentration measured along eastern edge of test lagoon (c_E), (b) Methane flux from the test lagoon (Q) is estimated from concentration measured along diagonal of test lagoon (c_{diag}), assumed background concentration, and estimated flux from the large lagoon.

Table 4.3: Estimated methane fluxes for the test lagoon (Q) and large lagoon to the east (Q_L) resulting from Simulation B. Q_L is estimated from the concentrations measured along the eastern edge of the test lagoon and the background concentration. Q is then estimated from this (now known) Q_L and the diagonal concentration.

Time Period	Methane Flux (kg $m^{-2}day^{-1}$)		[CH_4] (ppm)		
	Q	Q_L	c_b	c_{diag}	c_E
26 April	-4.49 x 10^{-3}	3.46 x 10^{-2}	1.9	3.31	5.21
30 April	1.04 x 10^{-2}	4.15 x 10^{-2}	1.9	4.67	7.95

Simulation C was performed to test the suspicion that for the period that estimated a negative flux off the test lagoon, *WindTrax* was expecting a larger concentration at the diagonal gas detector than had actually been measured. To do this, Q_L was inferred just as it had been in Simulation B (Figure 4.10a), and this value for Q_L was then used to compute the expected concentration along the diagonal path, c_{diag*} (setting $Q = 0$, such that the influence of the test lagoon was ignored) (Figure 4.10b). The results of Simulation C are given in Table 4.4. For the first time interval, the expected concentration along the diagonal is greater than the measured concentration, suggesting that the test lagoon would give a negative flux (i.e., the lagoon acts as a methane sink). For the second time interval, the expected concentration is less than the measured concentration along the diagonal, suggesting that *WindTrax* would estimate a positive flux for the test lagoon (i.e., the lagoon acts as a source).

The results from Simulations B and C were consistent with those of the original *WindTrax* simulation (Simulation A) in that the emission estimates for the two intervals were of opposite sign, despite both intervals having a lower methane concentration measured along the diagonal of the test lagoon than along the eastern edge. This is due to the realities of the site deviating from the ideal assumed by the model. The simulations had to neglect the fact that the wind was disturbed by the large change in elevation at the east end of the test lagoon.

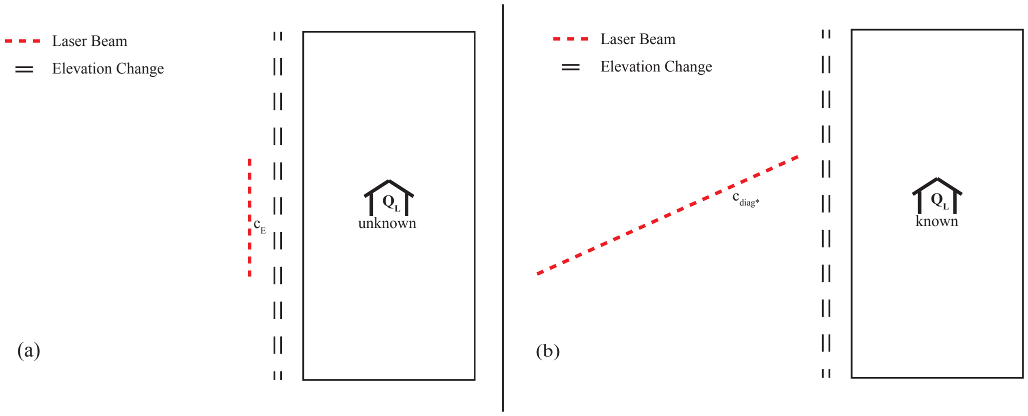

Figure 4.10: Schematic representation of *WindTrax* Simulation C: (a) Methane flux from large lagoon (Q_L) is estimated from the assumed background concentration (c_b) and concentration measured along eastern edge of test lagoon (c_E), (b) Expected concentration along the diagonal of the test lagoon (c_{diag*}) is computed from the estimated emission rate of the large lagoon and the assumed background concentration, ignoring the influence of the test lagoon.

Table 4.4: Estimated CH_4 concentrations along the diagonal of the test lagoon for Simulation C. Q_L is estimated from the concentration measured along the eastern edge of the test lagoon and the background concentration. The expected concentration along the diagonal (c_{diag*}) is then computed from this Q_L, ignoring the influence of the test lagoon.

Time Period	Q_L (kg $m^{-2}day^{-1}$)	$[CH_4]$ (ppm)		
		c_b	c_{diag*}	c_{diag}
26 April	3.46 x 10^{-2}	1.9	3.58	3.31
30 April	4.15 x 10^{-2}	1.9	3.73	4.67

4.3.5 Carbon Dioxide Concentration and Flux

The CO_2 concentrations measured by the LI-7500A were filtered for heavy rain events and a quality control parameter was implemented to only include data when $[CO_2] \geq 300$ ppm (Figure 4.11). The filtered CO_2 concentration ranged from 308 ppm to 438 ppm, with a median value of 393 ppm. The CO_2 flux ranged from -3.56 x 10^{-1} kg $m^{-2}day^{-1}$ to 3.46 x 10^{-1} kg $m^{-2}day^{-1}$, with a median value of 2.40 x 10^{-2} kg $m^{-2}day^{-1}$. The CO_2 flux was filtered to remove rain events and only include data periods where the wind direction was ± 30° of the direction of maximum fetch. The CO_2 emission rate (calculated using the estimated area of the lagoon) ranged from -5.64 x 10^2 kg hr^{-1} to 5.49 x 10^2 kg hr^{-1}, with a median value of 3.80 x 10^1 kg hr^{-1} (Figure 4.12).

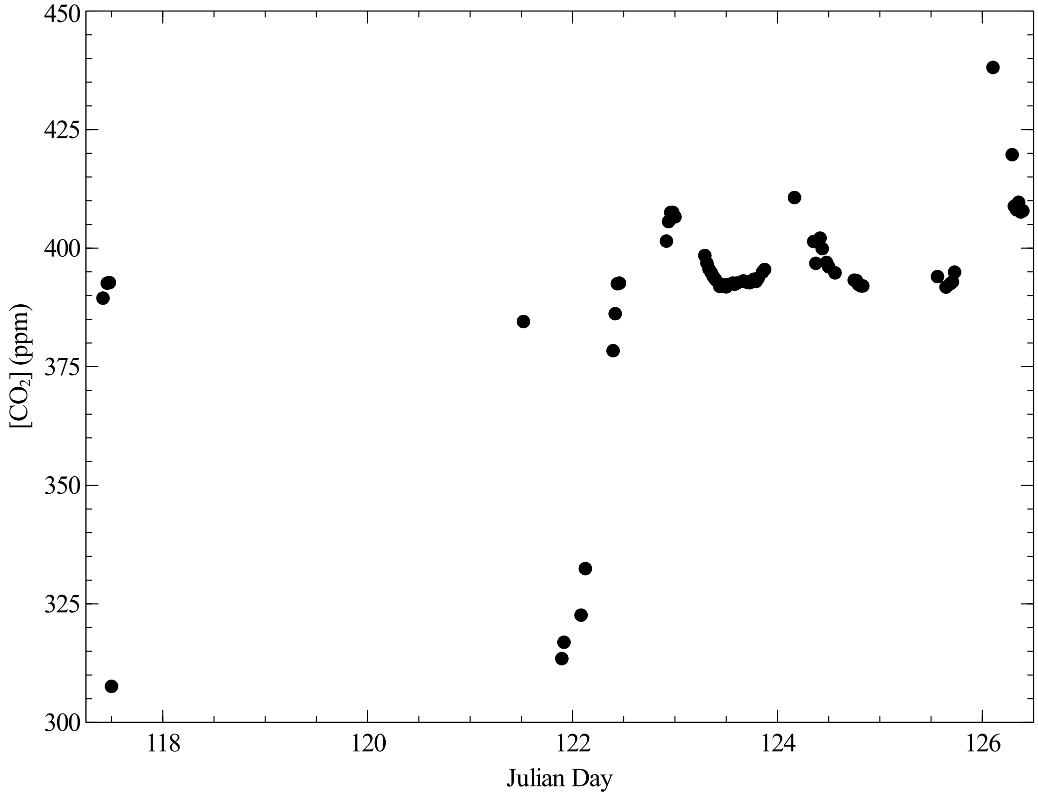

Figure 4.11: Time series of CO_2 concentration (ppm) measurements made with the LI-7500A at the biosolids lagoon, filtered to remove rain events.

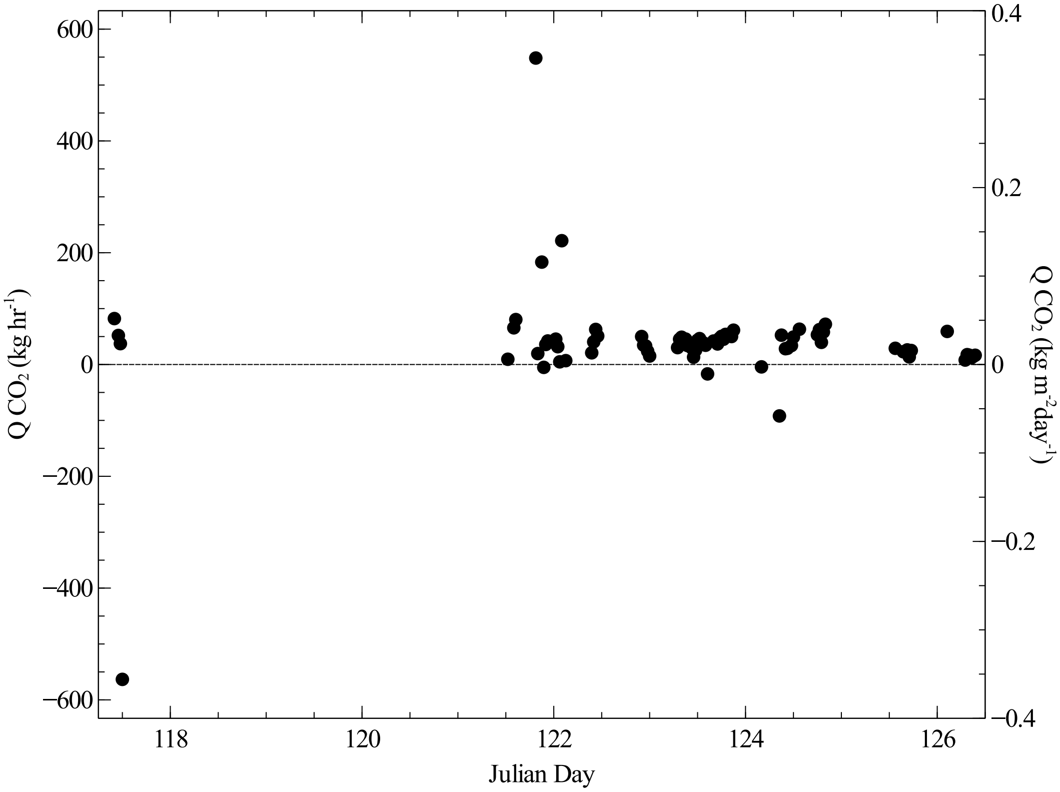

Figure 4.12: Time series of CO$_2$ emission rate (kg hr^{-1}) and flux (kg m^{-2}day^{-1}) measurements made using the eddy covariance technique at the biosolids lagoon, filtered to remove rain events and only include data where the mean wind direction during the 30-minute sampling period was in an ideal direction (109° ± 30°).

4.3.6 Flux Footprint

The parameterized statistical model of the scalar flux-source area model (mini-FSAM) given by Schmid (1994) was used to estimate the 50% source area of the flux measurements for the measurement period. The resultant source area estimate for the 22:00-22:30 MDT on 1 May time period had dimensions consistent with the median dimensions of the source areas for all time periods (Figure 4.13). The area bounded by this 50% contour was calculated to be approximately 2.6 x 10^2 m^2. This time period had unstable stratification and roughness length and turbulence conditions close to the average over the entire measurement period. Most of the estimated 50% source areas did not extend further than 59 m from the sensors. This model also gave the approximate upwind distance to the location of maximum flux influence. The median value for this distance was found to be approximately 15 m (measured upwind from the sensors).

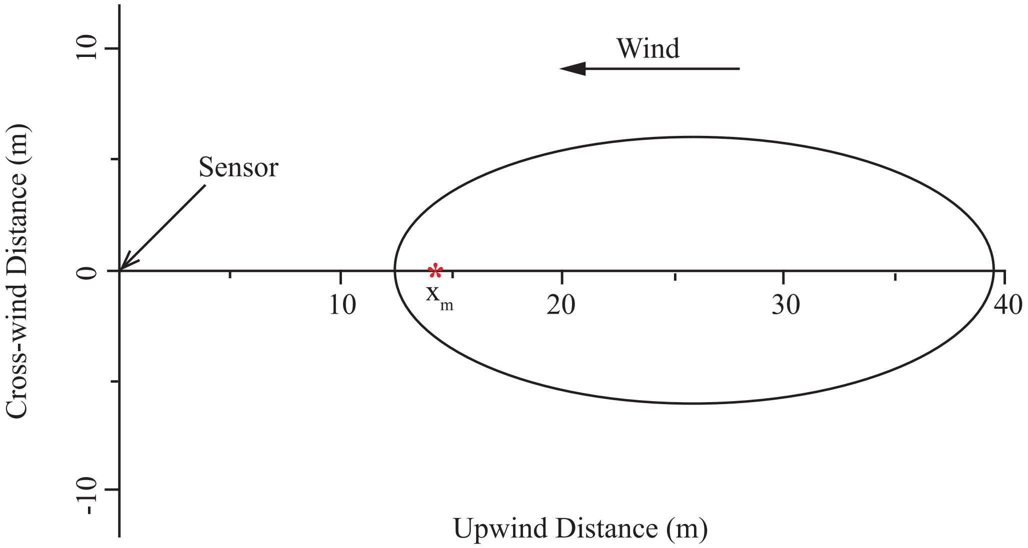

Figure 4.13: Schematic representation of the 50% source area for 22:00-22:30 on 1 May. Location of upwind distance with the maximum influence on the sensor marked by x_m.

Hsieh et al. (2000) developed an approximate analytical model to estimate the 90% flux fetch. Similar to the mini-FSAM presented by Schmid (1994), this model relates the fetch to atmospheric stability, measurement height, and the surface roughness length. The median value for the 90% flux fetch was estimated to be a distance of 253 m from the sensors.

Determining the upwind area contributing to the measured fluxes is useful in cases that (as here) the fluxes are estimated from sources that are non-uniform (Horst and Weil, 1992). A second, larger lagoon located upwind and east of the test lagoon is believed to be a much stronger source. A very short period of measurements with the laser gas detector oriented along the eastern side of the lagoon gave methane concentrations that were higher than those measured on the diagonal of the test lagoon. Given the source areas estimated by the footprint calculations, this upwind lagoon could have a large influence on the flux measurements, depending on the wind direction during a given time period.

4.4 Discussion

This site was not ideal for making eddy covariance measurements, both in terms of the fetch of test lagoon upwind of the sensors and the existence of flow disturbances. The presence of the large lagoon located upwind of the test lagoon was one of the major issues that had to be considered. This lagoon was a stronger source than the test lagoon, as evidenced by the higher concentration sensed by the laser gas detector along the eastern edge of the test lagoon. Considering the flux footprint analysis, the fluxes determined using eddy covariance could have been influenced by the presence of this lagoon. Most of the data periods had 50% source areas within the extent of the test lagoon, however only in 28% of the data periods was the along wind fetch sufficient to eliminate contamination of the measured flux by emission from surfaces other than the test lagoon, as determined by the 90% flux fetch calculated using the Hsieh et al. (2000) method. This is not surprising given the site conditions and small measurement height. The results presented here were filtered so as to avoid periods of short fetch over the test lagoon by limiting the acceptable wind direction to ± 30° of the direction of maximum fetch, but this did not completely remove the influence of other potential sources of methane.

Flow disturbance was caused by both the large berm at the eastern edge of the test lagoon and the proximity of the eddy covariance instruments to the concrete jetty they were mounted on. The flow disturbance caused by the jetty introduced mean vertical motion that would contribute to the vertical flux of the subject gas, making it necessary to perform the coordinate rotation. The large change in elevation at the east end of the test lagoon was neglected in the *WindTrax* simulations. The presence of this topographic flow disturbance compromises any assumptions made regarding the flow and as such makes the emission estimates provided by *WindTrax* suspect.

These adverse site conditions were deemed acceptable as this was merely a preliminary field campaign used as a learning experience in preparation for the campaign at the oil sands tailings pond later in the summer. This field campaign did allow for familiarization with running the instruments in the field, where factors such as rain had to be taken into account. It also provided experience implementing the coordinate rotation and flux corrections in post-processing of the data, as well as the discovery of certain limitations in the methodology that needed to be improved upon for the next field campaign. For instance, the use of single batteries that needed to be recharged regularly resulted in periods of data loss. To remedy this, a solar panel system was used at the tailings pond field site to allow continuous data collection. Only a single laser gas detector was used to measure methane concentration during this field campaign and as such, a meaningful upwind/downwind difference in methane concentration was not established. The two concentration measurements used in the *WindTrax* simulations for the eastern edge and along the diagonal of the test lagoon were not simultaneous, as they should have been. For the second field campaign, two separate laser gas detectors were deployed simultaneously to avoid this issue. The signal strength of the LI-7700 methane analyzer was not recorded in the datalogger output table, so it could not be used as a quality check for the methane concentration measurements. Instead, field notes regarding the weather conditions (e.g., rain events) were used as a means of filtering bad data.

The datalogger code was amended for the second field campaign to add this signal strength measurement to the output table, allowing for instrument performance to be more accurately monitored.

Chapter 5

Oil Sands Tailings Pond Field Campaign

Eddy covariance measurements of CH_4 and CO_2 fluxes were made at an oil sands tailings pond. Although a subsidiary element of the field campaign, two open-path, infrared laser gas detectors were also employed at this site to give additional methane concentration measurements, to be used in the application of the inverse dispersion method using the *WindTrax* software. This chapter gives a description of the measurement site and the specific methodology employed during the field campaign. Results of the methane and carbon dioxide fluxes from eddy covariance and methane flux estimated using the inverse dispersion technique are presented. The results from the post-processing of the eddy covariance measurements using the R program are compared with the results of the analysis using the EddyPro software.

5.1 Site Description

Oil sands tailings ponds store coarse tailings, thickened tailings, and froth treatment tailings. As a result, the tailings pond is made up of coarse sand, silt, processed water, and residual bitumen and solvent (used for the extraction and transportation of bitumen). The tailings pond where the measurements were made was generally brown in colour, with oily films covering the surface and patches of accumulated bitumen spread throughout, particularly at the edges of the pond. During the sampling campaign, it was observed that the bitumen residing on the surface of the pond was continuously displaced due to the wind. The area of this tailings pond was approximately 4.2 x 10^6 m^2, and was roughly elliptical in outline with major and minor axes of about 1.5 km and 3.0 km, respectively.

Restrictions on site selection for both the eddy covariance tower and the open-path, infrared laser gas detectors were severe. The dominant wind direction during the field campaign was such that the site chosen for the eddy covariance instruments was suitable. The eddy covariance instruments were mounted on a tower that was situated on a low berm (about 0.5 m high) at the northern edge of the pond (Figure 5.1). This berm was low enough so as not to result in flow disturbance for the sonic anemometer located at the top of the tower. The eddy covariance instruments were mounted at a height of 8.5 m above the tailings pond surface. The tower was approximately 7 m from the pond edge. The wind direction anticipated for the field campaign was southeast. Accordingly, the sonic anemometer was oriented with a bearing of 169°. The path separation between the sonic anemometer and the LI-7700 was 36 cm. The path separation between the sonic anemometer and the LI-7500A was 22 cm.

Two open-path, infrared laser gas detectors (Boreal Laser's GasFinder2) were positioned as close to the edge of the tailings pond as was permitted. Due to the restrictions on the feasible (and permissible) locations for the laser gas detectors, the detectors were not in positions that could take advantage of wind directions during many time periods. One laser gas detector was located at the southern edge of the pond, with a path length of 152 m. The second laser gas detector was located at the northwest corner of the pond, with a path length of 167 m. The height of the detectors above pond surface was approximately 10-15 m. These placements were not ideal to sample CH_4 concentration both upwind and downwind of the pond. Out of necessity, the laser gas detectors were placed approximately 200 m from the edge of the tailings pond. In this intervening distance, there was a gently sloping beach of sand rising about 5 m, followed by a more abrupt, irregular rise of roughly 2-5 m.

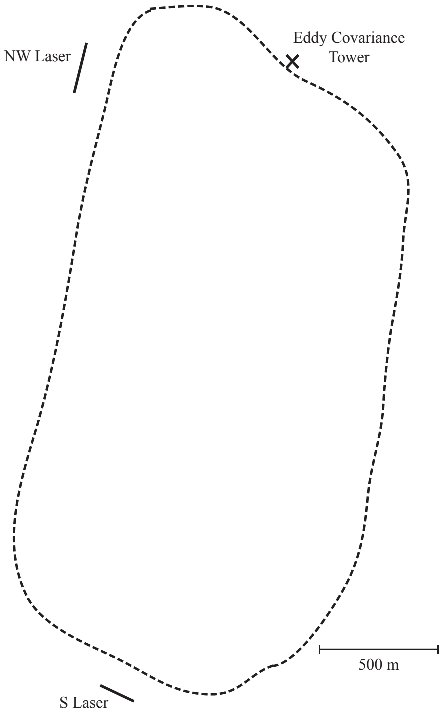

Figure 5.1: Simplified schematic representation of the oil sands tailings pond. The positions of the open-path, infrared laser gas detectors at the northwest corner and southern edge of the tailings pond are shown, as well as the location of the eddy covariance instruments.

5.2 Field Campaign Specific Methodology

Eddy covariance measurements were conducted from 11 July to 16 July 2012. Due to restrictions placed on site access, the instruments could only be monitored for the first two days of the measurement period and of necessity they were left unattended for the remainder of the period. The datalogger output included both the data table containing the 30-minute averages, standard deviations, and covariances of the measurements, as well as the raw time series data table at a 10 Hz acquisition frequency. In contrast to the field campaign at the biosolids lagoon, power to the eddy covariance instruments was provided by a solar panel system connected to

12 V batteries, allowing for continuous data collection. Post-processing of the eddy covariance data was carried out in the same manner as in the preliminary field campaign at the biosolids lagoon earlier in the summer. Details of this process are given in Chapter 3 and Appendix B. Application of the coordinate rotation to set $\overline{w} = 0$ required only a small rotation angle, with median value 0.24°. Both of the open-path, infrared laser gas detectors made methane concentration measurements continuously during the entire field campaign. Measurements made with these laser gas detectors were averaged over 30-minute periods and periods of low light level were removed.

5.3 Results

5.3.1 Meteorology

At 8.5 m above the surface of the tailings pond, the wind speed ranged from 0.3 m s^{-1} to 10 m s^{-1}. On the second day of meteorological measurements (12 July), there was a severe increase in wind speed shortly after the site was left unattended. Prior to this increase, the wind speed had not exceeded 5 m s^{-1}. The increase lasted four hours, before returning to normal wind speeds (Figure 5.2a). The dominant wind direction during the measurement period was from the southeast (Figure 5.2b). The sonic anemometer was mounted such that it would sample unobstructed winds for wind directions over a wide range (about ± 135°) centred about this direction. The temperature measured at the eddy covariance tower ranged from 12°C to 30°C, with median temperature of 21°C (Figure 5.3a). The sensible heat flux followed a typical diurnal pattern, with maximum values obtained just after midday and minimum values in the evening (Figure 5.3b). A plot of sensible heat flux plus latent heat flux ($Q_H + Q_E$), approximately equalling the net radiation, shows a similar diurnal pattern (Figure 5.3d). Figure 5.4 shows the latitudinal and longitudinal turbulence intensities (σ_v/u and σ_u/u, respectively), as well as the standard deviation in wind direction (σ_β) (approximated as $\sigma_\beta = \arctan(\sigma_v/u)$). MOST suggests that the ratio of the standard deviation of a signal to an appropriate scaling parameter (i.e., the turbulent intensity σ_w/u_*) should vary as a function of stability. The variation of the vertical velocity standard deviation with changes in stability agrees well with the formula of Wilson (2008) derived from measurements at an ideal site (Figure 5.5).

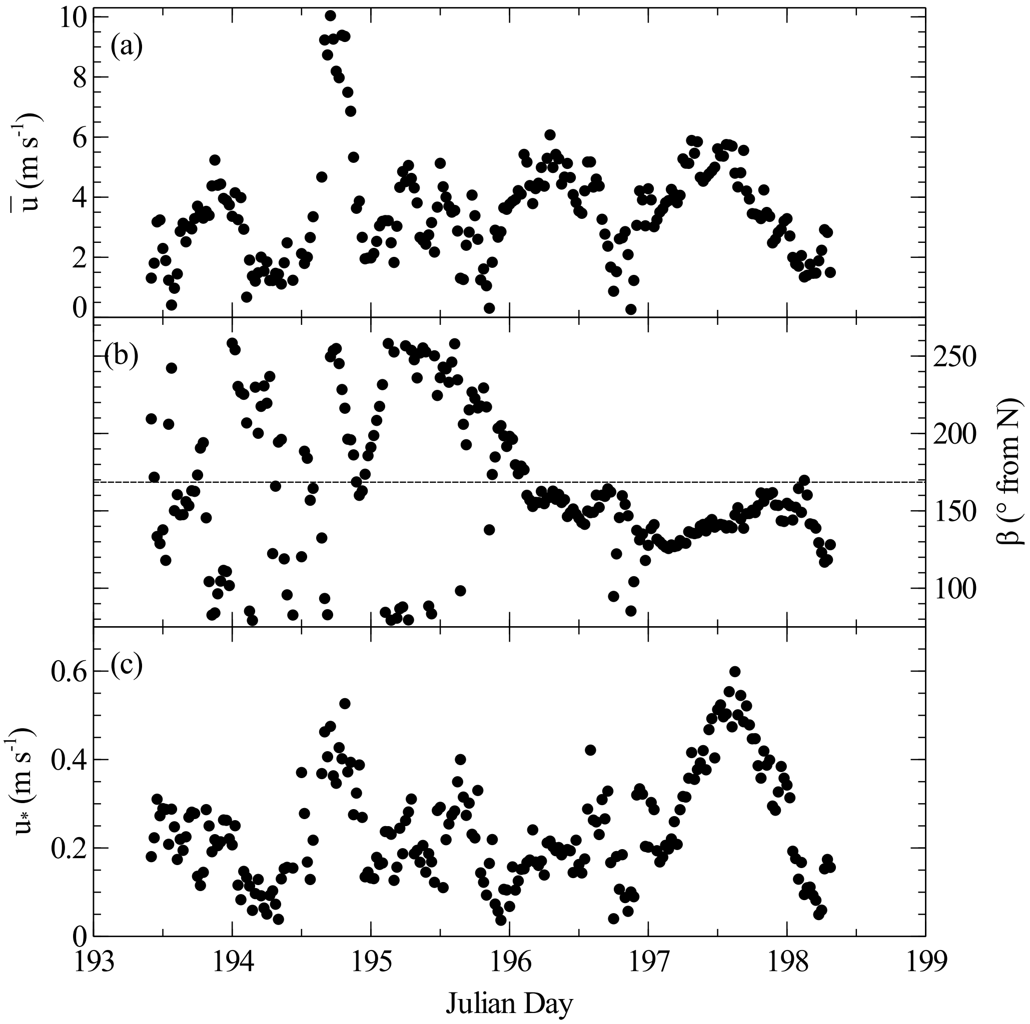

Figure 5.2: Time series of meteorological observations from sonic anemometer measurements made during the field campaign at the oil sands tailings pond: (a) mean horizontal velocity post-rotation, $\overline{u}$ (m s^{-1}); (b) wind direction, β (° from North), with dashed line showing bearing of sonic anemometer; (c) friction velocity, u_* (m s^{-1}).

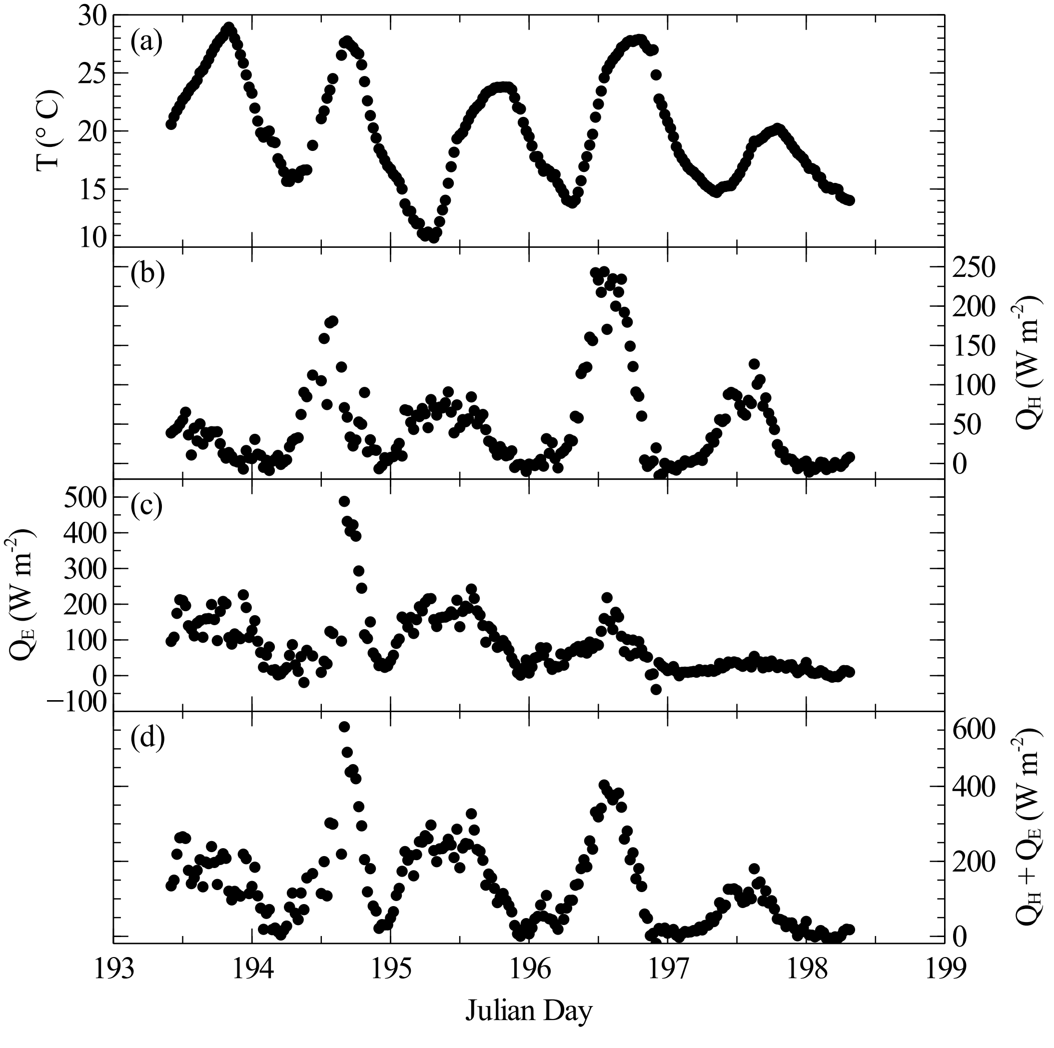

Figure 5.3: Time series of meteorological observations made during the field campaign at the oil sands tailings pond: (a) temperature, T (°C); (b)sensible heat flux, Q_H (W m^{-2}); (c) latent heat flux, Q_E (W m^{-2}); (d) $Q_H + Q_E$ (W m^{-2}).

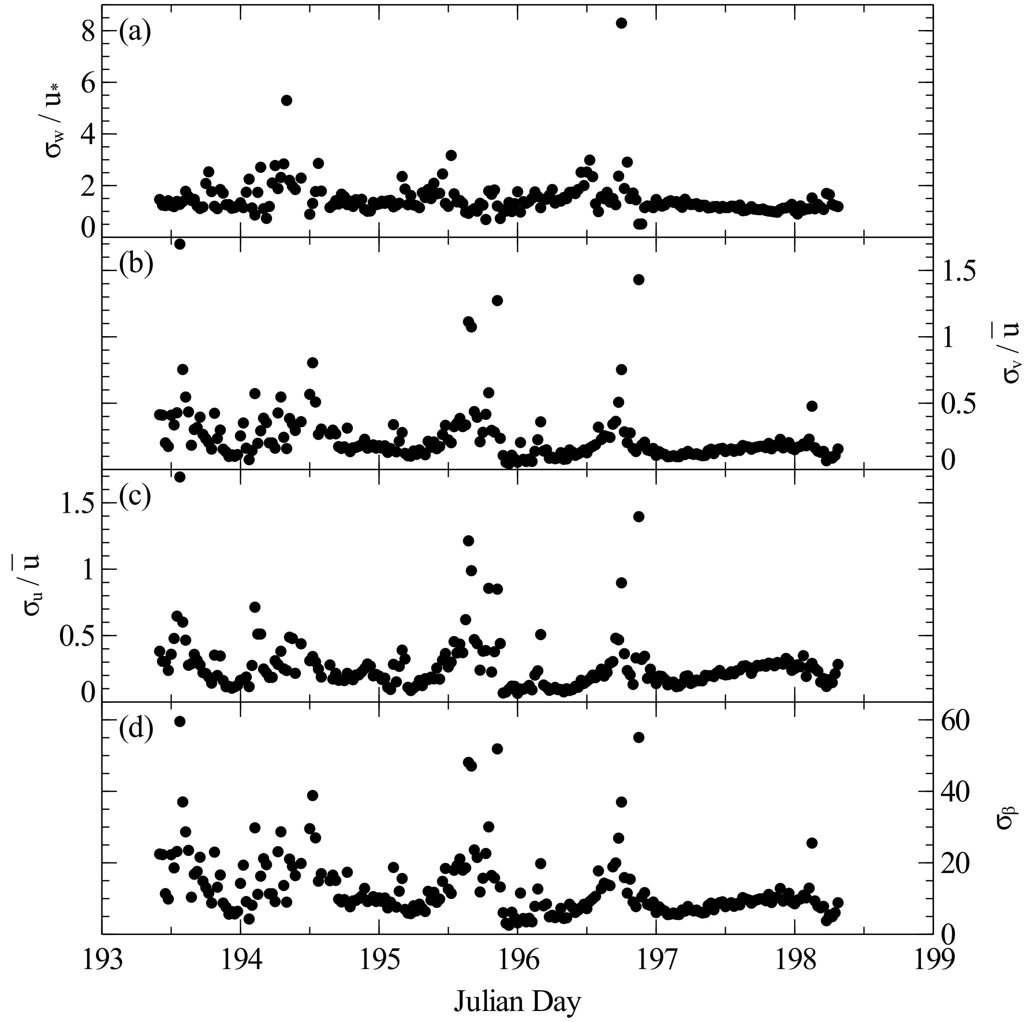

Figure 5.4: Time series of meteorological observations made during the field campaign at the oil sands tailings pond: (a) vertical turbulence intensity; (b) lateral turbulence intensity; (c) longitudinal turbulence intensity; (d) standard deviation in wind direction (in degrees).

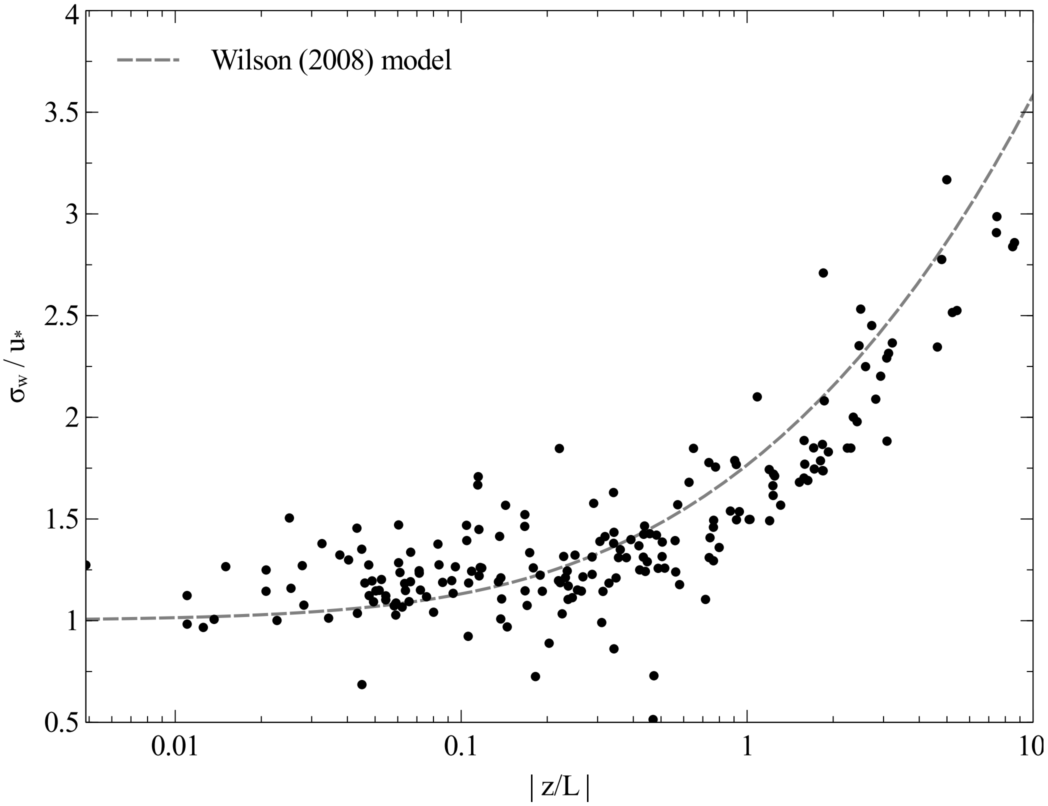

Figure 5.5: Plot of the variation in normalized standard deviation of vertical velocity with changes in stability (for unstable conditions). The dashed line gives the formula of Wilson (2008) ($\frac{\sigma_w}{u_*} = 1.0(1 - 4.5\frac{z}{L})^{1/3}$).

5.3.2 Methane Concentration

Eddy covariance measurements were made over the course of five days during which data was recorded continuously, except for when data was being downloaded from the datalogger or when the LI-7700 mirrors were being cleaned manually. As noted above, after the first two days of eddy covariance measurements, the instruments had to be left unattended at the site. Within a couple hours of leaving the site, the wind speed increased causing a dust storm that resulted in a decrease in the signal strength such that the RSSI (values ranging from 0% to 100%) dropped below 10%, indicating a signal of low quality. Methane measurements made with the LI-7700 are consistent over a wide range of RSSI values, but at low RSSI the signal-to-noise ratio of the measurement decreases (LI-COR, Inc., 2010). This decrease in signal strength is presumed to have been due to environmental factors, such as the deposition of dust and other particles in the optical path of the sensor. The dust deposited on the mirrors could not be removed manually while the instruments were left unattended. A washing cycle was set up to remove dust and other particles on the bottom mirror of the LI-7700. The parameters chosen for this washing cycle were suitable for cleaning the bottom mirror during normal conditions at the site. However, the short period of intense winds on the second day of measurements could not be predicted and resulted in much more dust accumulation on the LI-7700 mirror than this washing cycle could remove. If a more frequent washing cycle had been implemented, loss of data would have occurred because the spinning motor that is activated during the washing cycle causes perturbations in the pressure measurement due to the proximity of the pressure sensor to the lower mirror (LI-COR, Inc., 2010). The instrument does not have the option for a similar washing cycle for the upper mirror and any dust deposited there must be removed manually and as such, the upper mirror was not cleaned after the site was left unattended at about 15:00 MDT on 12 July until 09:00 16 July. The decrease in RSSI below 10% resulted in methane concentrations and associated fluxes that are best considered with some suspicion as being unreliable.

For the period when RSSI was greater than 10%, the range in methane concentration was from 1.98 ppm to 2.43 ppm, with a median value of 2.05 ppm. Lower methane concentrations typically were observed in the afternoon. After the RSSI had fallen below 10%, there was a drift upwards in CH_4 concentration as a result of the decreased signal strength of the LI-7700. The range in CH_4 concentration during this period of low signal strength was from 2.41 ppm to 6.53 ppm, with a median value of 3.23 ppm.

The methane concentrations measured with the LI-7700 were compared with those measured by the open-path, infrared laser gas detector that was located on the northwest side of the tailings pond. This laser gas detector was chosen for comparison because the wind direction during the measurement period was such that this detector was downwind (or at least not upwind; the presence of the complex berms at the edge of the pond made determination of the path of the wind arriving at the laser beam difficult) of the tailings pond for the majority of the measurement period. The methane concentration measured using this detector when the wind direction measured (some 800 m distant) by the sonic anemometer might be conjectured to have placed the laser path in a flow off the pond ranged from 1.82 ppm to 2.47 ppm, with a median value of 2.09 ppm. Thus the methane concentration measured with the laser gas detector agreed well with the concentration measured by the LI-7700 when the signal strength was above the lower limit of 10% (Figure 5.6). When the signal strength was below this limit, there was significant difference between the methane concentrations measured by the two methods, reaffirming the fact that the use of the LI-7700 measurements with decreased signal strength is inadvisable.

5.3.3 Methane Flux using the Eddy Covariance Technique

The eddy covariance method resulted in short term (30 min) methane fluxes (when RSSI $>$ 10%) ranging from -1.03 x 10^{-4} kg $m^{-2}day^{-1}$ to 7.07 x 10^{-5} kg $m^{-2}day^{-1}$, with a median value of 3.48 x 10^{-6} kg $m^{-2}day^{-1}$. The CH_4 flux (RSSI $>$ 10%) was positive for 71% of all measurement periods. The CH_4 emission rates (when

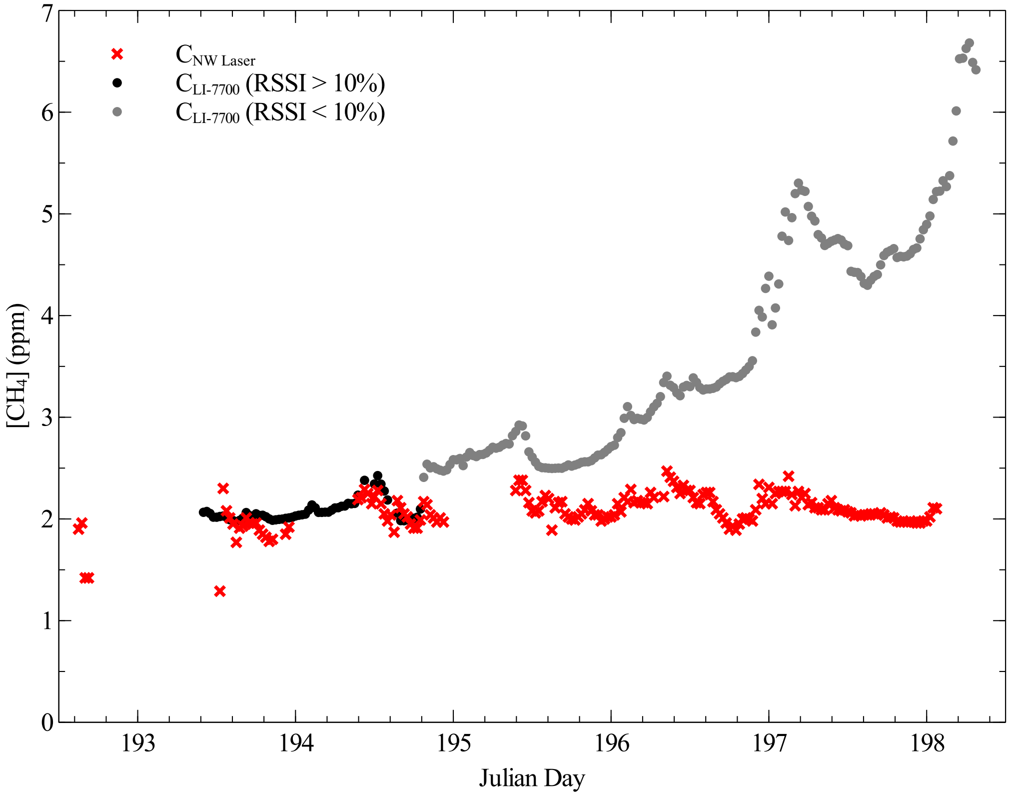

Figure 5.6: Time series of methane concentration (ppm) at the tailings pond, measured with the LI-7700, $c_{LI-7700}$ (indicating when the signal strength (RSSI) is above and below the threshold level of 10%) and the open-path, infrared laser gas detector located at the northwest corner of the tailings pond, c_{NW}.

RSSI > 10%), calculated using the estimated total area of the tailings pond, ranged from -18.0 kg hr^{-1} to 12.4 kg hr^{-1}, with a median value of 0.61 kg hr^{-1} (Figure 5.7). The offset in the measured methane density resulting from the low RSSI does not affect the raw covariance, but when applying the WPL correction, these terms are multiplied by the half-hour means of methane density. Any offset in half-hour means would directly transfer into the calculated flux and so, methane fluxes associated with low RSSI are unreliable as well. The CH_4 flux data cited above were filtered such that they met the criterion wherein the mean wind direction during that 30-minute period was over the pond (200° ± 60°). When this wind direction filter was applied, the flux footprint lay firmly over the tailings pond and the influence of other potential sources of methane nearby was negligible (according to the footprint model). The 30-minute average CH_4 emission rates were plotted against wind speed, wind direction, and CO_2 emission rates (Figure 5.8, 5.9, 5.10). No obvious correlation was noted.

5.3.4 Methane Flux using the Inverse Dispersion Technique

An estimate of the flux of methane was also conducted using the inverse dispersion method, incorporating the two open-path, infrared laser gas detectors and the meteorological measurements made at the eddy covariance tower, with the *WindTrax* software. Prior to presenting the results of this simulation, the provisos and assumptions associated with the implementation of this technique are first reviewed. An inverse dispersion analysis using *WindTrax* assumes the wind field to be horizontally homogeneous, and therefore neglects the berms around the tailings pond, as well as other realities of the site that differ from the ideal of the model. Designation of the laser paths as either being "upwind" or "downwind" of the tailings pond rests on this unverifiable (and, to say the least, doubtful) assumption in regard to the wind field. Added to this uncertainty are the unknown influences of the irregular terrain at the pond edge and the specification of the height of the laser beams above the pond surface that could only be very roughly estimated. Furthermore, in the inverse dispersion analysis, the background concentration field is assumed to be height in-

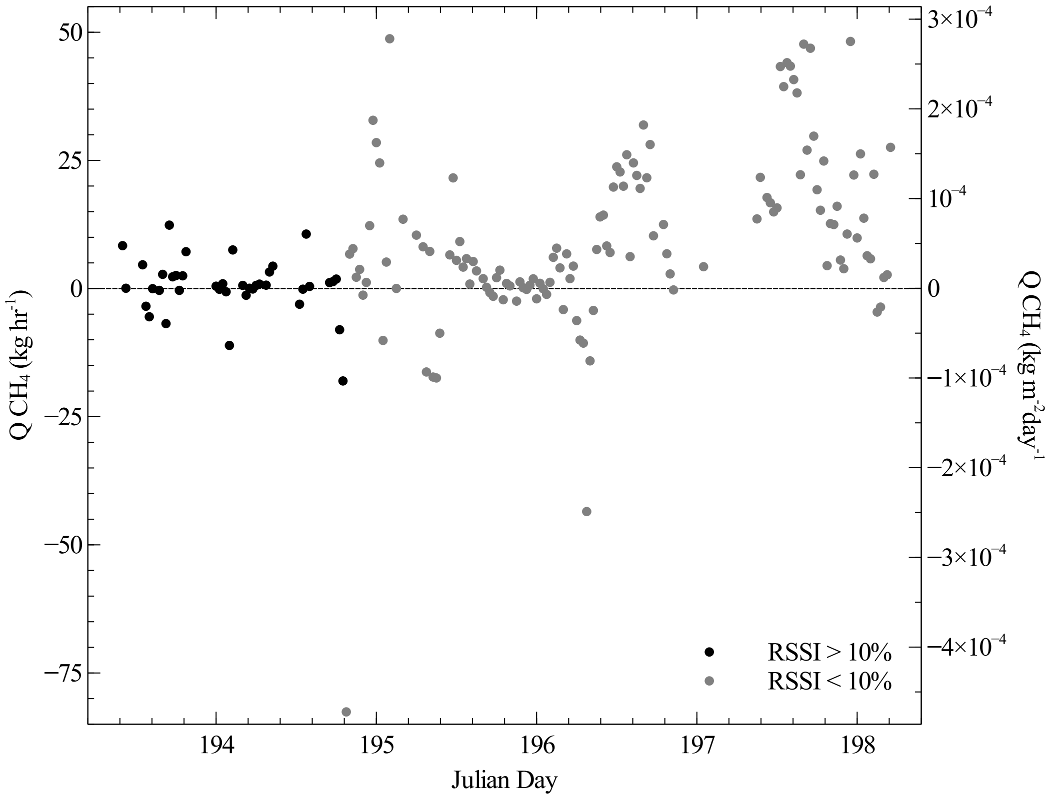

Figure 5.7: Time series of CH$_4$ emission rate (kg hr^{-1}) and flux (kg m^{-2}day^{-1}) from the tailings pond using the eddy covariance technique, indicating when the signal strength (RSSI) is above and below the threshold level of 10%. Data are filtered to only include data where the mean wind direction during the 30-minute sampling period was in an ideal direction (200° ± 60°).

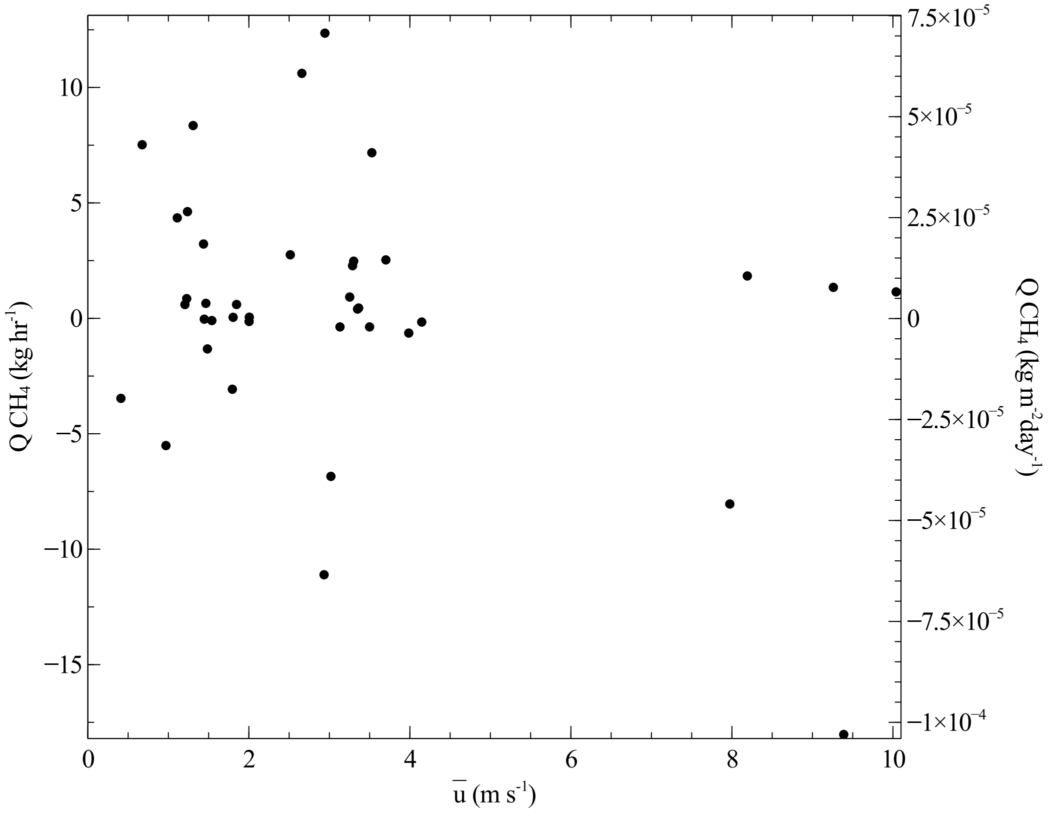

Figure 5.8: Half-hour mean methane emission rates (kg hr^{-1})and flux (kg m^{-2}day^{-1}) plotted against corresponding mean horizontal velocity post-rotation, $\overline{u}$ (m s^{-1}).

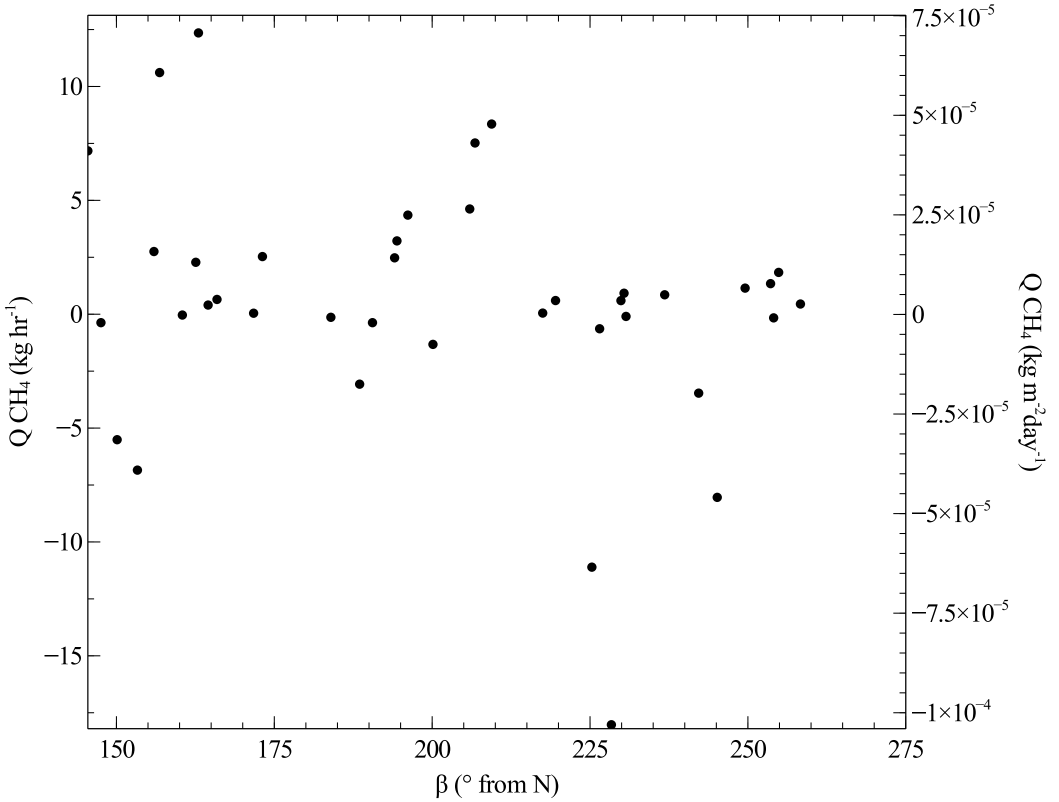

Figure 5.9: Half-hour mean methane emission rates (kg hr^{-1})and flux (kg m^{-2}day^{-1}) plotted against corresponding mean wind direction, β (° from N).

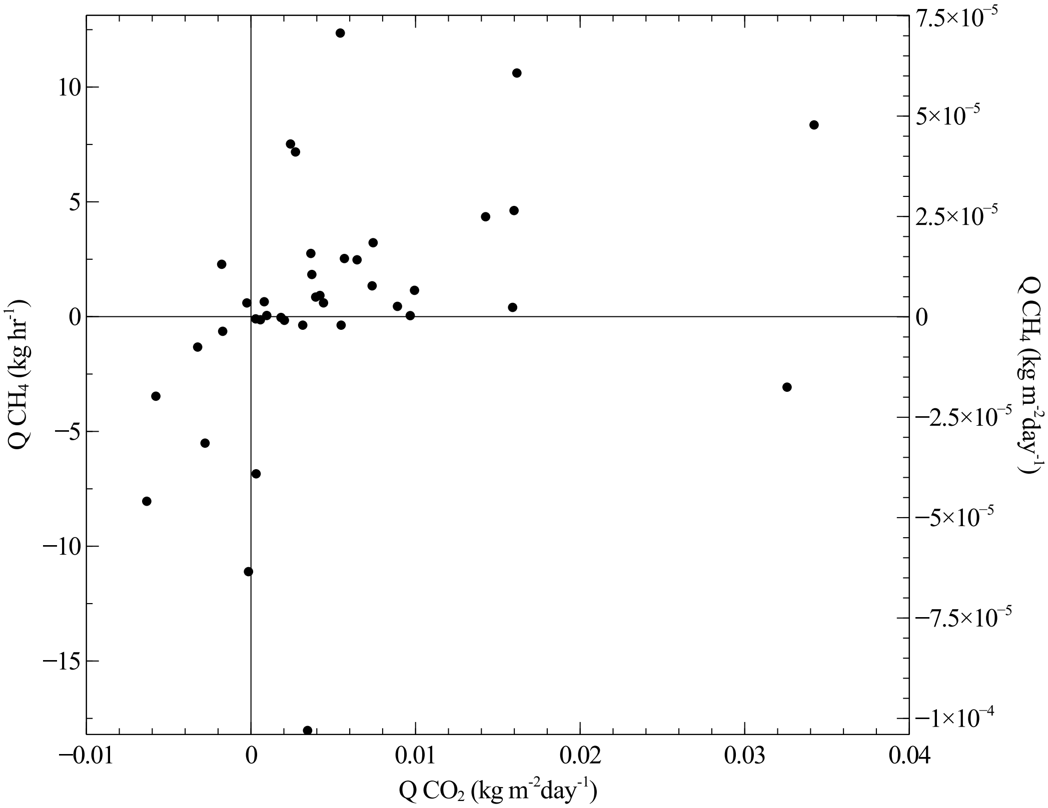

Figure 5.10: Half-hour mean methane emission rates (kg hr^{-1}) and flux (kg m^{-2} day^{-1}) plotted against corresponding mean carbon dioxide flux (kg $m^{-2}day^{-1}$).

dependent (uniform). The validity of this assumption is debatable given that there were most likely other sources nearby, either natural (swamps) or artificial (mined or disturbed sources), influencing the background concentration.

The *WindTrax* simulation was performed with N_p = 50,000 particles released from each sensor location at a height of 10 m above the pond surface. In order to represent a line average concentration, 50 source points along the laser paths were used. This analysis utilized two measured methane concentrations, the downwind laser gas detector at the northwest corner of the pond and the "upwind" laser gas detector at the southern edge of the pond, as well as the meteorological measurements made at the eddy covariance tower approximately 800 m east of the northwest laser gas detector (see Appendix E for meteorological data used as input to *WindTrax*). The simulation inferred the background methane concentration and estimated the methane flux for each input data period. To eliminate periods with the potential that MOST did not accurately describe the wind field, data periods were removed when $u_* \leq 0.15$ m s^{-1} (low wind conditions), $|L| \leq 10$ m (strongly stable or unstable atmosphere), and $z_0 \geq 0.1$ m (Flesch et al., 2007). For some wind directions, the touchdown field was not over the tailings pond or only covered a small area. Results were filtered to remove periods when the touchdown field covered less than 10% of the tailings pond, to exclude those periods that would result in unrepresentative estimates of the CH_4 flux. With an assumed laser beam height of 10 m above the tailings pond surface, the estimated CH_4 fluxes ranged from -2.19 x 10^{-3} kg m^{-2}day^{-1} to 3.28 x 10^{-3} kg m^{-2}day^{-1}, with a median value of -1.01 x 10^{-4} kg m^{-2}day^{-1}. The CH_4 emission rate, calculated using the estimated total area of the tailings pond, ranged from -3.87 x 10^{2} kg hr^{-1} to 5.81 x 10^{2} kg hr^{-1}, with median value -1.78 x 10^{1} kg hr^{-1} (Figure 5.11). The height of the laser gas detectors above the pond surface could only be roughly approximated, so the *WindTrax* simulation was performed multiple times with different specifications for the laser beam heights (ranging from 5 m to 15 m, in steps of 1 m). These simulations were performed with N_p = 5,000 particles released from each sensor location and 30 source points along the laser paths to represent a line average concentration. The median values of the emission rates estimated by these simulations were of the same order of magnitude as the median value of the original simulation results and ranged from -5.94 x 10^1 kg hr^{-1} to -2.38 x 10^1 kg hr^{-1}.

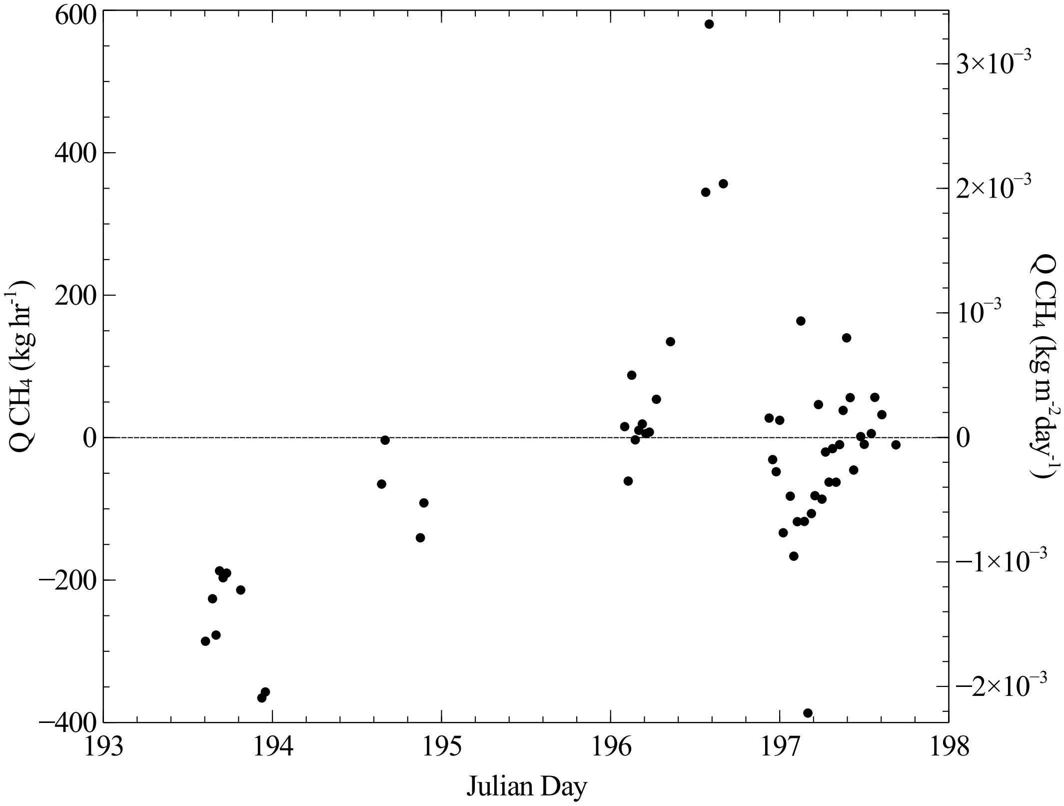

Figure 5.11: Time series of methane emission rate (kg hr^{-1}) and flux (kg m^{-2}day^{-1}) from the tailings pond estimated using *WindTrax* (filtered to exclude data where $u_* \leq 0.15$ m s^{-1}, $|L| \leq 10$ m, $z_0 \geq 0.1$ m, and fraction of the tailings pond covered by touchdowns $\leq$ 10%).

The emissions estimates resulting from the *WindTrax* analysis differed from the fluxes determined by eddy covariance by more than an order of magnitude. More data periods gave negative emission rates using this method than using eddy covariance (only approximately 40% were positive), suggesting the tailings pond was not a source of methane. The quantitative results for the methane flux from the tailings pond given by this analysis have an uncertainty that could be as high as 100%. Despite this high uncertainty, the qualitative finding that the downwind laser gas detector often showed lower concentration than the upwind detector strongly suggests a downward transport of methane to the pond. The upwind and downwind laser gas detectors, which had been calibrated by the manufacturer just days before their operation at the oil sands tailings pond, were inter-compared side-by-side for approximately 20 minutes on the last morning of the field campaign and proved very consistent, with an average percent difference between the two detectors of only 0.53% over the comparison period (Figure 5.12).

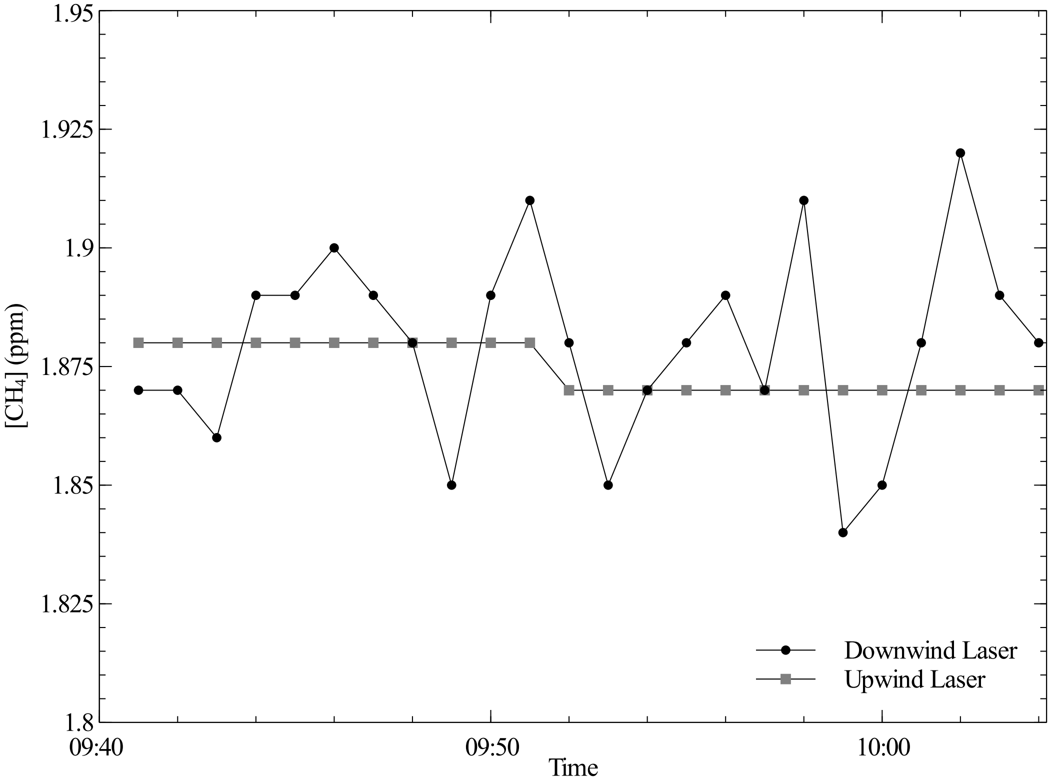

Figure 5.12: Methane concentration measurements made by the collocated laser gas detectors on the last morning of the field campaign for approximately 20 minutes.

5.3.5 Carbon Dioxide Concentration and Flux

The CO_2 concentration measured by the LI-7500A ranged from 351 ppm to 436 ppm, with a median value of 374 ppm (Figure 5.13). Lower daytime values observed are presumably due to the removal of CO_2 in the atmosphere by plants through photosynthesis. Using the eddy covariance method, the CO_2 flux from the tailings pond ranged from -3.51 x 10^{-2} kg $m^{-2}day^{-1}$ to 4.47 x 10^{-2} kg $m^{-2}day^{-1}$, with a median value of 4.69 x 10^{-3} kg $m^{-2}day^{-1}$. The emission rate, calculated using the estimated total area of the tailings pond, ranged from -6.14 x 10^3 kg hr^{-1} to 7.82 x 10^3 kg hr^{-1}, with a median value of 8.20 x 10^2 kg hr^{-1} (Figure 5.14).

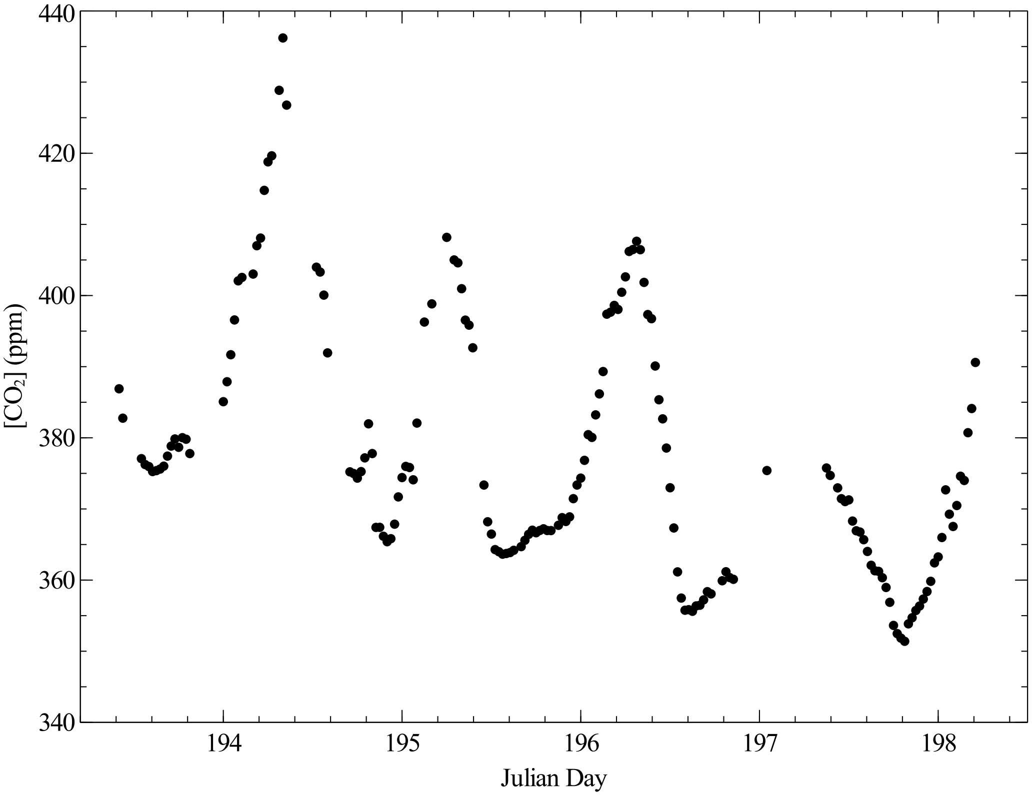

Figure 5.13: Time series of CO_2 concentration (ppm) measured at the oil sands tailings pond with the LI-7500A.

5.3.6 EddyPro Comparison

A time series data table covering 2.5 hours on 11 July was output to the datalogger at a 10 Hz acquisition frequency. Results from post-processing of this time series data were compared with results given by LICOR's EddyPro software. EddyPro processes raw time series (of wind velocities, temperature and gas concentrations) to compute fluxes of CH_4, CO_2, momentum, and latent and sensible heat. In the EddyPro software, the advanced settings allow for selection of raw data processing

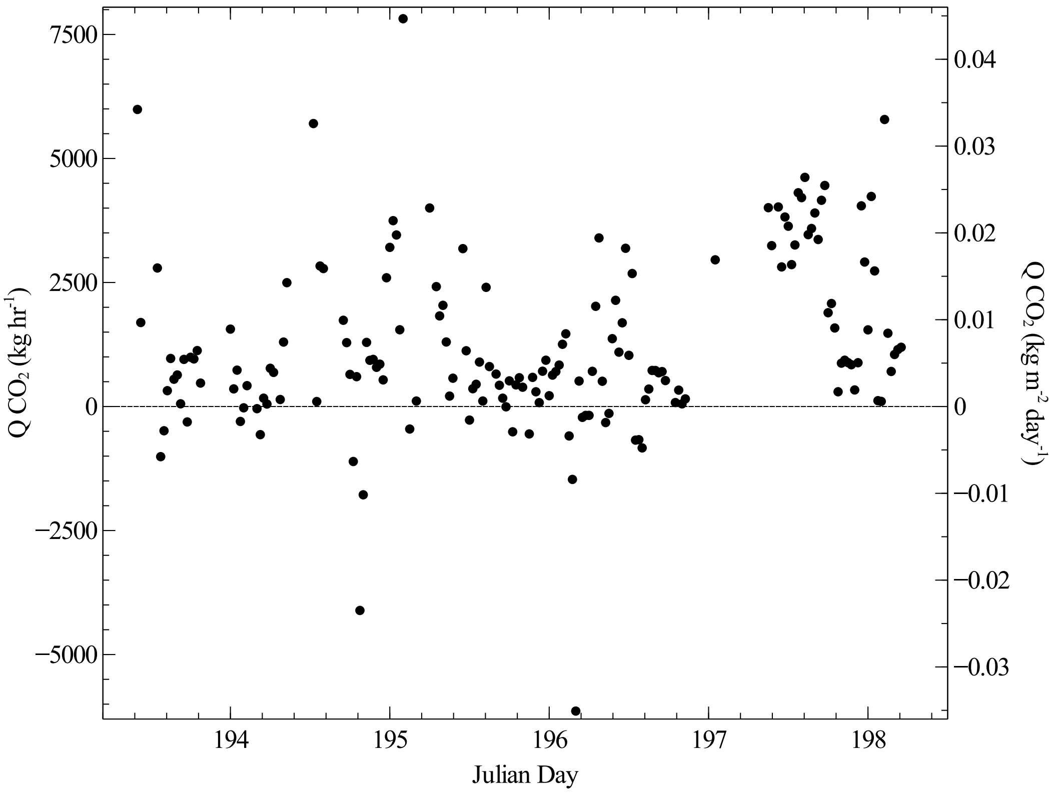

Figure 5.14: Time series of carbon dioxide emission rate (kg hr^{-1}) and flux (kg $\mathrm{m}^{-2}\mathrm{day}^{-1}$) from the tailings pond, measured using the eddy covariance technique. Data has been filtered to only include data where the mean wind direction during the 30-minute sampling period was in an ideal direction (200° ± 60°).

options. Most of the defaults were left unchanged or were set to correspond with the post-processing done with the R program of the statistics computed by the datalogger (means, standard deviations, and covariances). For instance, in EddyPro the tilt correction method was changed from the planar fit method to the double rotation method that was used in the R program and the compensation for density fluctuations was chosen to be the Webb et al. (1980) method. According to the EddyPro 4 Help and User Guide (LI-COR, Inc., 2012), the frequency response corrections compensating for the flux losses at different frequencies of turbulent transport due to physical limitations of the sensors and sensor performance are applied in EddyPro according to Moncrieff et al. (1997). This method models all major sources of flux attenuation by means of a mathematical formulation and is the suggested method for open-path systems (LI-COR, Inc., 2012). The EddyPro analysis was carried out first without applying the frequency response correction and the results were compared with the fluxes calculated using the program developed in R without the frequency response correction applied to the covariances. The results from both analyses agreed well, with a median percent difference between the two methods for CO_2 flux and CH_4 flux of 0.68% and 0.70%, respectively (Table 5.1). When the frequency response correction was applied, there was a larger difference between the two methods, with the fluxes computed by the R program being of higher magnitude. The median percent differences between the CO_2 and CH_4 fluxes were 1.69% and 9.71%, respectively.

Table 5.1: EddyPro and R comparison of CO_2 and CH_4 fluxes. Comparison is made between the two methods when frequency response corrections are both applied and not applied. Frequency response corrections are applied to measured fluxes to compensate for flux losses at different frequencies of turbulent transport resulting from the physical limitations of the sensors and sensor performance.

	CO_2 Flux (kg m^2 day^{-1})				CH_4 Flux (kg m^2 day^{-1})			
	Correction Not Applied		Correction Applied		Correction Not Applied		Correction Applied	
Time	R	EddyPro	R	EddyPro	R	EddyPro	R	EddyPro
11:30	1.33 x 10^{-2}	1.30 x 10^{-2}	1.36 x 10^{-2}	1.33 x 10^{-2}	-1.39 x 10^{-5}	-1.39 x 10^{-5}	-1.87 x 10^{-5}	-1.62 x 10^{-5}
12:00	1.21 x 10^{-2}	1.21 x 10^{-2}	1.21 x 10^{-2}	1.23 x 10^{-2}	6.76 x 10^{-6}	6.71 x 10^{-6}	4.05 x 10^{-6}	5.57 x 10^{-6}
12:30	2.79 x 10^{-2}	2.78 x 10^{-2}	2.91 x 10^{-2}	2.86 x 10^{-2}	-1.88 x 10^{-5}	-1.90 x 10^{-5}	-2.46 x 10^{-5}	-2.19 x 10^{-5}
13:00	1.61 x 10^{-2}	1.61 x 10^{-2}	1.68 x 10^{-2}	1.65 x 10^{-2}	2.66 x 10^{-5}	2.64 x 10^{-5}	2.71 x 10^{-5}	2.71 x 10^{-5}
13:30	-6.22 x 10^{-3}	-6.31 x 10^{-3}	-7.00 x 10^{-3}	-6.74 x 10^{-3}	-2.04 x 10^{-5}	-2.07 x 10^{-5}	-2.37 x 10^{-5}	-2.31 x 10^{-5}
14:00	-3.11 x 10^{-3}	-3.20 x 10^{-3}	-4.06 x 10^{-3}	-3.54 x 10^{-3}	-3.14 x 10^{-5}	-3.17 x 10^{-5}	-3.73 x 10^{-5}	-3.50 x 10^{-5}

To apply the frequency response correction, EddyPro computes the cospectrum for each half-hour averaging period of the time series data then calculates the cospectral loss that must have resulted from the imperfections of the instrument set-up (e.g., sonic and gas sensor path lengths, path separations, etc.). This calculation is performed by specifying transfer functions that describe how these deficiencies affect the calculated cospectra and whose product is multiplied by the calculated cospectra to obtain the attenuated cospectra. The ratio of the integrated true cospectra to the integrated attenuated cospectra gives a correction factor that is applied to the measured flux to give the "true" flux. The frequency response correction in the R program assumes the cospectral model of Kaimal et al. (1972) in neutral conditions based on flat terrain to be a good representation of the true spectral shape (see Appendix B2 for a detailed description). Kaimal et al. (1972) show that the cospectral shape does not vary much in unstable conditions. This model cospectrum was developed for situations closer to the ideal than the experimental site for which it has been applied. Any deviation in the shape of the true atmospheric cospectra from the model cospectra used would result in erroneous estimates of the proper flux correction for instrument frequency responses, path lengths and path separations. This could partly explain the difference between the flux estimates given by EddyPro and those calculated using the post-processing program written in R. Further discrepancies exist between the two methods in regards to the types of frequency response transfer functions applied to obtain the attenuated cospectra. EddyPro includes spectral corrections for both high-pass filtering and low-pass filtering effects that are not included in the correction done in the R program. The correction of high-pass filtering effects includes the effects of the finite averaging time, termed the block averaging transfer function. This transfer function was not applied in the R program as there was presumably not much cospectral power at low frequencies that was not caught with the 30-minute averaging interval used. The low-pass filtering effects apply a correction for flux spectral losses in the high frequency range. Both programs apply transfer functions for scalar path averaging and sensor separation, but EddyPro also includes transfer functions for sonic path averaging and dynamic frequency response of the sonic anemometer and gas sensors. Investigations into the influence of these latter transfer functions led to the conclusion that they were negligible, and therefore they were not implemented in the R program.

5.3.7 Flux Footprint

The footprint is the (largely upwind) area of the surface that contributes to the mean vertical flux measured by the sensor. Schmid (1994) presented the characteristic dimensions of the 50% source area (i.e., the area responsible for 50% of the measured flux) as a function of the measurement height, the roughness length, the Obukhov length, and the level of crosswind turbulence. The parameterized statistical model of the scalar flux-source area model (mini-FSAM) was used to estimate the source area of the flux measurements for each time period. The resultant 50% source area estimate for the 12:00-12:30 MDT 13 July time period had dimensions consistent with the average dimensions of the source areas estimated for all time periods (Figure 5.15). The area bounded by this 50% boundary was calculated to be approximately 6.1 x 10^3 m^2.

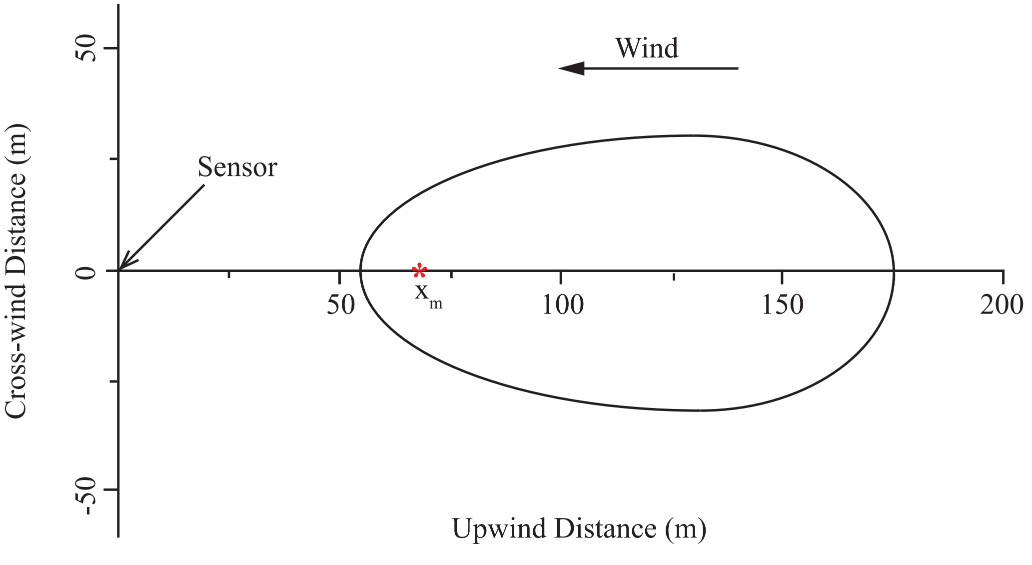

Figure 5.15: Schematic representation of the 50% source area for 12:00-12:30 on 13 July. Location of upwind distance with the maximum influence on the sensor marked by x_m.

Most of the estimated 50% source areas did not extend further than 280 m from the eddy covariance tower. This model also gave the approximate upwind distance to the location of maximum influence, and the median value of this distance was found to be 61 m upwind from the sensors. For most wind directions, the pond was large enough so that the upwind area contributing to the fluxes, as calculated using the Schmid (1994) 50% source area model, did not extend further than the pond boundaries.

Hsieh et al. (2000) developed an approximate analytical model to estimate the 90% flux fetch. Similar to the Schmid (1994) mini-FSAM, this model relates the fetch to atmospheric stability, measurement height, and the surface roughness length. The median value for the 90% flux fetch was estimated to be a distance of 880 m from the eddy covariance mast.

5.4 Discussion

A significant percentage of the methane fluxes determined by the eddy covariance measurements made at the tailings pond were negative, implying that the tailings pond was not consistently acting as a source of methane. Hypothetical reasons for the negative methane fluxes include poor instrument performance (particularly the LI-7700 methane analyzer and sonic anemometer), an undesirable footprint for the flux measurements, or errors in the post-processing steps performed to determine the flux of methane.

The possibility that these apparent negative fluxes are a result of poor instrument deployment or performance has been patiently considered. If the LI-7700 methane analyzer had not been calibrated correctly and was not reporting the correct methane concentration, this could have impacted the validity of the flux measurements. However, the LI-7700 was new and newly calibrated, and had responded as expected to trace gases in the lab prior to the field campaign. The consistency of the open-path, infrared laser gas detector providing methane concentration measurements at the downwind edge of the tailings pond (the northwest corner, approximately

800 m from the eddy covariance tower where the LI-7700 was mounted) with the methane concentration measurements made with the LI-7700 (reported earlier, see Figure 5.6) provided further confidence that the LI-7700 was reporting the correct methane concentrations.

A question one must ask oneself in relation to these eddy fluxes is the quality of measurements made by the sonic anemometer. The velocity statistics provided by the sonic anemometer (e.g., σ_w/u_*, reported earlier, see Figure 5.5) fit very nicely the expected pattern for an undisturbed surface layer. Furthermore, the eddy covariance tower was placed so as to provide the sensors with more than 2 km of upwind pond surface, with only a very mild flow disturbance caused by the low berm at the edge of the pond.

If (as believed) the negative fluxes observed were not a result of poor instrument performance, there remains the question of whether they are a result of an undesirable footprint of the flux measurements. A footprint analysis was performed to determine the approximate surface area contributing to the flux measurements made at the eddy covariance tower. This analysis consisted of the 50% source area model of Schmid (1994) and the 90% flux fetch model of Hsieh et al. (2000). Methane flux outliers (i.e., unusually large negative values) were not found to be associated with unusual or unacceptable flux footprints that extended farther than the pond extent.

Having established that the instruments were performing as expected and making measurements of the flux from a footprint lying over the pond, it is necessary to consider possible errors in the post-processing steps used in the determination of the methane fluxes. The EddyPro software was used as a verification of the post-processing and flux calculations performed in the R program. The EddyPro analysis of the raw time series data was consistent with the analysis done by the R program (reported earlier, see Table 5.1). Despite the small discrepancy between the two methods when the frequency response corrections were applied to the flux measurements (to account for deficiencies in instrument set-up), there was regular agreement as to which data periods had negative fluxes. The application of the inverse dispersion technique through the *WindTrax* simulations also gave negative emissions rates, consistent with the upwind laser gas detector regularly reporting higher methane concentrations than the downwind detector. However, as indicated earlier, one must have some reservation about the estimates provided by the inverse dispersion technique. In particular, the assumption inherent to *WindTrax* that the wind field was horizontally homogeneous, neglecting the influence of berms at the edges of the tailings pond, cannot be verified. Furthermore, the assumption that the background methane concentration was uniform may not have been true.

One is left without any reason to discount these eddy covariance measurements.

Chapter 6

Conclusion

Methane and carbon dioxide flux measurements were made during a brief field campaign at an oil sands tailings pond. The methodologies adopted in this field campaign were the eddy covariance and inverse dispersion techniques. These measurements were performed in order to investigate the feasibility of using a micrometeorological technique as an alternative to the traditional flux chamber approach to quantify the emission rate of methane from a tailings pond. Exploring such alternatives is of interest because these micrometeorological techniques effectively sample a larger surface area at higher temporal resolution than the flux chamber approach allows.

The eddy covariance method resulted in a median methane emission rate of 0.61 kg hr^{-1} or 3.48 x 10^{-6} kg $\text{m}^{-2}\text{day}^{-1}$ (with negative emission rates making up approximately 30% of these results). Variation in methane emission rates was not found to correlate with meteorological variables tested (wind direction and wind speed) or with the emission rate of carbon dioxide. It was established that the negative fluxes were unlikely to result from poor performance of either the methane analyzer or the sonic anemometer. The methane concentration measurements were consistent with those reported by the laser at the northwest corner of the pond and the velocity statistics provided by the sonic anemometer fit the expected pattern for an undisturbed surface layer. Neither an undesirable flux footprint nor the calculations performed in post-processing of the data were found to be responsible for the unexpected negative emission rates observed. The total length of the field campaign was only six days, with only two days giving reliable methane data from the eddy covariance instruments. A longer field campaign with more consistent access to the site, would have allowed for additional days giving reliable data and a more representative estimate of emissions from the tailings pond that would further take into account the temporal variability of the environment.

As a subsidiary component of this research project, methane emission rates from the tailings pond were also estimated using the inverse dispersion method. This technique estimated negative emission rates for even more data periods than did the eddy covariance method. The magnitude of the fluxes resulting from this technique and the eddy covariance fluxes were found to differ by more than an order of magnitude. However, the inverse dispersion technique as implemented in *WindTrax* is more suitable for small area sources than for the large tailings pond it was employed at. The assumption that the wind statistics provided by the sonic anemometer were representative of the entire pond may not have been correct, and the presence of berms at the edges of the pond was neglected even though they would have disturbed the flow. Any deviation from the ideal flow that is assumed by the model results in a loss of accuracy in the *WindTrax* emissions estimates.

The results of the field campaigns of this study have demonstrated that the eddy covariance method gives a useful indication of the emission rate of surface area sources, provided the flow is undisturbed and the flux footprint is over the source area of interest. The application of the inverse dispersion technique, on the other hand, is subject to a loss of accuracy when the realities of the site deviate from the ideal assumed by the model used in this technique. As a result, there is less confidence in the emissions estimates resulting from the inverse dispersion technique applied under such conditions.

References

Arya, S. P. (2001). *Introduction to Micrometeorology.* Academic Press, San Diego, 2nd edition.

Burba, G. and Anderson, D. (2010). *A Brief Practical Guide to Eddy Covariance Measurements: Principles and Workflow Examples for Scientific and Industrial Applications.* Version 1.0.1. LI-COR, Inc., Lincoln, NE.

Denmead, O. T. (2008). Approaches to measuring fluxes of methane and nitrous oxide between landscapes and the atmosphere. *Plant Soil*, 309:5–24.

Dyer, A. J. (1974). A review of flux-profile relationships. *Boundary Layer Meteorology*, 7:363–372.

Dyer, A. J. and Bradley, E. F. (1982). An alternative analysis of flux-gradient relationships at the 1976 ITCE. *Boundary Layer Meteorology*, 22(1):3–19.

Fedorak, P. M., Coy, D. L., Salloum, M. J., and Dudas, M. J. (2002). Methanogenic potential of tailings samples from oil sands extraction plants. *Canadian Journal of Microbiology*, 2(3):199–211.

Ferrara, R. M., Loubet, B., Di Tommasi, P., Bertolini, T., Magliulo, V., Cellier, P., Eugster, W., and Rana, G. (2012). Eddy covariance measurement of ammonia fluxes: Comparison of high frequency correction methodologies. *Agricultural and Forest Meteorology*, 158-159:30–42.

Flesch, T. K., Wilson, J. D., Harper, L. A., and Crenna, B. P. (2005). Estimating gas emissions from a farm with an inverse dispersion technique. *Atmospheric Environment*, 39:4863–4874.

Flesch, T. K., Wilson, J. D., Harper, L. A., Todd, R. W., and Cole, N. A. (2007). Determining ammonia emissions from a cattle feedlot with an inverse dispersion technique. *Agricultural and Forest Meteorology*, 144:139–155.

Flesch, T. K., Wilson, J. D., and Yee, E. (1995). Backward-time Lagrangian stochastic dispersion models and their application to estimate gaseous emissions. *Journal of Applied Meteorology*, 34:1320–1332.

Gao, Z., Desjardins, R. L., and Flesch, T. K. (2009). Comparison of a simplified micrometeorological mass difference technique and an inverse dispersion technique for estimating methane emissions from small area sources. *Agricultural and Forest Meteorology*, 149:891–898.

Hayes, R. E. (2004). Catalytic solutions for fugitive methane emissions in the oil and gas sector. *Chemical Engineering Science*, 59:4073–4080.

Horst, T. W. (1999). The footprint for estimation of atmosphere-surface exchange fluxes by profile techniques. *Boundary Layer Meteorology*, 90:171–188.

Horst, T. W. and Weil, J. C. (1992). Footprint estimation for scalar flux measurements in the atmospheric surface layer. *Boundary Layer Meteorology*, 59:279–296.

Hsieh, C., Katul, G., and Chi, T. (2000). An approximate analytical model for footprint estimation of scalar fluxes in thermally stratified atmospheric flows. *Advances in Water Resources*, 23:765–772.

Intergovernmental Panel on Climate Change (2007). *Climate change 2007: The scientific basis*. Cambridge University Press, Cambridge, UK.

Kaimal, J. C., Wyngaard, J. C., Izumi, Y., and Cote, O. R. (1972). Spectral characteristics of surface-layer turbulence. *Quart. J. R. Met. Soc.*, 98:563–589.

Laubach, J. and Kelliher, F. M. (2004). Measuring methane emission rates of a dairy cow herd by two micrometeorological techniques. *Agricultural and Forest Meteorology*, 125:279–303.

LI-COR, Inc. (2009). *LI-7500A Open-path CO2/H2O Gas Analyzer Instruction Manual*. LI-COR, Inc., Lincoln, NE.

LI-COR, Inc. (2010). *LI-7700 Open-path CH4 Analyzer Instruction Manual*. LI-COR, Inc., Lincoln, NE.

LI-COR, Inc. (2012). *EddyPro 4 Help and User's Guide*. LI-COR, Inc., Lincoln, NE.

Mahzabin, T. (2012). Quantifying methane emission from surface sources using the backward Lagrangian stochastic method. Master's thesis, University of Alberta.

McDermitt, D., Burba, G., Xu, L., Anderson, T., Komissarov, A., Riensche, B., Schedlbauer, J., Starr, G., Zona, D., Oechel, W., Oberbauer, S., and Hastings, S. (2011). A new low-power, open-path instrument for measuring methane flux by eddy covariance. *Appl Phys B*, 102:391–405.

Moncrieff, J. B., Massheder, J. M., de Bruin, H., Elbers, J., Friborg, T., Heusinkveld, B., Kabat, P., Scott, S., Soegaard, H., and Verhoef, A. (1997). A system to measure surface fluxes of momentum, sensible heat, water vapour, and carbon dioxide. *Journal of Hydrology*, 188-189:589–611.

Moore, C. J. (1986). Frequency response corrections for eddy correlation systems. *Boundary Layer Meteorology*, 37:17–35.

Penner, T. and Foght, J. M. (2010). Mature fine tailings from oil sands processing harbour diverse methanogenic communities. *Can. J. Microbiol.*, 56(6):459–470.

Schmid, H. P. (1994). Source areas for scalars and scalar fluxes. *Boundary Layer Meteorology*, 67:293–318.

Schneising, O., Buchwitz, M., Reuter, M., Heymann, J., Bovensmann, H., and Burrows, J. P. (2011). Long-term analysis of carbon dioxide and methane column-averaged mole fractions retrieved from SCIAMACHY. *Atmos. Chem. Phys.*, 11:2863–2880.

Schotanus, P., Nieuwstadt, F. T. M., and de Bruin, H. A. R. (1983). Temperature measurement with a sonic anemometer and its application to heat and moisture fluxes. *Boundary Layer Meteorology*, 26:81–93.

Schuepp, P. H., Leclerc, M. Y., MacPherson, J. I., and Desjardins, R. L. (1990). Footprint prediction of scalar fluxes from analytical solutions of the diffusion equation. *Boundary Layer Meteorology*, 50:355–373.

Siddique, T., Gupta, R., Fedorak, P. M., MacKinnon, M. D., and Foght, J. M. (2008). A first approximation kinetic model to predict methane generation from an oil sands tailings settling basin. *Chemosphere*, 72(10):1573–1580.

Siddique, T., Penner, T., Semple, K., and Foght, J. M. (2011). Anaerobic biodegradation of longer-chain n-alkanes coupled to methane production in oil sands tailings. *Environ. Sci. Technol.*, 45(13):5892–5899.

Stull, R. B. (1988). *An Introduction to Boundary Layer Meteorology.* Kluwer Academic Publishers.

Thomson, D. J. (1987). Criteria for the selection of stochastic models of particle trajectories in turbulent flows. *J. Fluid Mech.*, 180:529–556.

Webb, E. K. (1970). Profile relationships: The log-linear range and extension to strong stability. *Quart. J. R. Met. Soc.*, 96:67–90.

Webb, E. K., Pearman, G. I., and Leuning, R. (1980). Correction of flux measurements for density effects due to heat and water vapour transfer. *Quart. J. R. Met. Soc.*, 106:85–100.

Wilczak, J. M., Oncley, S. P., and Stage, S. A. (2001). Sonic anemometer tilt correction algorithms. *Boundary Layer Meteorology*, 99:127–150.

Wilson, J. D. (2008). Monin-Obukhov functions for standard deviations of velocity. *Boundary Layer Meteorology*, 129:353–369.

Wilson, J. D., Flesch, T. K., and Harper, L. A. (2001). Micro-meteorological methods for estimating surface exchange with a disturbed windflow. *Agricultural and Forest Meteorology*, 107:207–225.

Wilson, J. D. and Sawford, B. L. (1996). Review of Lagrangian stochastic models for trajectories in the turbulent atmosphere. *Boundary Layer Meteorology*, 78:191–210.

Wuebbles, D. J. and Hayhoe, K. (2002). Atmospheric methane and global change. *Earth Science Reviews*, 57:177–210.

Yusuf, R. O., Noor, Z. Z., Abba, A. H., Hassan, M. A. A., and Din, M. F. M. (2012). Greenhouse gas emissions: quantifying methane emissions from livestock. *American J. of Engineering and Applied Sciences*, 5(1):1–8.

Appendix A

R Program

```
#————————————————————————————————
#Program: Post-processing of eddy covariance data

#This program performs the required post-processing corrections to the eddy covariance data recorded
on the
#datalogger during the field campaign and calculates the flux of methane and carbon dioxide.

#Author: C. Brown
#Last Revised: 09 April 2013
#————————————————————————————————

# Constants:
MWch4<- 16.04 #molecular weight of CH4 [g mol^-1]
R<- 8.3143e-3   #Universal gas constant [kPa m^3 K^-1 mol^-1]
RD<- R/29       #Gas constant for dry air [kPa m^3 K^-1 g^-1]
RV<- R/18       #Gas constant for water vapour [kPa m^3 K^-1 g^-1]
CP<- 1004.67    #Estimate of heat capacity of air [J kg^-1 K^-1]
LV<- 2.440e6    #Estimate of latent heat of vapourization [J kg^-1]
mu<- 29/18      #Ratio of the molecular weight of dry air to that of water vapour
kv<- 0.4        #von Karman constant
g<- 9.81        #gravitational acceleration [m s^-2]

#——————————————————————————
#Read in data file containing means, standard deviations, and covariances
data<- read.csv(”flux_datafile.csv”)
#——————————————————————————
# Organize data and get correct units
RSSI_avg<- data[,70]
Ts<- data[,9]
press<- data[,33]
Tkelvin<- Ts+273.16
rho<- press*1000.0/(287.0*Tkelvin) #kg m^-3
co2_7500mgm3<- data[,14]
co2_7500gm3<- co2_7500mgm3*10^-3
h2o_7500gm3<- data[,19]
h2omean<- h2o_7500gm3
rhoco2<- co2_7500gm3*10^-3 #kg m^-3
rhov<- h2o_7500gm3*10^-3 #kg m^-3
ch4_7700_mmolm3<- data[,61]
ch4_7700_mgm3<- ch4_7700_mmolm3*16.04
```

```
ch4_7700_gm3<- ch4_7700_mgm3*10^-3
dch4<- ch4_7700_mmolm3
Rxx<- (data[,25])^2
Rxy<- data[,26]
Rxz<- data[,27]
Ryy<- (data[,29])^2
Ryz<- data[,30]
Rzz<- (data[,32])^2
uco2<- data[,16]*10^-6 #kg m^-2 s^-1
vco2<- data[,17]*10^-6
wco2<- data[,18]*10^-6
uh2o<- data[,21]*10^-3
vh2o<- data[,22]*10^-3
wh2o<- data[,23]*10^-3
uT<- data[,11]
vT<- data[,12]
wT<- data[,13]
uch4<- data[,63] #mmol m^-2 s^-1
vch4<- data[,64]
wch4<- data[,65]
u_prerotate<- data[,24]
v_prerotate<- data[,28]
w_prerotate<- data[,31]
wT_prerotate<- wT
wh2o_prerotate<- wh2o
wco2_prerotate<- wco2
wch4_prerotate<- wch4
#——————————————————————————
#Coordinate rotation function
rotate<- function(U, V, W, Rxx, Rxy, Rxz, Ryy, Ryz, Rzz, T, co2, h2o, ch4, uT, vT, wT, uco2, vco2, wco2,
uh2o, vh2o, wh2o, uch4, vch4, wch4, phi)(
    meansq<- matrix(NA,3,3) #create mean square velocity tensor
    meansq[1,1]<- Rxx+U^2
    meansq[2,2]<- Ryy+V^2
    meansq[3,3]<- Rzz+W2̂
    meansq[1,2]<- Rxy+U*V
    meansq[1,3]<- Rxz+U*W
    meansq[2,3]<- Ryz+V*W
    meansq[3,2]<- meansq[2,3]
    meansq[2,1]<- meansq[1,2]
    meansq[3,1]<- meansq[1,3]
    total_ht_flx<- matrix(NA,1,3)
    total_ht_flx[1,1]<- uT+U*T
    total_ht_flx[1,2]<- vT+V*T
    total_ht_flx[1,3]<- wT+W*T
    total_co2_flx<- matrix(NA,1,3)
    total_co2_flx[1,1]<- uco2+U*co2
    total_co2_flx[1,2]<- vco2+V*co2
```

```
total_co2_flx[1,3]<- wco2+W*co2
total_h2o_flx<- matrix(NA,1,3)
total_h2o_flx[1,1]<- uh2o+U*h2o
total_h2o_flx[1,2]<- vh2o+V*h2o
total_h2o_flx[1,3]<- wh2o+W*h2o
total_ch4_flx<- matrix(NA,1,3)
total_ch4_flx[1,1]<- uch4+U*ch4
total_ch4_flx[1,2]<- vch4+V*ch4
total_ch4_flx[1,3]<- wch4+W*ch4
theta<- atan2(V,U)
u1<- U*cos(theta)+V*sin(theta)
v1<- -U*sin(theta)+V*cos(theta)
w1<- W
meansq_1<- matrix(NA,3,3)
meansq_1[1,1]<- meansq[1,1]*cos(theta)*cos(theta)+meansq[2,2]*sin(theta)*sin(theta)
    + 2.0*meansq[1,2]*sin(theta)*cos(theta)
meansq_1[2,2]<- meansq[1,1]*sin(theta)*sin(theta)+meansq[2,2]*cos(theta)*cos(theta)
    - 2.0*meansq[1,2]*sin(theta)*cos(theta)
meansq_1[3,3]<- meansq[3,3]
meansq_1[1,2]<- (meansq[2,2]-meansq[1,1])*sin(theta)*cos(theta)
    +meansq[1,2]*(cos(theta)*cos(theta)-sin(theta)*sin(theta))
meansq_1[1,3]<- meansq[1,3]*cos(theta)+meansq[2,3]*sin(theta)
meansq_1[2,3]<- -meansq[1,3]*sin(theta)+meansq[2,3]*cos(theta)
total_ht_flx_1<- matrix(NA,1,3)
total_ht_flx_1[1,1]<- total_ht_flx[1,1]*cos(theta)+total_ht_flx[1,2]*sin(theta)
total_ht_flx_1[1,2]<- -total_ht_flx[1,1]*sin(theta)+total_ht_flx[1,2]*cos(theta)
total_ht_flx_1[1,3]<- total_ht_flx[1,3]
total_co2_flx_1<- matrix(NA,1,3)
total_co2_flx_1[1,1]<- total_co2_flx[1,1]*cos(theta)+total_co2_flx[1,2]*sin(theta)
total_co2_flx_1[1,2]<- -total_co2_flx[1,1]*sin(theta)+total_co2_flx[1,2]*cos(theta)
total_co2_flx_1[1,3]<- total_co2_flx[1,3]
total_h2o_flx_1<- matrix(NA,1,3)
total_h2o_flx_1[1,1]<- total_h2o_flx[1,1]*cos(theta)+total_h2o_flx[1,2]*sin(theta)
total_h2o_flx_1[1,2]<- -total_h2o_flx[1,1]*sin(theta)+total_h2o_flx[1,2]*cos(theta)
total_h2o_flx_1[1,3]<- total_h2o_flx[1,3]
total_ch4_flx_1<- matrix(NA,1,3)
total_ch4_flx_1[1,1]<- total_ch4_flx[1,1]*cos(theta)+total_ch4_flx[1,2]*sin(theta)
total_ch4_flx_1[1,2]<- -total_ch4_flx[1,1]*sin(theta)+total_ch4_flx[1,2]*cos(theta)
total_ch4_flx_1[1,3]<- total_ch4_flx[1,3]
meansq_1[3,2]<- meansq_1[2,3]
meansq_1[2,1]<- meansq_1[1,2]
meansq_1[3,1]<- meansq_1[1,3]
# done first rotation, have first intermediate mean, mean-square tensors
phi<- atan2(w1,u1)
u2<- u1*cos(phi)+w1*sin(phi)
v2<- v1
w2<- -u1*sin(phi)+w1*cos(phi)
meansq_2<- matrix(NA,3,3)
```

```
meansq_2[1,1]<- meansq_1[1,1]*cos(phi)*cos(phi)+meansq_1[3,3]*sin(phi)*sin(phi)
    +2.0*meansq_1[1,3]*sin(phi)*cos(phi)
meansq_2[2,2]<- meansq_1[2,2]
meansq_2[3,3]<- meansq_1[1,1]*sin(phi)*sin(phi)+meansq_1[3,3]*cos(phi)*cos(phi)
    -2.0*meansq_1[1,3]*sin(phi)*cos(phi)
meansq_2[1,2]<- meansq_1[1,2]*cos(phi)+meansq_1[2,3]*sin(phi)
meansq_2[1,3]<- meansq_1[1,3]*(cos(phi)*cos(phi)-sin(phi)*sin(phi))
    +(meansq_1[3,3]-meansq_1[1,1])*sin(phi)*cos(phi)
meansq_2[2,3]<- -meansq_1[1,2]*sin(phi)+meansq_1[2,3]*cos(phi)
total_ht_flx_2<- matrix(NA,1,3)
total_ht_flx_2[1,1]<- total_ht_flx_1[1,1]*cos(phi)+total_ht_flx_1[1,3]*sin(phi)
total_ht_flx_2[1,2]<- total_ht_flx_1[1,2]
total_ht_flx_2[1,3]<- -total_ht_flx_1[1,1]*sin(phi)+total_ht_flx_1[1,3]*cos(phi)
total_co2_flx_2<- matrix(NA,1,3)
total_co2_flx_2[1,1]<- total_co2_flx_1[1,1]*cos(phi)+total_co2_flx_1[1,3]*sin(phi)
total_co2_flx_2[1,2]<- total_co2_flx_1[1,2]
total_co2_flx_2[1,3]<- -total_co2_flx_1[1,1]*sin(phi)+total_co2_flx_1[1,3]*cos(phi)
total_h2o_flx_2<- matrix(NA,1,3)
total_h2o_flx_2[1,1]<- total_h2o_flx_1[1,1]*cos(phi)+total_h2o_flx_1[1,3]*sin(phi)
total_h2o_flx_2[1,2]<- total_h2o_flx_1[1,2]
total_h2o_flx_2[1,3]<- -total_h2o_flx_1[1,1]*sin(phi)+total_h2o_flx_1[1,3]*cos(phi)
total_ch4_flx_2<- matrix(NA,1,3)
total_ch4_flx_2[1,1]<- total_ch4_flx_1[1,1]*cos(phi)+total_ch4_flx_1[1,3]*sin(phi)
total_ch4_flx_2[1,2]<- total_ch4_flx_1[1,2]
total_ch4_flx_2[1,3]<- -total_ch4_flx_1[1,1]*sin(phi)+total_ch4_flx_1[1,3]*cos(phi)
meansq_2[3,2]<- meansq_2[2,3]
meansq_2[2,1]<- meansq_2[1,2]
meansq_2[3,1]<- meansq_2[1,3]
# done second rotation, have second intermediate mean, mean-square tensors
psi<- 0.5*atan2((2.0*meansq_2[2,3]),(meansq_2[2,2]-meansq_2[3,3]))
u3<- u2
v3<- v2*cos(psi)+w2*sin(psi)
w3<- -v2*sin(psi)+w2*cos(psi)
meansq_3<- matrix(NA,3,3)
meansq_3[1,1]<- meansq_2[1,1]
meansq_3[2,2]<- meansq_2[2,2]*cos(psi)*cos(psi)+meansq_2[3,3]*sin(psi)*sin(psi)
    +2.0*meansq_2[2,3]*sin(psi)*cos(psi)
meansq_3[3,3]<- meansq_2[2,2]*sin(psi)*sin(psi)+meansq_2[3,3]*cos(psi)*cos(psi)
    -2.0*meansq_2[2,3]*sin(psi)*cos(psi)
meansq_3[1,2]<- meansq_2[1,2]*cos(psi)+meansq_2[1,3]*sin(psi)
meansq_3[1,3]<- -meansq_2[1,2]*sin(psi)+meansq_2[1,3]*cos(psi)
meansq_3[2,3]<- meansq_2[2,3]*(cos(psi)*cos(psi)-sin(psi)*cos(psi))
    +(meansq_2[3,3]-meansq_2[2,2])*sin(psi)*cos(psi)
total_ht_flx_3<- matrix(NA,1,3)
total_ht_flx_3[1,1]<- total_ht_flx_2[1,1]
total_ht_flx_3[1,2]<- total_ht_flx_2[1,2]*cos(psi)+total_ht_flx_2[1,3]*sin(psi)
total_ht_flx_3[1,3]<- -total_ht_flx_2[1,2]*sin(psi)+total_ht_flx_2[1,3]*cos(psi)
total_co2_flx_3<- matrix(NA,1,3)
```

```
    total_co2_flx_3[1,1]<- total_co2_flx_2[1,1]
    total_co2_flx_3[1,2]<- total_co2_flx_2[1,2]*cos(psi)+total_co2_flx_2[1,3]*sin(psi)
    total_co2_flx_3[1,3]<- -total_co2_flx_2[1,2]*sin(psi)+total_co2_flx_2[1,3]*cos(psi)
    total_h2o_flx_3<- matrix(NA,1,3)
    total_h2o_flx_3[1,1]<- total_h2o_flx_2[1,1]
    total_h2o_flx_3[1,2]<- total_h2o_flx_2[1,2]*cos(psi)+total_h2o_flx_2[1,3]*sin(psi)
    total_h2o_flx_3[1,3]<- -total_h2o_flx_2[1,2]*sin(psi)+total_h2o_flx_2[1,3]*cos(psi)
    total_ch4_flx_3<- matrix(NA,1,3)
    total_ch4_flx_3[1,1]<- total_ch4_flx_2[1,1]
    total_ch4_flx_3[1,2]<- total_ch4_flx_2[1,2]*cos(psi)+total_ch4_flx_2[1,3]*sin(psi)
    total_ch4_flx_3[1,3]<- -total_ch4_flx_2[1,2]*sin(psi)+total_ch4_flx_2[1,3]*cos(psi)
    meansq_3[3,2]<- meansq_3[2,3]
    meansq_3[2,1]<- meansq_3[1,2]
    meansq_3[3,1]<- meansq_3[1,3]
    U<- u2
    V<- v2
    W<- w2
    Rxx<- meansq_2[1,1]-u2*u2
    Ryy<- meansq_2[2,2]-v2*v2
    Rzz<- meansq_2[3,3]-w2*w2
    Rxy<- meansq_2[1,2]-u2*v2
    Rxz<- meansq_2[1,3]-u2*w2
    Ryz<- meansq_2[2,3]-v2*w2
    uT<- total_ht_flx_2[1,1]-u2*T
    vT<- total_ht_flx_2[1,2]-v2*T
    wT<- total_ht_flx_2[1,3]-w2*T
    uco2<- total_co2_flx_2[1,1]-u2*co2
    vco2<- total_co2_flx_2[1,2]-v2*co2
    wco2<- total_co2_flx_2[1,3]-w2*co2
    uh2o<- total_h2o_flx_2[1,1]-u2*h2o
    vh2o<- total_h2o_flx_2[1,2]-v2*h2o
    wh2o<- total_h2o_flx_2[1,3]-w2*h2o
    uch4<- total_ch4_flx_2[1,1]-u2*ch4
    vch4<- total_ch4_flx_2[1,2]-v2*ch4
    wch4<- total_ch4_flx_2[1,3]-w2*ch4
    result<- c(U, V, W, Rxx, Rxy, Rxz, Ryy, Ryz, Rzz, T, co2, h2o, ch4, uT, vT, wT, uco2, vco2, wco2,
        uh2o, vh2o, wh2o, uch4, vch4, wch4, phi, theta)
    names(result)<- c(“U”, “V”, “W”, “Rxx”, “Rxy”, “Rxz”, “Ryy”, “Ryz”, “Rzz”, “T”, “co2”, “h2o”,
        “ch4”, “uT”, “vT”, “wT”, “uco2”, “vco2”, “wco2”, “uh2o”, “vh2o”, “wh2o”, “uch4”, “vch4”,
        “wch4”, “phi”, “theta”)
    return(result)
)
#————————————————————————
#Apply coordinate rotation
data_post_rotate<- NULL
angles<- NULL
for (i in 1:nrow(data))(
    #pointers to variables used in function rotate:
```

```
    Ui<- u_prerotate[i]
    Vi<- v_prerotate[i]
    Wi<- w_prerotate[i]
    Rxxi<- Rxx[i]
    Rxyi<- Rxy[i]
    Rxzi<- Rxz[i]
    Ryyi<- Ryy[i]
    Ryzi<- Ryz[i]
    Rzzi<- Rzz[i]
    Ti<- Ts[i]
    rhoco2i<- rhoco2[i]
    rhovi<- rhov[i]
    dch4i<- dch4[i]
    uTi<- uT[i]
    vTi<- vT[i]
    wTi<- wT[i]
    uco2i<- uco2[i]
    vco2i<- vco2[i]
    wco2i<- wco2[i]
    uh2oi<- uh2o[i]
    vh2oi<- vh2o[i]
    wh2oi<- wh2o[i]
    uch4i<- uch4[i]
    vch4i<- vch4[i]
    wch4i<- wch4[i]
    #apply coordinate rotation
    post_rotate<- rotate(Ui, Vi, Wi, Rxxi, Rxyi, Rxzi, Ryyi, Ryzi, Rzzi, Ti, rhoco2i, rhovi, dch4i, uTi, vTi,
        wTi, uco2i, vco2i, wco2i, uh2oi, vh2oi, wh2oi, uch4i, vch4i, wch4i)
    #returns result as ”post_rotate”
    theta<- post_rotate[27] #angle to do first rotation
    phi<- post_rotate[26] #angle to do second rotation
    #rbind post_rotate to create data file
    data_post_rotate<- rbind(data_post_rotate,post_rotate)
    a<- cbind(theta,phi)
    angles<- rbind(angles,a)
    colnames(angles)<- c(”theta”,”phi”)
)
#Define outputs of rotate function
U<- data_post_rotate[,1] #mean horizontal wind (x-dir)
V<- data_post_rotate[,2] #mean horizontal wind (y-dir)
W<- data_post_rotate[,3] #mean vertical wind (z-dir)
Rxx<- data_post_rotate[,4] #stdev U
Rxy<- data_post_rotate[,5] #covariance U and V
Rxz<- data_post_rotate[,6] #covariance U and W
Ryy<- data_post_rotate[,7] #stdev V
Ryz<- data_post_rotate[,8] #covariance V and W
Rzz<- data_post_rotate[,9] #stdev W
T<- data_post_rotate[,10] #mean temperature from sonic [degrees C]
```

```
rhoco2<- data_post_rotate[,11] #mean co2 density from LI-7500 [kg m^-3]
rhov<- data_post_rotate[,12] #mean h2o density from LI-7500 [kg m^-3]
dch4<- data_post_rotate[,13] #mean ch4 molar density from LI-7700 [mmol m^-3]
uT<- data_post_rotate[,14] #covariance U and T
vT<- data_post_rotate[,15] #covariance V and T
wT<- data_post_rotate[,16] #covariance W and T
uco2<- data_post_rotate[,17] #covariance U and CO2
vco2<- data_post_rotate[,18] #covariance V and CO2
wco2<- data_post_rotate[,19] #covariance W and CO2 [kg m^-2s^-1]
uh2o<- data_post_rotate[,20] #covariance U and H2O
vh2o<- data_post_rotate[,21] #covariance V and H2O
wh2o<- data_post_rotate[,22] #covariance W and H2O [kg m^-2s^-1]
uch4<- data_post_rotate[,23] #covariance U and CH4
vch4<- data_post_rotate[,24] #covariance V and CH4
wch4<- data_post_rotate[,25] #covariance W and CH4 [mmol m^-3s^-1]
theta<- data_post_rotate[,27]*180/pi #angle to do first rotation
phi<- data_post_rotate[,26]*180/pi #angle to do second rotation
#——————————————————————
wT_postrotate<- wT
wh2o_postrotate<- wh2o
wco2_postrotate<- wco2
wch4_postrotate<- wch4
#——————————————————————
#Determine flux multipliers to compute CH4 flux
#Flux Multiplier Tables:
# KAPPA
kappa_file<- read.csv(file="flux_multiplier1.csv",head=FALSE)
kappa_file<- kappa_file[2:67,2:107]
temp<- seq(-50,55)
pressure<- seq(50,115)
colnames(kappa_file)<- temp
rownames(kappa_file)<- pressure
# P derivative
Pder<- read.csv(file="flux_multiplier2.csv",head=FALSE)
Pder<- Pder[2:66,2:102]
temp<- seq(-50,50)
pressure<- seq(50,114)
colnames(Pder)<- temp
rownames(Pder)<- pressure
# T derivative
Tder<- read.csv(file="flux_multiplier3.csv",head=FALSE)
Tder<- Tder[2:67,2:106]
temp<- seq(-50,54)
pressure<- seq(50,115)
colnames(Tder)<- temp
rownames(Tder)<- pressure
kappa_multiplier<- NULL
pder_multiplier<- NULL
```

```
tder_multiplier<- NULL
julian_day<- NULL
for(i in 1:nrow(data))(
    P<- press[i]
    T<- Ts[i]
    sigma<- rhov[i]/rho[i]
    if(is.na(P)==TRUE)(
        kappa<- NA
        pder<- NA
        tder<- NA
        kappa_multiplier<- rbind(kappa_multiplier,kappa)
        pder_multiplier<- rbind(pder_multiplier,pder)
        tder_multiplier<- rbind(tder_multiplier,tder)
        julian_day<- rbind(julian_day,j_day)
        flux_multiplier<- cbind(julian_day,kappa_multiplier,pder_multiplier,tder_multiplier)
        next
    )
    #Compute fast response air temperature from sonic temperature and IRGA vapour density
    H2O_li<- h2omean[i]
    amb_press_li<- press[i]
    q<- rhov[i]/(rho[i]+rhov[i])
    Tc_absolute<- (Ts[i]+273.15)/(1+0.51*q)
    #Compute the molar mixing ratio of CO2 and H2O
    divisor_li<- (amb_press_li/(R*Tc_absolute))-(H2O_li/18)
    Xv_li<- H2O_li/(18*divisor_li)
    # find equivalent pressure (Pe)
    Pe<- amb_press_li*(1+0.46*Xv_li)
    # use Pe and T to find correct flux multipliers from excel files
    # first find upper and lower Pe and T
    #Pe
    x1<- as.integer(Pe)
    x2<- x1+1
    #T
    Tc<- Tc_absolute-273.15
    y1<- as.integer(Tc)
    y2<- y1+1
    #find flux multipliers:
    #kappa
    a1<- which(colnames(kappa_file)==y1)
    a2<- which(colnames(kappa_file)==y2)
    b1<- which(rownames(kappa_file)==x1)
    b2<- which(rownames(kappa_file)==x2)
    k1<- kappa_file[b1,a1]
    k2<- kappa_file[b2,a1]
    k3<- kappa_file[b1,a2]
    k4<- kappa_file[b2,a2]
    #first find kappa at correct T and Pe(k1)
    kappa1<- k1+(((k3-k1)/(y2-y1))*(Tc-y1))
```

```
    #then find kappa at correct T and Pe(k2)
    kappa2<- k2+(((k4-k2)/(y2-y1))*(Tc-y1))
    #finally find kappa at correct T and Pe
    kappa<- kappa1+(((kappa2-kappa1)/(x2-x1))*(Pe-x1))
    #P derivative
    a1<- which(colnames(Pder)==y1)
    a2<- which(colnames(Pder)==y2)
    b1<- which(rownames(Pder)==x1)
    b2<- which(rownames(Pder)==x2)
    P1<- Pder[b1,a1]
    P2<- Pder[b2,a1]
    P3<- Pder[b1,a2]
    P4<- Pder[b2,a2]
    #first find pder at correct T and Pe(P1)
    pder1<- P1+(((P3-P1)/(y2-y1))*(Tc-y1))
    #then find tder at correct T and Pe(P2)
    pder2<- P2+(((P4-P2)/(y2-y1))*(Tc-y1))
    #finally find pder at correct T and Pe
    pder<- pder1+(((pder1-pder2)/(x1-x2))*(Pe-x1))
    #T derivative
    a1<- which(colnames(Tder)==y1)
    a2<- which(colnames(Tder)==y2)
    b1<- which(rownames(Tder)==x1)
    b2<- which(rownames(Tder)==x2)
    T1<- Tder[b1,a1]
    T2<- Tder[b2,a1]
    T3<- Tder[b1,a2]
    T4<- Tder[b2,a2]
    #first find tder at correct T and Pe(P1)
    tder1<- T1+(((T3-T1)/(y2-y1))*(Tc-y1))
    #then find tder at correct T and Pe(P2)
    tder2<- T2+(((T4-T2)/(y2-y1))*(Tc-y1))
    #finally find tder at correct T and Pe
    tder<- tder1+(((tder1-tder2)/(x1-x2))*(Pe-x1))
    #julian day
    j_day<- data[i,1]
    #create new file of flux multipliers for each time period
    kappa_multiplier<- rbind(kappa_multiplier,kappa)
    pder_multiplier<- rbind(pder_multiplier,pder)
    tder_multiplier<- rbind(tder_multiplier,tder)
    julian_day<- rbind(julian_day,j_day)
    flux_multiplier<- cbind(julian_day,kappa_multiplier,pder_multiplier,tder_multiplier)
)
#————————————————————————
# Create output data file
Jday<- data[,1]
results<- as.data.frame((matrix(nrow=nrow(data),ncol=37)))
names(results)<- c(“Julian_day”, “RSSI”, “wh2o_postrotate”, “wh2o_scf”, “Fh2o”, “Fh2o_scf”, “wco2_postrotate”,
```

```
    “wco2_scf”, “Fco2”, “Fco2_scf”, “wch4_postrotate”, “wch4_scf”, “Fch4”, “Fch4_scf”, “Fch4_nospec”,
    “QH”, “QE”, “tau”, “ustar”, “swonust”, “svonust”, “svonubar”, “suonubar”, “L”, “u”, “v”, “w”,
    “h2o”, “co2”, “ch4”, “Tk”, “z0”, “wind_dir”, “co2_ppm”, “ch4_ppm”, “coord_rot_angle1”, “coord_rot_angle2”)
results[,]<- 0
#————————————————————————————————
# Add preliminary data to output file
results$wh2o_postrotate<- wh2o_postrotate
results$wco2_postrotate<- wco2_postrotate
results$wch4_postrotate<- wch4_postrotate
results$u<- U
results$v<- V
results$w<- W
results$h2o<- rhov #kg m^-3
results$co2<- rhoco2 #kg m^-3
results$ch4<- dch4 #mmol m^-3
results$Julian_day<- Jday
#————————————————————————————————
# Apply SCF
SCF_7500<- NULL
SCF_7700<- NULL
for(i in 1:length(U))(
    z<- 8.465
    u<- U[i]
    s_7700<- 0.36 #path separation [m] between centre of sonic path and centre of LI7700 light path
    s_7500<- 0.22 #path separation [m] between centre of sonic path and centre of LI7500 light path
    p_7700<- 0.5 #physical path length [m] of LI7700
    p_7500<- 0.125 #path length [m] of LI7500
    #Cospectra functions
    f1<- seq(0.001,1,0.001)
    f2<- seq(1.001,100,0.001)
    cospectra_function1<- function(f)(
        n<- f*u/z
        y<- (11*f)/((1+(13.3*f))^1.75)
        c<- y/n
        return(c)
    )
    cospectra_function2<- function(f)(
        n<- f*u/z
        y<- (4.4*f)/((1+(3.8*f))^2.4)
        c<- y/n
        return(y)
    )
    i1<- integrate(cospectra_function1,0,1)$val
    i2<- integrate(cospectra_function2,1,Inf)$val
    iCo<- i1+i2
    #LI7500 transfer function
    p<- p_7500
    s<- s_7500
```

```
transfer_function1<- function(f)(
    n<- f*u/z
    fp<- n*p/u
    fs<- n*s/u
    Ts_7500<- exp(-9.9*(fs^1.5))
    Tp_7500<- sqrt((3+(exp(-2*pi*fp))-(4/(2*pi*fp))*(1-(exp(-2*pi*fp))))/(2*pi*fp))
    T_7500<- Ts_7500*Tp_7500
    y<- (11*f)/((1+(13.3*f))^1.75)
    TC_7500<- y*T_7500/n
    return(TC_7500)
)
transfer_function2<- function(f)(
    n<- f*u/z
    fp<- n*p/u
    fs<- n*s/u
    Ts_7500<- exp(-9.9*(fs^1.5))
    Tp_7500<- sqrt((3+(exp(-2*pi*fp))-(4/(2*pi*fp))*(1-(exp(-2*pi*fp))))/(2*pi*fp))
    T_7500<- Ts_7500*Tp_7500
    y<- (4.4*f)/((1+3.8*f)^2.4)
    TC_7500<- y*T_7500/n
    return(TC_7500)
)
i1<- integrate(transfer_function1,0,1)$val
i2<- integrate(transfer_function2,1,Inf)$val
iTCo_7500<- i1+i2
#LI7700 transfer function
p<- p_7700
s<- s_7700
transfer_function1<- function(f)(
    n<- f*u/z
    fp<- n*p/u
    fs<- n*s/u
    Ts_7700<- exp(-9.9*(fs^1.5))
    Tp_7700<- sqrt((3+(exp(-2*pi*fp))-(4/(2*pi*fp))*(1-(exp(-2*pi*fp))))/(2*pi*fp))
    T_7700<- Ts_7700*Tp_7700
    y<- (11*f)/((1+(13.3*f))^1.75)
    TC_7700<- y*T_7700/n
    return(TC_7700)
)
transfer_function2<- function(f)(
    n<- f*u/z
    fp<- n*p/u
    fs<- n*s/u
    Ts_7700<- exp(-9.9*(fs^1.5))
    Tp_7700<- sqrt((3+(exp(-2*pi*fp))-(4/(2*pi*fp))*(1-(exp(-2*pi*fp))))/(2*pi*fp))
    T_7700<- Ts_7700*Tp_7700
    y<- (4.4*f)/((1+3.8*f)^2.4)
    TC_7700<- y*T_7700/n
```

```
        return(TC_7700)
    )
    i1<- integrate(transfer_function1,0,1)$val
    i2<- integrate(transfer_function2,1,Inf)$val
    iTCo_7700<- i1+i2
    #spectral correction factors for LI-7500 and LI-7700
    SCF_7500i<- iCo/iTCo_7500
    SCF_7700i<- iCo/iTCo_7700
    SCF_7500<- rbind(SCF_7500,SCF_7500i)
    SCF_7700<- rbind(SCF_7700,SCF_7700i)
)
wh2o_scf<- wh2o_postrotate*SCF_7500
wco2_scf<- wco2_postrotate*SCF_7500
wch4_scf<- wch4_postrotate*SCF_7700
results$wh2o_scf<- wh2o_scf
results$wco2_scf<- wco2_scf
results$wch4_scf<- wch4_scf
#——————————————————————————
#Compute flux of CO2, H2O, CH4 and apply corrections
for (i in 1:nrow(data_post_rotate))(
    print(i)
    sigma<- rhov[i]/rho[i]
    #initial values
    wh2o<- wh2o_scf[i]
    wco2<- wco2_scf[i]
    wch4<- wch4_scf[i]
    #wh2o<- wh2o_postrotate[i]
    #wco2<- wco2_postrotate[i]
    #wch4<- wch4_postrotate[i]
    wT<- wT_postrotate[i]
    #applying corrections requires iteration
    dwT<- 100.0
    dwh2o<- 100.0
    while(dwT>0.001 — dwh2o>0.001)(
        oldheatflux<- wT
        oldmoisflux<- wh2o
        #Schotanus et al. (1983) eqn. (8) —- correction of flux based on sonic T to true T. The correction
        #is essentially due to the fact that speed of sound depends on humidity as well as temperature,
        #so sonic T' #reflects not only true T' but also rhov' (or q').
        wT<- wT_postrotate[i]-0.51*Tkelvin[i]*wh2o/rho[i] #wh2o/rho is ¡w' rhov'¿/rho = ¡w'q'¿
        #WPL correction to vapour flux
        wh2o<- (1.0+mu*sigma)*(wh2o_scf[i]+rhov[i]/Tkelvin[i]*wT) #kg mˆ-2 sˆ-1
        #Calculate dwT and dwh2o
        dwT<- abs(wT-oldheatflux)/abs(oldheatflux)*100
        dwh2o<- abs(wh2o-oldmoisflux)/abs(oldmoisflux)*100
    )
    #CO2
    wco2<- wco2_scf[i]+(mu*rhoco2[i]/rho[i]*wh2o)+((1+mu*sigma)*rhoco2[i]/Tkelvin[i]*wT)
```

```
#CH4
#use uncorrected methane number density (mmol m^-3)
#compute methane mass density:
mc<- 16.043 #molecular weight of methane [mg mmol^-1]
rho_c<- dch4[i] #measured raw number density of methane [mmol m^-3]
q_cm<- mc*rho_c #measured methane mass density before correction [mg m^-3]
press_mean<- press[i]
H2o_li_mean<- h2omean[i] #g m^-3
q<- rhov[i]/(rho[i]+rhov[i])
Tc_absolute<- (Ts[i]+273.15)/(1+0.51*q)
rho_d_li_mean<- (press_mean/(Tc_absolute*RD))-H2o_li_mean*mu #units=g m^-3
rho_a_li_mean<- (rho_d_li_mean+H2o_li_mean)/1000
#Compute the molar mixing ratio of CO2 and H2O
divisor_li<- (press_mean/(R*Tc_absolute))-(H2o_li_mean/18)
Xv_li<- H2o_li_mean/(18*divisor_li)
#Find flux multipliers A, B, and C
A<- flux_multiplier[i,2]
B<- 1+((1-(1.46*Xv_li))*flux_multiplier[i,3])
C<- 1+((1-Xv_li)*flux_multiplier[i,4])+(Xv_li*(B-1))
#convert uncorrected methane flux (w’rho_c’) to mass density
cov_CH4_Uz<- wch4*mc #units = mg m^-2 s^-1
#calculate flux of methane
F_77_ga<- cov_CH4_Uz
#LI7700 modified Webb et al term for methane
CH4_wpl_LE_li<- mu*q_cm/rho[i]*wh2o
CH4_wpl_H_li<- (1+(mu*sigma))*q_cm/(Tc_absolute)*wT
F_77_wpl<- A*(F_77_ga+B*CH4_wpl_LE_li+C*CH4_wpl_H_li) #mg m^-2 s^-1
#Other calculations
tau<- sqrt((Rxz[i]^2)+(Ryz[i]^2))
ustar<- sqrt(tau)
u<- U[i]
swonust<- sqrt(Rzz[i])/ustar #sigma_w/ustar
svonust<- sqrt(Ryy[i])/ustar #sigma_v/ustar
svonubar<- sqrt(Ryy[i])/u #sigma_v/ubar
suonubar<- sqrt(Rxx[i])/u
virt_kin_htflx<- wT+0.61*Tc_absolute*wh2o/rho[i]
TvirtKelvin<- Tc_absolute*(1.0+0.61*rhov[i]/rho[i])
L<- -1.0*(ustar^3)*TvirtKelvin/(kv*g*virt_kin_htflx)
QH<- rho[i]*CP*wT #units J m^-2 s^-1
QE<- LV*wh2o
tau<- rho[i]*tau
Tk<- Tc_absolute
RSSI<- RSSI_avg[i]
#save results
results$Fch4_nospec[i]<- wch4_nospec
results$RSSI[i]<- RSSI
#results$Fco2[i]<- wco2 #kg m^-2 s^-1
#results$Fh2o[i]<- wh2o #kg m^-2 s^-1
```

```
    #results$Fch4[i]<- F_77_wpl #mg m^-2 s^-1
    results$Fco2_scf[i]<- wco2
    results$Fh2o_scf[i]<- wh2o
    results$Fch4_scf[i]<- F_77_wpl
    results$tau[i]<- tau #kg m^2 s^-2
    results$ustar[i]<- ustar #m s^-1
    results$swonust[i]<- swonust
    results$svonust[i]<- svonust
    results$svonubar[i]<- svonubar
    results$suonubar[i]<- suonubar
    results$L[i]<- L #m
    results$QH[i]<- QH #J m^-2 s^-1
    results$QE[i]<- QE #J m^-2 s^-1
    results$Tk[i]<- Tk #K
)
#End of Program
#——————————————————————
```

Appendix B

Eddy Covariance Post-Processing Corrections

B.1 Coordinate Rotation

A coordinate rotation was applied to correct for sonic anemometer tilt, as described in Wilczak et al. (2001). In the field, the sonic anemometer cannot be perfectly leveled so as to ensure that the vertical axis is always perpendicular to the mean wind streamline. Instead, the vertical wind speed signal will likely be contaminated by the other two wind components. To place the sonic anemometer in the streamline coordinate system, a series of two rotations is applied at the end of each averaging interval. The first rotation sets $\overline{v} = 0$ by swinging the x- and y-axes about the z-axis, resulting in new velocities given by:

$$u_1 = u_m \cos\theta + v_m \sin\theta \tag{B.1}$$

$$v_1 = -u_m \sin\theta + v_m \cos\theta \tag{B.2}$$

$$w_1 = w_m \tag{B.3}$$

where the subscript "m" denotes the measured velocities and the rotation angle θ is given by:

$$\theta = \tan^{-1}\left(\frac{\overline{v}_m}{\overline{u}_m}\right). \tag{B.4}$$

The second rotation sets $\overline{w} = 0$ by swinging the new x- and z-axes about the y-axis so that the x-axis points in the mean streamline direction and the final velocities are given by:

$$u_2 = u_1 \cos\phi + w_1 \sin\phi \tag{B.5}$$

$$v_2 = v_1 \tag{B.6}$$

$$w_2 = -u_1 \sin\phi + w_1 \cos\phi \tag{B.7}$$

where the rotation angle ϕ is given by:

$$\phi = \tan^{-1}\left(\frac{\overline{w}_1}{\overline{u}_1}\right). \tag{B.8}$$

B.2 Frequency Response Corrections

Many, if not all, eddy covariance systems underestimate the true atmospheric fluxes due to physical limitations of the sensors, sensor performance, and the frequency response of the eddy covariance system. To compensate for the flux losses at different frequencies of turbulent transport, frequency response corrections are applied to the measured fluxes (Moore, 1986). Application of this correction requires knowledge of both the "true" and attenuated cospectra. The "true" cospectra at this site could not be measured, so an assumption must be made regarding the cospectral shape. The $w'\theta'$ cospectrum model provided by Kaimal et al. (1972) using data obtained in the 1968 Kansas experiments under neutral conditions was chosen to represent the "true" cospectral shape:

$$\frac{-nC_{w\theta}(n)}{u_* T_*} = \begin{cases} \frac{11 f_i}{(1+13.3 f_i)^{1.75}} & f_i \leq 1.0 \\ \frac{4.4 f_i}{(1+3.8 f_i)^{2.4}} & f_i \geq 1.0 \end{cases} \tag{B.9}$$

where $C_{w\theta}$ is the cospectrum for sensible heat, n represents frequency (Hz), and f_i is the normalized frequency given by $f_i = nz/\overline{u}$, with z being the height above the surface and $\overline{u}$ the mean wind speed.

The attenuated cospectral curve is located below the ideal cospectral curve, especially at high frequencies, indicating flux losses related to deficiencies in the frequency response when measuring the covariance between w' and gas fluctuations (Burba and Anderson, 2010). Functions that describe how these deficiencies affect the ideal cospectrum and lower the cospectral curve at each frequency are known as transfer functions. In the application of this correction, only the transfer functions related to gas sensor path averaging and anemometer-gas sensor separation were applied, as they were deemed to have the most significant influence on the flux loss. The influence of scalar path averaging was compensated using the following transfer function (Moore, 1986):

$$T_p = \sqrt{\frac{1}{2\pi f_p}\left(3 + e^{-2\pi f_p} - \frac{4\left(1 - e^{-2\pi f_p}\right)}{2\pi f_p}\right)} \tag{B.10}$$

where f_p is the normalized frequency given by $f_p = np/\overline{u}$, with p representing the sensor path length. The transfer function representing sensor separation is given by (Moore, 1986):

$$T_s = e^{-9.9 f_s^{1.5}} \tag{B.11}$$

where f_s is the normalized frequency given by $f_s = ns/\overline{u}$, with s representing the separation distance between the anemometer and the gas sensor. This transfer function is used to compensate for the separation between scalar sensors (e.g., LI-7700, LI-7500A) and the sonic anemometer that is necessary in order to avoid flow distortion errors in the velocity measurements. The total transfer function is a product of the individual transfer functions. The "true" cospectrum and total transfer function are multiplied together to obtain the attenuated cospectral shape. The flux correction factor (CF) is calculated as the ratio of the integrated "true" model cospectrum to the integrated attenuated cospectrum (Ferrara et al., 2012):

$$CF = \frac{\int\limits_0^\infty C_{w\beta}(f)df}{\int\limits_0^\infty T(f)C_{w\beta}(f)df} \tag{B.12}$$

where $T(f) = \prod_{i=1}^{N} T_i(f)$ is the product of all the appropriate transfer functions (in this case, gas sensor path length (T_p) and anemometer-gas sensor separation (T_s)). The "true" flux ($\overline{w'\beta'}$) is then calculated by multiplying the measured flux $(\overline{w'\beta'})_m$ by the correction factor:

$$(\overline{w'\beta'}) = CF(\overline{w'\beta'})_m. \tag{B.13}$$

B.3 WPL Term and Schotanus Correction

Measured fluctuations in gas concentration can result from fluctuations in water vapour density and temperature, which are not associated with the net transport of the gas of interest. The impact of such fluctuations on flux measurements was derived by Webb et al. (1980) for both the flux of gases, such as CH_4 (QCH_4), and evaporation (E):

$$QCH_4 = \overline{w'\rho_c'} + \mu\frac{\overline{\rho_c}}{\overline{\rho_d}}\overline{w'\rho_v'} + (1+\mu\sigma)\frac{\overline{\rho_c}}{\overline{T}}\overline{w'T'} \tag{B.14}$$

$$E = (1+\mu\sigma)\left(\overline{w'\rho_v'} + \frac{\overline{\rho_v}}{\overline{T}}\overline{w'T'}\right) \tag{B.15}$$

where $\overline{w'\rho_c'}$ is the uncorrected methane flux; $\overline{w'\rho_v'}$ is the water vapour flux; $\overline{w'T'}$ is the heat flux; μ is the ratio of dry air formula weight to water vapour molecular weight ($\mu = 1.6077$); σ is the ratio of water vapour mass density to dry air mass density; $\overline{\rho_c}$ is the average gas density; $\overline{\rho_d}$ is the average mass density of dry air; $\overline{\rho_v}$ is the average water vapour density; and $\overline{T}$ is the average temperature.

The temperature used in these calculations is the sonic-derived temperature. The sonic anemometer provides an estimate of temperature from the measurement of the speed of sound. However, this speed depends on both temperature and humidity, so the following relation is used to calculate the actual air temperature from the sonic temperature, according to Schotanus et al. (1983):

$$\overline{T} = \frac{\overline{T_s}}{1+0.51q} \tag{B.16}$$

where $\overline{T_s}$ is the average sonic-derived temperature and q is the specific humidity. To correct the covariance of temperature with vertical velocity, the following relation from Schotanus et al. (1983) is used:

$$\overline{w'T'} = \overline{w'T_s'} - 0.51\overline{T_s}\,\overline{w'q'}. \tag{B.17}$$

The WPL correction and Schotanus correction are implemented through the use of an iteration, as they are coupled.

B.4 LI-7700 Specific Corrections

It is necessary to adjust the spectroscopic light absorption measurements made by the LI-7700 methane analyzer for the spectroscopic effects of pressure, temperature, and water vapour density. These effects can be compensated for by applying multipliers to each of the terms in the WPL formulation of CH_4 flux (LI-COR, Inc., 2010):

$$QCH_4 = A\left[\overline{w'\rho_c'} + B\mu\frac{\overline{\rho_c}}{\overline{\rho_d}}\overline{w'\rho_v'} + C(1+\mu\sigma)\frac{\overline{\rho_c}}{\overline{T}}\overline{w'T'}\right]. \tag{B.18}$$

This equation is in a form similar to that of Webb et al. (1980) except it includes the multipliers for the spectroscopic corrections, A, B, and C, that are specific to the LI-7700 analyzer and are given by (LI-COR, Inc., 2010):

$$A = \overline{\kappa} \tag{B.19}$$

$$B = 1 + (1 - 1.46\overline{x_v})\alpha_v\overline{P_e}\frac{\kappa_{P_e}}{\overline{\kappa}} \tag{B.20}$$

$$C = 1 + (1 - \overline{x_v})\overline{T}\frac{\kappa_T}{\overline{\kappa}} + \overline{x_v}(B - 1). \tag{B.21}$$

These multipliers account for the spectroscopic effects of temperature, pressure, and water vapour on methane molar density (A), spectroscopic effects of pressure and water vapour on latent heat flux (B), and spectroscopic effects of temperature, pressure, and water vapour on sensible heat flux (C). These multipliers must be recalculated for each averaging period.

The spectroscopic effects of water vapour are taken into account using the concept of equivalent pressure (P_e). The equivalent pressure accounts for the fact that different gas species cause pressure broadening to different degrees. For environmental measurements, water vapour is the only variable gas present in sufficient quantities to affect pressure broadening, so P_e is defined relative to dry air (LI-COR, Inc., 2010):

$$P_e = P(1 + \alpha_v x_v) \tag{B.22}$$

where $\alpha_v = a_v - 1$ and a_v is the foreign gas broadening coefficient for water vapour relative to dry air ($a_v = 1.46$), x_v is the mole fraction of water vapour, and $\overline{P}$ is the average pressure.

To acquire the values for $\overline{\kappa}$ (which corrects for spectroscopic effects of T, P, x_v), $\alpha_v \overline{P_e} \frac{\kappa_{P_e}}{\kappa}$ (where κ_{P_e} is the rate of change of κ with P_e at constant $\overline{T}$), and $\overline{T} \frac{\kappa_T}{\kappa}$ (where κ_T is the rate of change of κ with T at constant $\overline{P_e}$), high resolution digital tables provided by LI-COR were used. These tables covered temperatures of -50 to 55°C and pressures of 50 to 115 kPa in 1°C and 1 kPa increments. Linear interpolation was used between temperature and equivalent pressure values to acquire a more accurate estimate of the spectroscopic correction factors.

Appendix C

Flux Footprint Calculation

C.1 Schmid (1994) 50% Source Area

For stable stratification, the equation for determining the dimensions of the source area is:

$$D_N = \alpha_1 \left(\frac{z_m}{z_0}\right)^{\alpha_2} \exp\left[\alpha_3 \left(\frac{z_m}{L}\right)^{\alpha_4}\right] \left(\frac{\sigma_v}{u_*}\right)^{\alpha_5} \tag{C.1}$$

where D_N is the dimension of the bounding contour, normalized by the roughness length (z_0), z_m is the measurement height, L is the Obukhov length, σ_v is the standard deviation of the lateral wind fluctuations, u_* is the friction velocity, and the parameter values (α_{1-5}) are provided for each normalized dimension in Table C.1. The dimensions of the bounding contour consist of (a) the distance to the downwind edge, (e) distance to the upwind edge, (d) the maximum width, (x_d) the distance to the point where the contour is widest, (x_m) the distance to the maximum source location, and (A_r) the area bounded by the contour.

For unstable stratification, the equation for determining the dimensions of the source area is:

$$D_N = \alpha_1 \left(\frac{z_m}{z_0}\right)^{\alpha_2} \left(1 - \alpha_3 \frac{z_m}{L}\right)^{\alpha_4} \left(\frac{\sigma_v}{u_*}\right)^{\alpha_5}. \tag{C.2}$$

The parameter values for each normalized dimension are provided in Table C.2.

Table C.1: Parameter values for each normalized dimension under stable stratification Schmid (1994).

Dimension	α_1	α_2	α_3	α_4	α_5
a/z_0	3.28	1.09	3.53	1.05	0
e/z_0	10.1	1.08	3.84	1.07	0
d/z_0	4.07	0.79	2.97	0.977	1
x_d/z_0	4.84	1.13	3.83	1.10	0
x_m/z_0	1.58	1.25	2.91	1.02	0
A_r/z_0^2	51.3	1.86	7.29	1.05	1

Table C.2: Parameter values for each normalized dimension under unstable stratification Schmid (1994)

Dimension	α_1	α_2	α_3	α_4	α_5
a/z_0	2.79	1.11	14.1	−0.399	0
e/z_0	8.54	1.11	12.8	−0.390	0
d/z_0	3.25	0.832	28.2	−0.272	1
x_d/z_0	4.29	1.15	10.3	−0.408	0
x_m/z_0	1.72	1.24	8.65	−0.746	0
A_r/z_0^2	31.4	1.93	17.8	−0.642	1

C.2 Hsieh et al. (2000) 90% Flux Fetch

The 90% flux fetch (x) is the upwind extent of the source area that contributes 90% of the measured flux (Q). Hsieh et al. (2000) determined the fetch as a function of the measurement height (z_m), the roughness length (z_0), and the atmospheric stability parameter (z_m/L):

$$\frac{x}{|L|} = \frac{-1}{k_v^2 \ln\left(\frac{Q}{S_0}\right)} D \left(\frac{z_u}{L}\right)^P \tag{C.3}$$

where S_0 is the surface flux and $\frac{Q}{S_0} = 0.90$. The length scale z_u is defined as

$$z_u = z_m \left(\ln\left(\frac{z_m}{z_0}\right) - 1 + \frac{z_0}{z_m}\right) \tag{C.4}$$

and D and P are similarity constants defined at different stabilities:

$D = 0.28$; $P = 0.59$	unstable
$D = 0.97$; $P = 1$	near neutral and neutral conditions
$D = 2.44$; $P = 1.33$	stable.

Appendix D

Roughness Length Calculation

For each record, the wind profile law is solved by employing an iteration to find the best fit roughness length (z_0) over a search range from 0.0001 m to 0.1 m in steps of 0.0001 m and minimizing the residual, defined as the square of the difference between the observed wind speed and the calculated wind speed. The values for u_* and L used in this calculation are provided directly by the sonic anemometer. For stable conditions (positive L), the following wind profile is used:

$$\overline{u}(z) = \frac{u_*}{k_v}\left[\ln\frac{z}{z_0} + 5\frac{z - z_0}{L}\right]. \tag{D.1}$$

For unstable conditions (negative L):

$$\overline{u}(z) = \frac{u_*}{k_v}\left[\ln\frac{z}{z_0} - \psi_m\left(\frac{z}{L}\right) + \psi_m\left(\frac{z_0}{L}\right)\right] \tag{D.2}$$

where ψ_m is given in terms of φ_m as

$$\psi_m = 2\ln\left(\frac{1+\varphi_m^{-1}}{2}\right) + \ln\left(\frac{1+\varphi_m^{-2}}{2}\right) + 2\arctan\left(\varphi_m^{-1}\right) + \frac{\pi}{2}. \tag{D.3}$$

The similarity function (φ_m) recommended by Dyer and Bradley (1982) is used:

$$\varphi_m = \left(1 - 28\frac{z}{L}\right)^{-1/4}. \tag{D.4}$$

Appendix E

Micrometeorological Data at Oil Sands Tailings Pond Field Site

Table E.1: Half-hour means of micrometeorological data collected during the oil sands tailings pond field campaign from 11 July to 16 July 2012, including sonic temperature ($\overline{T_s}$), horizontal wind velocity post-rotation ($\overline{u}$), wind direction (in degrees from North), friction velocity (u_*), Obukhov length (L), sensible heat flux (Q_H), and latent heat flux (Q_E).

Julian Day	$\overline{T_s}$ [K]	$\overline{u}$ [m s^{-1}]	Wind Direction	u_* [m s^{-1}]	L [m]	$\frac{\sigma_w}{u_*}$	Q_H [W m^{-2}]	Q_E [W m^{-2}]
193.417	295.14	1.307	209.4	0.180	-11.10	1.459	38.81	95.07
193.438	295.81	1.804	171.7	0.223	-19.21	1.242	41.99	109.04
193.458	296.25	3.178	133.4	0.310	-44.81	1.224	43.88	186.93
193.479	296.62	3.243	128.9	0.273	-26.58	1.414	49.28	228.45
193.500	297.10	2.293	137.7	0.289	-29.48	1.228	54.79	217.43
193.521	297.33	1.890	118.0	0.287	-25.75	1.185	64.92	199.28
193.542	297.72	1.237	206.0	0.208	-16.76	1.387	36.44	138.07
193.563	298.08	0.411	242.2	0.288	-101.18	1.275	11.18	123.63
193.583	298.33	0.970	150.1	0.248	-24.80	1.380	45.06	108.71
193.604	298.72	1.446	160.4	0.174	-11.52	1.777	28.66	146.74
193.625	299.57	2.863	147.4	0.220	-14.80	1.570	49.79	162.96
193.646	299.72	3.132	147.5	0.195	-19.47	1.425	24.16	115.01
193.667	300.20	2.515	155.9	0.225	-19.33	1.466	38.71	165.78
193.688	300.66	3.019	153.3	0.270	-36.56	1.212	33.55	170.28
193.708	301.23	2.944	163.0	0.281	-34.58	1.113	39.52	211.58
193.729	301.67	3.288	162.6	0.278	-35.73	1.170	39.25	169.09
193.750	302.07	3.702	173.1	0.136	-4.55	2.081	39.75	107.20
193.771	302.40	3.499	190.5	0.115	-3.39	2.532	24.18	195.62
193.792	302.65	3.302	194.1	0.145	-9.24	1.768	11.54	223.98
193.813	302.97	3.527	145.5	0.287	-91.33	1.197	5.68	219.10
193.833	303.13	3.394	104.3	0.250	-61.11	1.107	13.32	115.36
193.854	302.72	4.375	82.7	0.192	-38.39	1.847	8.27	99.34
193.875	302.08	5.234	84.0	0.219	-73.79	1.708	1.97	135.91

193.896	301.53	4.397	96.4	0.205	-71.71	1.259	1.02	124.42
193.917	300.71	4.438	104.6	0.214	-72.62	1.262	2.86	116.84
193.938	300.02	3.958	111.5	0.263	-155.33	1.122	-8.66	250.73
193.958	299.05	3.892	110.8	0.263	-50.59	1.147	15.14	210.67
193.979	297.98	3.744	101.7	0.221	-61.50	1.211	6.36	117.55
194.000	297.46	3.363	258.3	0.207	-48.75	1.334	5.51	137.27
194.021	296.20	4.147	254.1	0.250	-32.15	1.145	29.50	171.40
194.042	295.08	3.252	230.4	0.116	-7.08	1.743	11.41	103.49
194.063	294.08	3.986	226.5	0.083	-3.26	2.249	9.90	71.86
194.083	293.73	2.934	225.3	0.147	88.48	1.135	-4.96	25.08
194.104	294.15	0.675	206.8	0.133	-24.73	0.862	4.22	55.12
194.125	294.33	1.908	85.2	0.114	43.83	1.736	-8.94	81.72
194.146	293.43	1.373	79.2	0.059	-4.58	2.710	2.77	15.03
194.167	293.31	1.206	229.9	0.097	-11.83	1.105	5.44	16.49
194.188	291.84	1.485	200.1	0.129	-17.93	0.729	10.18	1.97
194.208	291.36	2.005	217.5	0.092	82.51	1.191	-1.18	5.02
194.229	290.71	1.540	230.7	0.064	-7.80	2.101	1.87	14.48
194.250	289.83	1.847	219.5	0.051	-1.77	2.776	4.66	22.97
194.271	289.79	1.228	236.8	0.093	-2.74	1.883	21.16	56.10
194.292	290.51	1.227	122.4	0.103	-2.71	2.315	28.78	85.70
194.313	290.47	1.466	165.9	0.073	-1.00	2.839	31.39	29.98
194.333	290.31	1.437	194.4	0.039	-0.15	5.299	32.67	11.86
194.354	290.74	1.111	196.1	0.130	-2.89	2.202	62.32	52.47
194.375	290.94	1.818	119.0	0.153	-3.49	1.979	90.31	-19.47
194.396	290.93	2.481	95.7	0.156	-3.67	1.849	84.62	73.68
194.438	293.10	1.235	82.7	0.155	-2.75	2.291	112.34	54.49
194.500	295.48	2.122	120.3	0.371	-41.69	0.889	105.10	9.21
194.521	296.23	1.795	188.5	0.278	-11.49	1.310	158.78	40.73
194.542	297.28	2.003	184.0	0.168	-5.32	1.769	74.86	33.52
194.563	297.95	2.658	156.8	0.129	-0.98	2.859	178.32	129.37
194.583	298.97	3.350	164.5	0.218	-4.69	1.786	180.44	126.67
194.646	301.01	4.670	132.5	0.368	-33.19	1.151	121.77	108.94
194.667	301.73	9.232	93.4	0.463	-77.82	1.243	60.50	652.86
194.688	301.77	8.733	82.9	0.406	-62.11	1.414	50.22	568.83
194.708	301.36	10.040	249.6	0.475	-140.11	1.285	24.00	556.57
194.729	301.13	9.260	253.6	0.363	-74.06	1.667	13.13	566.43
194.750	300.76	8.191	254.9	0.346	-59.21	1.567	22.52	505.45
194.771	300.64	7.974	245.1	0.427	-88.69	1.265	47.49	376.02
194.792	299.82	9.389	228.4	0.402	-80.93	1.394	44.56	329.06
194.813	298.52	9.349	216.3	0.526	-127.30	1.192	87.81	152.18
194.833	297.03	7.490	196.3	0.372	-195.99	1.455	13.04	131.10
194.854	295.72	6.859	195.9	0.394	-127.12	1.337	27.92	185.38
194.875	294.63	5.328	186.1	0.275	-81.08	1.469	16.90	73.80
194.896	293.76	3.631	168.7	0.324	-143.93	1.080	16.46	55.44
194.917	292.76	3.869	160.0	0.388	1087.32	1.005	-6.93	31.02
194.938	292.33	2.664	162.9	0.269	3669.47	1.017	-3.09	35.93
194.958	291.80	1.950	173.6	0.135	-23.51	1.349	7.32	23.72
194.979	291.34	1.974	185.6	0.145	-47.36	1.260	3.63	27.61
195.000	291.09	1.979	191.0	0.132	-18.91	1.290	7.54	42.13
195.021	290.62	2.127	198.7	0.131	-15.12	1.394	8.60	58.59
195.042	290.35	2.529	208.4	0.179	-19.52	1.312	18.65	94.32
195.063	289.93	3.046	217.5	0.163	-11.41	1.408	25.10	109.21
195.083	289.37	3.195	231.6	0.166	-18.54	1.428	8.75	176.11
195.104	288.19	3.220	84.4	0.237	-14.58	1.177	67.50	169.37
195.125	287.58	3.217	258.1	0.237	-15.04	1.240	66.51	145.88
195.146	287.55	2.484	79.3	0.231	-16.78	1.315	51.85	169.84
195.167	286.81	1.827	252.6	0.127	-3.44	2.352	43.18	119.78
195.188	286.48	3.032	80.7	0.157	-4.61	1.867	60.69	166.88
195.208	286.46	4.327	86.8	0.245	-17.33	1.257	58.17	216.28
195.229	285.61	4.851	87.9	0.187	-6.86	1.616	68.27	207.31

195.250	285.34	4.518	256.6	0.262	-20.10	1.250	61.59	231.74
195.271	285.63	5.056	79.5	0.281	-31.75	1.216	43.52	248.07
195.292	285.33	4.623	253.7	0.311	-27.02	1.144	79.42	244.50
195.313	285.07	4.310	247.6	0.187	-6.84	1.721	70.68	175.64
195.333	285.56	3.810	235.9	0.195	-9.01	1.536	60.68	151.17
195.354	286.52	2.661	252.0	0.168	-4.95	1.850	71.07	169.71
195.375	287.53	2.561	255.3	0.206	-9.22	1.496	70.20	170.83
195.396	288.40	2.435	252.7	0.145	-3.00	2.089	76.81	170.45
195.417	289.90	2.745	88.5	0.187	-5.56	1.681	90.40	176.78
195.438	291.32	3.154	83.5	0.169	-5.35	1.701	64.48	191.11
195.458	292.52	2.174	250.2	0.122	-3.10	2.451	38.63	176.14
195.479	293.51	3.668	224.5	0.285	-22.38	1.310	73.18	230.95
195.500	293.77	5.127	236.0	0.292	-38.66	1.197	44.56	158.42
195.521	294.05	4.347	242.9	0.110	-1.70	3.168	54.35	201.98
195.542	294.56	4.002	241.7	0.219	-13.51	1.680	51.78	215.49
195.563	295.08	3.697	233.1	0.254	-20.23	1.368	55.66	206.66
195.583	295.57	3.503	246.1	0.275	-17.56	1.421	83.29	263.24
195.604	295.93	3.558	257.9	0.284	-23.85	1.310	66.04	235.38
195.625	296.18	2.874	234.7	0.350	-58.42	0.969	49.60	192.18
195.646	296.41	1.304	98.3	0.400	-80.00	0.923	57.32	168.06
195.667	296.91	1.261	205.9	0.315	-37.53	1.034	62.35	139.02
195.688	297.27	2.401	192.7	0.274	-35.79	1.105	42.77	97.15
195.708	297.50	2.836	215.2	0.301	-61.55	1.008	27.96	145.56
195.729	297.55	4.069	226.7	0.231	-29.49	1.313	25.66	144.21
195.750	297.77	3.384	222.6	0.223	-36.04	1.245	17.88	118.55
195.771	297.85	2.599	216.5	0.330	-188.23	0.686	10.46	83.08
195.792	297.83	1.247	217.7	0.144	-9.35	1.788	21.45	82.39
195.813	297.91	1.613	229.4	0.123	-6.88	1.664	15.93	98.69
195.833	297.91	1.052	217.1	0.093	-4.40	1.830	9.84	84.58
195.854	297.90	0.304	137.7	0.165	-24.32	1.210	11.08	67.66
195.875	297.76	1.834	173.5	0.219	-46.53	0.725	15.97	49.91
195.896	297.11	2.901	184.8	0.073	13.77	1.061	-5.17	36.17
195.917	296.28	2.669	203.4	0.057	15.60	1.012	-1.68	8.70
195.938	296.07	2.849	205.1	0.037	4.51	1.346	-1.05	1.35
195.958	294.97	3.643	198.5	0.107	90.13	0.994	-2.87	23.05
195.979	294.26	3.597	191.6	0.105	14.87	1.300	-10.32	48.03
196.000	293.76	3.763	198.1	0.068	122.68	1.762	-0.81	8.04
196.021	292.99	3.859	196.3	0.157	7701.18	0.974	-2.03	27.06
196.042	292.13	3.923	179.8	0.105	-102.06	1.376	-3.00	54.54
196.063	292.17	4.218	174.0	0.126	-37.08	1.316	0.37	58.58
196.083	291.56	4.105	178.9	0.152	-27.70	1.390	4.62	87.25
196.104	290.93	5.423	176.5	0.153	-337.59	1.505	-3.97	67.21
196.125	291.15	5.167	160.0	0.167	-10.92	1.755	30.73	89.77
196.146	290.98	4.386	156.9	0.173	-29.12	1.577	12.65	38.08
196.167	290.49	3.786	152.8	0.241	-44.03	1.145	26.28	19.17
196.188	290.67	4.285	155.4	0.168	-50.74	1.464	6.05	28.94
196.208	289.94	4.466	155.4	0.161	95.16	1.471	-5.79	27.66
196.229	289.54	4.989	162.6	0.170	-24.82	1.630	12.31	69.80
196.250	289.16	4.367	154.6	0.139	-13.04	1.847	15.52	32.85
196.271	288.60	5.293	158.1	0.212	-33.84	1.322	19.71	64.22
196.292	288.46	6.073	158.8	0.216	-24.73	1.434	29.59	78.37
196.313	288.31	4.988	162.7	0.203	-21.58	1.399	28.08	77.62
196.333	288.59	5.424	157.5	0.194	-9.68	1.539	59.22	88.77
196.354	289.29	5.277	160.6	0.201	-11.08	1.494	57.01	94.20
196.375	290.28	4.437	155.4	0.185	-4.59	1.737	113.80	73.70
196.396	291.50	4.670	157.2	0.193	-4.93	1.746	120.15	93.86
196.417	292.38	5.124	146.3	0.196	-5.19	1.689	121.89	71.59
196.438	293.40	4.654	148.9	0.194	-3.78	1.849	159.83	105.21
196.458	294.39	4.086	151.2	0.144	-1.62	2.515	155.72	83.46
196.479	295.93	3.825	147.9	0.218	-3.60	2.001	241.94	95.97

196.500	297.08	3.541	145.2	0.163	-1.56	2.525	232.68	91.19
196.521	298.20	3.464	142.5	0.144	-1.13	2.987	216.91	133.11
196.542	299.25	4.211	141.3	0.175	-1.83	2.346	242.67	176.50
196.563	299.80	5.172	149.9	0.288	-11.10	1.295	168.35	251.46
196.583	300.18	5.174	148.8	0.421	-27.29	0.991	224.84	174.10
196.604	300.57	4.337	149.1	0.263	-6.46	1.568	233.79	143.28
196.625	300.87	4.602	160.2	0.259	-7.06	1.491	198.47	199.62
196.646	301.17	4.372	152.2	0.230	-4.61	1.738	216.59	183.04
196.667	301.57	3.264	160.1	0.309	-10.60	1.360	233.72	117.52
196.688	301.72	2.771	159.4	0.266	-8.27	1.498	191.86	70.34
196.708	302.01	2.370	164.2	0.329	-16.43	1.258	179.40	104.58
196.729	302.10	1.674	162.2	0.167	-2.63	2.366	149.03	55.54
196.750	302.05	0.870	94.7	0.040	-0.04	8.292	123.34	96.96
196.771	302.19	1.522	122.2	0.181	-5.35	1.886	90.85	62.60
196.792	302.28	2.612	145.6	0.107	-1.14	2.908	85.11	99.71
196.813	302.30	2.649	159.8	0.185	-8.33	1.497	59.98	76.20
196.833	301.99	2.853	154.2	0.088	-6.78	1.712	4.29	58.17
196.854	301.74	2.089	146.8	0.057	-73.38	1.448	-3.79	53.06
196.875	301.60	0.264	85.3	0.101	434.58	0.509	-0.36	2.08
196.896	301.46	1.228	104.2	0.090	-18.05	0.514	3.11	4.81
196.917	299.56	3.062	137.4	0.320	-168.29	1.147	19.97	-41.64
196.938	297.72	4.211	131.2	0.334	253.16	1.211	-15.79	40.95
196.958	297.10	3.910	135.0	0.322	255.90	1.200	-13.55	30.42
196.979	296.31	3.047	117.9	0.204	-407.45	1.145	0.08	23.27
197.000	295.65	4.281	127.7	0.202	161.90	1.460	-5.58	15.77
197.021	295.08	3.911	138.6	0.303	1254.94	1.295	-3.26	18.17
197.042	294.40	3.017	141.1	0.287	402.84	1.204	-7.06	26.97
197.063	293.56	3.249	131.7	0.194	83.92	1.248	-8.43	12.35
197.083	293.02	3.502	130.0	0.168	178.81	1.361	-2.29	-0.44
197.104	292.64	3.610	128.1	0.179	345.22	1.412	-2.18	10.02
197.125	292.26	3.816	126.6	0.206	-188.54	1.351	3.26	10.52
197.146	291.85	3.885	125.7	0.198	-259.69	1.379	1.85	10.08
197.167	291.59	4.259	128.0	0.220	-407.17	1.249	1.43	11.68
197.188	291.40	4.104	126.9	0.260	-333.29	1.159	3.61	12.97
197.208	291.09	3.814	127.4	0.208	-140.10	1.471	4.81	10.61
197.229	290.84	4.062	130.8	0.287	-224.87	1.323	7.75	18.46
197.250	290.46	5.274	129.3	0.317	-563.66	1.266	3.78	15.30
197.271	290.18	5.132	129.0	0.315	-178.19	1.274	14.02	17.15
197.292	289.96	5.126	136.5	0.358	-209.59	1.299	18.05	12.91
197.313	289.75	5.886	135.7	0.416	-183.88	1.185	32.56	19.39
197.333	289.54	5.460	135.3	0.355	-138.56	1.237	27.10	13.87
197.354	289.43	5.844	135.7	0.377	-118.63	1.234	38.05	18.34
197.375	289.72	4.661	140.1	0.392	-90.30	1.134	55.42	38.02
197.396	289.90	4.531	141.2	0.420	-117.52	1.151	53.16	24.04
197.417	289.93	4.665	137.0	0.377	-79.71	1.185	56.20	29.48
197.438	289.98	4.773	142.6	0.468	-98.28	1.188	87.43	42.35
197.458	289.98	4.874	144.4	0.492	-111.88	1.118	90.02	39.16
197.479	290.36	4.998	139.4	0.404	-62.70	1.191	88.14	42.99
197.500	290.70	5.610	140.7	0.513	-132.59	1.148	85.59	41.46
197.521	291.09	5.375	141.3	0.524	-163.78	1.149	73.74	34.61
197.542	291.65	5.365	140.8	0.497	-160.84	1.203	64.10	29.54
197.563	292.06	5.750	138.9	0.503	-173.51	1.196	61.16	36.84
197.583	292.70	5.740	140.4	0.554	-177.59	1.123	79.92	43.06
197.604	293.37	5.700	139.0	0.474	-118.74	1.246	76.01	27.38
197.625	293.97	4.799	147.3	0.599	-143.35	1.028	125.93	59.99
197.646	293.94	4.342	152.0	0.501	-105.71	1.041	100.41	42.76
197.667	294.12	4.813	144.8	0.545	-128.77	1.094	106.23	42.62
197.688	294.28	5.556	138.7	0.486	-133.47	1.183	72.79	24.39
197.708	294.57	4.206	148.2	0.521	-143.04	1.087	83.16	41.33
197.729	294.80	3.939	148.3	0.478	-145.20	1.073	63.58	27.16

197.750	294.93	3.451	150.4	0.447	-136.12	1.067	53.83	43.86
197.771	295.06	3.437	148.9	0.447	-171.44	1.093	43.04	31.83
197.792	295.27	3.398	153.3	0.386	-195.25	1.036	23.86	24.25
197.813	295.17	3.287	161.6	0.358	-246.19	1.012	13.75	33.37
197.833	294.75	4.241	156.2	0.419	-373.03	1.001	15.04	29.19
197.854	294.40	3.490	161.1	0.387	-769.05	0.983	4.90	22.71
197.875	294.07	3.361	160.5	0.399	-675.30	0.967	5.82	32.03
197.896	293.63	2.479	161.7	0.295	-300.46	1.076	5.08	31.88
197.917	293.26	2.597	153.7	0.285	-769.49	1.124	1.19	19.67
197.938	292.86	2.831	153.5	0.327	514.42	1.136	-6.53	8.61
197.958	292.63	2.930	143.6	0.384	1797.22	1.177	-3.87	15.33
197.979	292.34	3.204	143.1	0.358	-1738.76	1.274	0.60	23.14
198.000	291.88	3.285	154.9	0.342	-618.99	1.006	2.74	39.74
198.021	291.43	2.709	153.3	0.314	270.97	0.898	-11.03	15.56
198.042	291.40	1.995	144.1	0.193	162.13	1.213	-4.39	7.59
198.063	291.26	1.779	152.3	0.176	66.83	1.050	-7.55	6.25
198.083	290.73	1.705	164.4	0.129	47.40	1.094	-4.54	7.69
198.104	290.60	2.058	149.0	0.167	-155.37	1.102	1.60	14.06
198.125	290.02	1.345	169.7	0.095	-50.68	1.522	0.79	9.28
198.146	289.72	1.398	160.2	0.110	15.27	1.100	-7.73	1.94
198.167	289.77	1.770	141.6	0.112	30.34	1.272	-3.94	-0.51
198.188	289.58	1.468	141.1	0.093	13.10	1.164	-5.03	-4.35
198.208	289.66	1.474	138.8	0.082	-49.77	1.075	1.14	-2.59
198.229	289.58	1.883	129.4	0.049	4.66	1.695	-2.03	-3.12
198.250	288.99	2.234	123.1	0.059	5.40	1.652	-3.73	4.92

Appendix F

Tabulation of Datalogger Output

Period-by-period means, standard deviations, and covariances off CR3000 datalogger for the Oil Sands Tailings Pond Field Campaign

Table F.1: Period-by-period means, standard deviations, and covariances of the three wind components (u, v, w)

Julian Day	$\overline{u}$ [m s^{-1}]	$\overline{\sigma_u}$ [m s^{-1}]	$\overline{u'v'}$ [m^2 s^{-2}]	$\overline{u'w'}$ [m^2 s^{-2}]	$\overline{v}$ [m s^{-1}]	$\overline{\sigma_v}$ [m s^{-1}]	$\overline{v'w'}$ [m^2 s^{-2}]	$\overline{w}$ [m s^{-1}]	$\overline{\sigma_w}$ [m s^{-1}]
193.417	-0.9907	0.4032	-0.0062	0.0340	-0.8526	0.6141	0.0085	-0.0322	0.2661
193.438	-1.7979	0.5563	-0.1070	0.0601	-0.0950	0.7321	-0.0252	-0.1147	0.2887
193.458	-2.5924	0.7443	-0.3141	0.1001	1.8352	0.8837	0.0286	-0.1123	0.3844
193.479	-2.4896	0.7377	-0.1228	0.0827	2.0767	0.6053	0.0011	-0.0721	0.3891
193.500	-1.9648	0.6662	-0.0610	0.0833	1.1802	1.0553	0.0216	-0.0692	0.3592
193.521	-1.1965	0.5892	-0.1584	0.0433	1.4617	0.9357	0.0513	-0.0659	0.3378
193.542	-0.9833	0.7376	0.1650	-0.0008	-0.7477	0.6153	-0.0147	-0.0728	0.2835
193.563	-0.1136	0.6376	-0.1219	0.0244	-0.3836	0.7579	0.0130	-0.0927	0.3525
193.583	0.9194	0.5473	-0.0210	0.0260	-0.3092	0.7587	0.0561	-0.0045	0.3421
193.604	1.4290	0.6702	0.0001	0.0172	-0.2074	0.7925	0.0259	0.0812	0.3100
193.625	2.6614	1.1038	0.8272	0.0822	-1.0388	0.9744	0.0602	0.1781	0.3519
193.646	2.9188	0.7767	-0.3207	0.0206	-1.1294	0.7325	0.0221	0.1065	0.2771
193.667	2.4500	0.8778	-0.1044	0.0721	-0.5547	0.7837	0.0190	0.1136	0.3370
193.688	2.9077	0.9058	-0.1201	0.0920	-0.7996	0.9937	0.0259	0.1359	0.3355
193.708	2.9218	0.8103	-0.0391	0.0462	-0.2922	1.1695	0.0668	0.2176	0.3170
193.729	3.2612	0.7184	-0.0739	-0.0232	-0.3504	0.8822	0.0467	0.2308	0.3160
193.750	3.6810	0.7853	0.0462	0.0271	0.2846	0.8645	0.0214	0.2656	0.2854
193.771	3.2368	0.6359	0.0115	0.0119	1.2977	0.7305	0.0121	0.2886	0.2921
193.792	2.9723	0.4473	0.0085	-0.0087	1.4082	0.5298	0.0011	0.2876	0.2514
193.813	3.2369	1.3803	0.4927	0.1131	-1.3890	1.3696	0.0612	0.1875	0.3496
193.833	1.4652	0.7474	0.0994	0.0359	-3.0611	0.7300	0.0450	0.0727	0.2744
193.854	0.3037	1.2576	0.8297	-0.0025	-4.3632	1.5540	-0.0238	0.1116	0.3534
193.875	0.4868	0.7908	0.1133	-0.0152	-5.2110	0.8578	0.0402	0.0486	0.3726
193.896	1.3354	0.5650	0.0493	-0.0137	-4.1890	0.5292	0.0385	0.0292	0.2573
193.917	1.9363	0.3962	0.0089	-0.0072	-3.9930	0.5537	0.0438	0.0309	0.2688
193.938	2.1445	0.3997	0.0232	0.0051	-3.3255	0.4541	0.0668	0.1105	0.2904
193.958	2.0660	0.3484	-0.0005	0.0003	-3.2968	0.4775	0.0664	0.0851	0.2969
193.979	1.4626	0.4206	-0.0075	-0.0164	-3.4459	0.4717	0.0452	0.0165	0.2665
194.000	-0.0223	0.8540	-0.0156	-0.0306	-3.3631	0.5500	0.0277	0.0327	0.2752
194.021	-0.3342	1.4712	0.2139	0.0226	-4.1331	0.6753	0.0501	0.0619	0.2839
194.042	-1.5427	0.5365	0.0355	0.0079	-2.8632	0.6001	0.0073	0.0276	0.2017

194.063	-2.1228	0.2720	0.0311	-0.0025	-3.3734	0.4754	0.0058	0.0164	0.1867
194.083	-1.6155	0.4495	0.1679	0.0061	-2.4491	0.7908	-0.0187	-0.0115	0.1667
194.104	-0.5305	0.2887	0.0692	0.0061	-0.4157	0.5457	-0.0087	-0.0261	0.1132
194.125	0.2159	0.4484	-0.2992	0.0061	-1.8957	0.9448	-0.0234	0.0229	0.1990
194.146	0.0115	0.4041	-0.1686	0.0042	-1.3722	0.6999	-0.0085	0.0354	0.1602
194.167	-0.5810	0.4814	-0.0265	0.0075	-1.0566	0.2752	-0.0060	-0.0094	0.1069
194.188	-1.2664	0.4215	-0.0884	0.0128	-0.7738	0.4523	-0.0128	-0.0531	0.0949
194.208	-1.3205	0.3910	-0.0119	0.0053	-1.5086	0.3831	-0.0057	-0.0407	0.1091
194.229	-0.7230	0.2809	-0.0150	-0.0019	-1.3596	0.3133	-0.0025	-0.0244	0.1342
194.250	-1.1662	0.4547	0.1223	0.0067	-1.4317	0.4594	0.0040	-0.0361	0.1408
194.271	-0.4573	0.5354	-0.0180	0.0107	-1.1388	0.3284	0.0002	-0.0344	0.1752
194.292	0.8459	0.4536	0.1212	-0.0012	-0.8866	0.6810	0.0014	0.0529	0.2376
194.313	1.4607	0.3553	-0.0675	0.0078	-0.0708	0.3655	-0.0100	0.1009	0.2085
194.333	1.2912	0.3154	0.0282	0.0056	0.6220	0.2604	0.0017	0.0980	0.2061
194.354	0.9839	0.6185	-0.0365	0.0307	0.5111	0.3011	0.0037	0.0647	0.2912
194.375	1.1740	0.8329	-0.2032	0.0242	-1.3867	0.6740	0.0099	0.0537	0.3025
194.396	0.7255	0.8108	-0.1436	-0.0188	-2.3723	0.4055	0.0136	0.0098	0.2886
194.438	0.0853	0.4342	0.0647	-0.0210	-1.2314	0.5492	0.0123	-0.0245	0.3549
194.500	1.4091	0.8195	0.5390	0.0487	-1.5851	1.1012	0.1132	0.0681	0.3239
194.521	1.6840	0.4557	-0.1078	-0.0049	0.6068	1.4997	0.1214	0.1285	0.3697
194.542	1.9290	0.7047	-0.3102	-0.0088	0.5262	0.9539	-0.0136	0.1158	0.2937
194.563	2.5980	0.7218	0.2075	0.0325	-0.5456	0.6396	0.0130	0.1339	0.3712
194.583	3.3349	0.6132	-0.1023	0.0215	-0.2438	1.0310	0.0367	0.2002	0.3905
194.646	3.7639	1.1388	-0.1767	0.0630	-2.7586	1.4027	0.0893	0.1708	0.4213
194.667	2.3355	2.6739	1.3293	0.1058	-8.9300	1.7129	0.1532	0.1564	0.5709
194.688	0.6335	2.3202	1.0904	-0.1239	-8.7081	1.9224	0.0577	0.1756	0.5713
194.708	-1.5948	1.7419	0.0105	-0.1546	-9.9091	1.6368	0.1187	0.2417	0.6056
194.729	-0.8246	1.4812	0.0933	-0.0824	-9.2218	1.5390	0.0758	0.1394	0.6035
194.750	-0.5468	1.4029	0.0220	-0.0752	-8.1708	1.3171	0.0646	0.1770	0.5399
194.771	-1.8689	2.6289	0.9768	0.1178	-7.7505	1.5030	0.0591	0.1250	0.5370
194.792	-4.7393	1.4958	0.8649	0.1476	-8.1043	1.6614	-0.0024	0.0709	0.5589
194.813	-6.3017	1.3863	-0.0014	0.2451	-6.9050	1.7009	-0.1287	-0.0977	0.6284
194.833	-6.6317	1.2308	0.7451	0.1675	-3.4666	1.5364	-0.0197	-0.3291	0.5490
194.854	-6.0985	1.1142	0.6368	0.1582	-3.1310	1.4739	-0.0507	-0.2333	0.5320
194.875	-5.0792	1.0568	0.5436	0.1157	-1.5958	1.1579	0.0585	-0.2162	0.4145
194.896	-3.6268	0.9073	-0.0719	0.1373	0.0020	0.8291	-0.0229	-0.1762	0.3665

194.917	-3.8152	1.0455	-0.4023	0.2179	0.5836	0.7043	-0.0508	-0.2678	0.4215
194.938	-2.6471	0.6958	-0.1385	0.0931	0.2706	0.4815	-0.0133	-0.1320	0.2884
194.958	-1.9411	0.3767	0.0187	0.0231	-0.1678	0.3671	0.0014	-0.0874	0.1868
194.979	-1.8862	0.3632	0.0576	0.0264	-0.5740	0.3664	0.0014	-0.0966	0.1890
195.000	-1.8286	0.3290	0.0453	0.0196	-0.7515	0.4086	-0.0036	-0.0866	0.1740
195.021	-1.8397	0.3083	0.0221	0.0188	-1.0607	0.3907	-0.0033	-0.1118	0.1856
195.042	-1.9445	0.2933	0.0219	0.0295	-1.6149	0.5696	-0.0092	-0.0740	0.2365
195.063	-2.0069	0.3831	-0.0202	0.0263	-2.2913	0.3489	0.0077	-0.0469	0.2309
195.083	-1.4573	0.3989	-0.1115	0.0240	-2.8437	0.4328	-0.0146	0.0222	0.2371
195.104	0.3198	1.0372	0.5742	-0.0004	-3.2028	0.9732	0.0334	0.0856	0.2750
195.125	-0.0333	0.4295	-0.0080	-0.0145	-3.2161	0.4891	0.0512	0.0618	0.2902
195.146	0.0270	0.5295	0.0429	-0.0185	-2.4814	0.6690	0.0354	0.1070	0.2977
195.167	-0.1927	0.5054	-0.0107	-0.0133	-1.8171	0.7173	-0.0134	0.0183	0.2987
195.188	0.1034	0.3650	0.0504	-0.0144	-3.0305	0.9850	0.0163	0.0129	0.2921
195.208	0.6074	0.4504	-0.0035	-0.0219	-4.2841	0.4779	0.0540	0.0516	0.3054
195.229	0.7739	0.4853	0.0272	-0.0087	-4.7891	0.4261	0.0335	0.0216	0.3016
195.250	-0.1621	0.6327	-0.0246	-0.0229	-4.5138	0.4798	0.0619	0.1035	0.3232
195.271	0.0715	0.5826	-0.0479	-0.0319	-5.0554	0.6152	0.0697	0.0499	0.3400
195.292	-0.4016	0.6526	-0.2452	-0.0276	-4.6046	0.7791	0.0827	0.0864	0.3510
195.313	-0.8277	0.5072	-0.1041	0.0016	-4.2289	0.5707	0.0311	0.0832	0.3195
195.333	-1.4776	0.4759	0.0993	0.0187	-3.5117	0.6333	0.0282	0.0443	0.2977
195.354	-0.3118	0.5774	0.0455	-0.0027	-2.6424	0.4354	0.0262	0.0529	0.3086
195.375	-0.1529	0.4391	0.0511	0.0032	-2.5567	0.4734	0.0408	0.0272	0.3064
195.396	-0.2541	0.5046	-0.0122	-0.0018	-2.4216	0.4262	0.0197	0.0355	0.3025
195.417	0.4655	0.4733	-0.1310	0.0024	-2.7049	0.6736	0.0338	0.0090	0.3143
195.438	0.2618	0.5583	-0.0685	-0.0091	-3.1436	0.5322	0.0278	-0.0110	0.2875
195.458	-0.3227	0.5259	-0.1643	0.0132	-2.1494	0.7236	0.0079	-0.0177	0.3000
195.479	-2.0594	1.4816	0.3800	0.0930	-3.0354	1.0427	0.0149	-0.0303	0.3743
195.500	-1.9763	1.0457	-0.1118	0.0450	-4.7306	1.4300	-0.0889	0.0545	0.3511
195.521	-1.1870	0.7930	-0.1055	0.0112	-4.1816	1.3585	-0.0155	0.0507	0.3497
195.542	-1.1674	1.3521	0.4749	0.0425	-3.8281	1.7759	0.0032	0.0140	0.3674
195.563	-1.5986	1.1903	-0.1470	0.0516	-3.3339	1.4505	-0.0391	0.0003	0.3479
195.583	-0.7633	1.1700	-0.9082	0.0774	-3.4176	1.6674	-0.0915	0.0762	0.3927
195.604	-0.0476	1.1506	-0.1081	0.0032	-3.5561	1.3224	0.0383	0.0933	0.3674
195.625	-1.1712	0.7581	0.1778	-0.0003	-2.6246	1.8795	-0.1150	-0.0065	0.3383
195.646	0.4374	1.2296	0.6557	0.0778	-1.2277	1.7604	0.0761	0.0312	0.3644

195.667	-1.0027	1.1138	-0.0177	0.0431	-0.7614	1.4665	-0.0362	-0.0650	0.3218
195.688	-2.1919	1.0160	0.2523	0.0643	-0.9757	1.1573	-0.0404	-0.0994	0.3049
195.708	-1.9509	1.1456	0.1452	0.0790	-2.0583	1.2181	-0.0466	-0.0510	0.3045
195.729	-2.1546	0.7793	0.0105	0.0308	-3.4519	1.0352	-0.0367	-0.0432	0.3026
195.750	-1.9943	0.7153	0.1566	0.0399	-2.7343	1.4379	-0.0271	-0.0067	0.2773
195.771	-1.7472	0.6084	-0.1485	0.0459	-1.9243	1.3472	-0.0829	-0.0360	0.2241
195.792	-0.8178	0.6553	0.2554	0.0290	-0.9410	1.1083	0.0266	-0.0258	0.2590
195.813	-0.7890	0.3911	-0.0718	0.0151	-1.4064	0.4541	-0.0018	0.0220	0.2034
195.833	-0.6984	0.3862	0.0387	0.0085	-0.7870	0.3121	-0.0046	-0.0231	0.1711
195.854	0.2482	0.3348	0.0385	-0.0130	-0.1491	0.3424	0.0045	0.0929	0.1649
195.875	1.8205	0.8141	-0.0245	0.0095	0.1520	0.4229	0.0013	0.1657	0.1477
195.896	2.7782	0.2155	-0.0204	-0.0019	0.8016	0.2950	0.0031	0.2295	0.0754
195.917	2.1866	0.2153	0.0044	0.0005	1.5125	0.1221	-0.0007	0.2336	0.0551
195.938	2.2851	0.2664	0.0222	0.0051	1.6820	0.1376	0.0017	0.2563	0.0526
195.958	3.1504	0.4771	-0.0126	0.0043	1.8036	0.3431	-0.0003	0.3000	0.1029
195.979	3.3015	0.4382	0.0096	0.0029	1.3948	0.2672	0.0012	0.3048	0.1341
196.000	3.2668	0.2647	-0.0015	-0.0003	1.8444	0.1831	-0.0013	0.2999	0.1176
196.021	3.4110	0.6227	-0.2951	-0.0092	1.7805	0.6131	-0.0006	0.3007	0.1463
196.042	3.8395	0.3506	0.0541	-0.0029	0.7526	0.3347	0.0063	0.2824	0.1412
196.063	4.1921	0.4453	-0.0010	-0.0052	0.3862	0.2548	0.0004	0.2604	0.1613
196.083	4.0310	0.5213	-0.0097	-0.0076	0.7257	0.3082	0.0062	0.2682	0.2066
196.104	5.3608	0.4993	0.0016	-0.0093	0.7387	0.3293	0.0079	0.3595	0.2258
196.125	5.0964	1.1050	0.3606	0.0525	-0.7778	0.6151	0.0407	0.3507	0.2961
196.146	4.2840	1.1637	0.6780	0.0647	-0.8912	0.8223	0.0646	0.2973	0.2767
196.167	3.6343	2.1261	1.1081	0.2925	-1.0335	1.0037	0.0851	0.2340	0.3070
196.188	4.1617	0.5331	-0.0271	0.0013	-0.9814	0.6144	0.0183	0.2835	0.2431
196.208	4.3373	0.5712	0.1666	0.0021	-1.0283	0.6088	0.0285	0.2731	0.2334
196.229	4.9486	0.4290	-0.0472	-0.0190	-0.5320	0.4388	0.0077	0.3412	0.2719
196.250	4.2269	0.4229	-0.0113	-0.0029	-1.0605	0.4122	0.0142	0.2776	0.2541
196.271	5.1927	0.5863	-0.0049	-0.0187	-0.9698	0.4289	0.0257	0.3394	0.2724
196.292	5.9700	0.5424	-0.0881	-0.0288	-1.0450	0.5592	0.0114	0.3862	0.3013
196.313	4.9511	0.4655	-0.0187	-0.0276	-0.5163	0.6408	0.0157	0.3200	0.2760
196.333	5.3097	0.4125	-0.0100	-0.0273	-1.0544	0.4258	0.0172	0.3426	0.2915
196.354	5.2142	0.5289	-0.0090	-0.0264	-0.7418	0.4256	0.0124	0.3231	0.2933
196.375	4.3104	0.3891	0.0352	-0.0187	-1.0191	0.6558	0.0245	0.2565	0.3159
196.396	4.5652	0.4698	0.0813	-0.0131	-0.9312	0.5956	0.0342	0.3123	0.3325

196.417	4.7318	0.5807	-0.0439	-0.0110	-1.9474	0.5765	0.0249	0.2617	0.3278
196.438	4.3732	0.4961	-0.0207	-0.0155	-1.5740	0.5713	0.0263	0.2402	0.3543
196.458	3.8922	0.6425	-0.0720	0.0033	-1.2275	0.5642	0.0121	0.1940	0.3624
196.479	3.5698	0.4997	-0.0378	-0.0199	-1.3573	0.5994	0.0357	0.2107	0.4310
196.500	3.2452	0.5256	-0.0535	-0.0100	-1.4084	0.4815	0.0185	0.1513	0.4086
196.521	3.1051	0.5559	-0.0537	-0.0118	-1.5300	0.6070	0.0071	0.1274	0.4271
196.542	3.7356	0.7555	-0.1545	0.0218	-1.9377	0.8331	0.0157	0.1613	0.4112
196.563	4.8887	1.0620	0.3105	0.0688	-1.6659	0.8405	0.0846	0.2641	0.3755
196.583	4.8582	1.2811	0.8449	0.1080	-1.7571	1.5071	0.1754	0.2808	0.4194
196.604	4.0798	1.0550	-0.0786	0.0172	-1.4538	1.0033	0.0433	0.2278	0.4094
196.625	4.5427	0.9311	0.2478	0.0243	-0.6824	1.1455	0.0693	0.2854	0.3851
196.646	4.1835	0.9339	-0.0868	0.0411	-1.2368	1.1199	0.0276	0.2822	0.4015
196.667	3.2187	0.9288	-0.1794	-0.0333	-0.4880	0.8217	0.0248	0.2406	0.4095
196.688	2.7280	0.7797	-0.2996	-0.0022	-0.4486	1.0019	0.0312	0.1898	0.3937
196.708	2.3509	1.1581	0.2206	0.0073	-0.1850	0.8381	0.0028	0.2345	0.4015
196.729	1.6562	0.7802	-0.0065	0.0345	-0.1894	0.8505	0.0210	0.1491	0.3973
196.750	0.2395	0.6081	0.0695	-0.0014	-0.8355	0.8170	-0.0259	0.0435	0.3337
196.771	1.0456	0.5836	-0.0658	-0.0144	-1.1030	0.3938	0.0177	0.0766	0.3366
196.792	2.3990	0.6438	0.0117	0.0197	-1.0224	0.4992	0.0080	0.1432	0.3116
196.813	2.6101	0.5800	0.1450	-0.0106	-0.4108	0.7019	0.0260	0.1910	0.2709
196.833	2.7563	0.4111	0.0565	0.0089	-0.7146	0.4233	0.0086	0.1720	0.1516
196.854	1.9356	0.7198	-0.0386	0.0309	-0.7781	0.2035	-0.0020	0.1185	0.0926
196.875	-0.0302	0.4024	-0.0820	0.0038	0.2620	0.3418	0.0008	0.0129	0.0484
196.896	-0.5286	0.3626	-0.0895	0.0054	1.1086	0.2737	-0.0033	0.0120	0.0448
196.917	-2.6163	1.0294	-0.2420	0.1107	1.5914	0.6706	0.0122	-0.0325	0.3691
196.938	-3.3409	0.7944	-0.0441	0.1198	2.5617	0.5584	0.0049	-0.0912	0.4090
196.958	-3.2532	0.9094	-0.2488	0.1190	2.1669	0.6395	-0.0129	-0.0870	0.3918
196.979	-1.9271	0.6546	-0.0813	0.0440	2.3597	0.3786	-0.0152	-0.0477	0.2356
197.000	-3.2306	0.5789	-0.0633	0.0428	2.8071	0.4740	-0.0174	-0.0875	0.2977
197.021	-3.3803	0.6580	-0.1679	0.1006	1.9623	0.6502	0.0096	-0.1294	0.3986
197.042	-2.6737	0.5247	-0.0931	0.0839	1.3975	0.4389	-0.0051	-0.0302	0.3474
197.063	-2.5950	0.5191	-0.0729	0.0422	1.9543	0.4139	-0.0058	-0.0726	0.2451
197.083	-2.7324	0.3645	-0.0507	0.0287	2.1897	0.4293	-0.0109	-0.0632	0.2314
197.104	-2.7413	0.4936	-0.0718	0.0310	2.3485	0.4060	-0.0171	-0.0541	0.2551
197.125	-2.8293	0.5235	-0.0792	0.0414	2.5599	0.4559	-0.0215	-0.0656	0.2810
197.146	-2.8395	0.4153	-0.0275	0.0353	2.6513	0.4137	-0.0210	-0.0625	0.2750

197.167	-3.2269	0.4938	-0.0394	0.0455	2.7790	0.4304	-0.0242	-0.0700	0.2783
197.188	-3.0589	0.6151	-0.0330	0.0666	2.7360	0.4339	-0.0221	-0.0461	0.3032
197.208	-2.8645	0.6633	-0.1618	0.0442	2.5186	0.5272	-0.0177	-0.0383	0.3075
197.229	-3.2041	0.7500	-0.1464	0.0888	2.4955	0.6202	-0.0167	-0.0733	0.3827
197.250	-4.0776	0.7329	-0.0555	0.1048	3.3444	0.6365	-0.0090	-0.0776	0.4037
197.271	-3.9501	0.7326	-0.1126	0.0980	3.2756	0.6346	-0.0389	-0.0739	0.4050
197.292	-4.3353	0.7425	-0.1793	0.1402	2.7294	0.7256	-0.0091	-0.1642	0.4726
197.313	-4.9339	0.8612	-0.2083	0.1874	3.2064	0.7472	-0.0061	-0.1611	0.5011
197.333	-4.5549	0.7948	-0.1876	0.1415	3.0056	0.6646	-0.0008	-0.1819	0.4475
197.354	-4.8985	0.9946	-0.4774	0.1753	3.1793	0.8692	-0.0256	-0.2111	0.4764
197.375	-4.0916	0.8262	-0.2112	0.1708	2.2267	0.7725	0.0030	-0.1559	0.4554
197.396	-4.0170	0.7961	-0.1935	0.1867	2.0910	0.8021	0.0312	-0.1587	0.4937
197.417	-3.9678	0.7532	-0.2576	0.1507	2.4506	0.7334	-0.0232	-0.0989	0.4530
197.438	-4.2850	0.9216	-0.3280	0.2336	2.0980	0.8595	0.0238	-0.1374	0.5654
197.458	-4.4386	1.0218	-0.4101	0.2719	2.0066	0.9245	0.0104	-0.1820	0.5655
197.479	-4.3568	0.8717	-0.3369	0.1806	2.4414	0.9894	0.0193	-0.1891	0.4912
197.500	-4.9501	1.0298	-0.3467	0.2870	2.6338	0.9028	-0.0072	-0.1684	0.6014
197.521	-4.7690	1.0112	-0.2959	0.2935	2.4741	0.9058	0.0109	-0.1512	0.6130
197.542	-4.7390	1.0308	-0.4866	0.2726	2.5077	1.0527	0.0075	-0.1772	0.6092
197.563	-4.9863	1.0329	-0.4850	0.2782	2.8590	1.0195	-0.0061	-0.1723	0.6127
197.583	-5.0492	1.1666	-0.5731	0.3406	2.7234	1.0937	-0.0058	-0.1775	0.6356
197.604	-4.9505	1.1164	-0.7175	0.2540	2.8191	1.1464	0.0153	-0.1739	0.6001
197.625	-4.4651	1.1750	-0.4580	0.3990	1.7476	1.0092	0.0243	-0.1913	0.6369
197.646	-4.1515	1.0823	-0.4205	0.3082	1.2425	0.8772	0.0075	-0.2663	0.5516
197.667	-4.3970	1.1185	-0.4626	0.3315	1.9491	0.9821	0.0261	-0.1862	0.6133
197.688	-4.8119	1.0327	-0.4071	0.2576	2.7736	1.0400	0.0169	-0.1647	0.5845
197.708	-3.9350	0.9808	-0.2990	0.2988	1.4732	0.8010	0.0304	-0.1854	0.5860
197.729	-3.6884	0.9937	-0.3309	0.2541	1.3744	0.7889	0.0352	-0.1551	0.5291
197.750	-3.2726	0.8685	-0.2249	0.2241	1.0832	0.6859	0.0182	-0.1622	0.4953
197.771	-3.2321	0.8878	-0.2481	0.2183	1.1636	0.6978	0.0230	-0.1212	0.5019
197.792	-3.2679	0.8622	-0.1808	0.1926	0.8992	0.6196	-0.0195	-0.2417	0.4289
197.813	-3.2571	0.9164	-0.2937	0.1665	0.4076	0.6978	-0.0394	-0.1781	0.3841
197.833	-4.1267	1.1165	-0.5150	0.2660	0.9176	0.7933	-0.0682	-0.3342	0.4600
197.854	-3.4524	0.9079	-0.2486	0.1915	0.4635	0.6776	-0.0465	-0.2178	0.4081
197.875	-3.3205	0.9449	-0.3249	0.2047	0.4785	0.6725	-0.0464	-0.2037	0.4136
197.896	-2.4564	0.6882	-0.1583	0.1082	0.2998	0.5956	-0.0218	-0.1401	0.3344

197.917	-2.4999	0.6925	-0.1366	0.1140	0.6696	0.4811	-0.0117	-0.2110	0.3441
197.938	-2.7259	0.8586	-0.2642	0.1473	0.7415	0.6013	0.0004	-0.1856	0.3916
197.958	-2.6517	0.8118	-0.2345	0.1534	1.2442	0.7116	0.0303	-0.0599	0.4576
197.979	-2.8899	0.6819	-0.1668	0.1280	1.3822	0.6114	0.0373	-0.0759	0.4607
198.000	-3.1817	0.7677	-0.1929	0.1532	0.7830	0.5634	-0.0179	-0.2346	0.3712
198.021	-2.6052	0.7404	-0.0639	0.1333	0.7155	0.4682	-0.0090	-0.2013	0.3102
198.042	-1.8102	0.4943	-0.0625	0.0478	0.8302	0.3907	0.0022	-0.1153	0.2425
198.063	-1.7034	0.5522	-0.1557	0.0498	0.5009	0.4396	-0.0076	-0.1122	0.1977
198.083	-1.6967	0.3164	-0.0347	0.0206	0.1265	0.3146	-0.0087	-0.1043	0.1495
198.104	-1.9347	0.4214	-0.1520	0.0261	0.6924	0.5807	0.0093	-0.1194	0.1888
198.125	-1.3438	0.3957	-0.1374	0.0136	-0.0240	0.6380	-0.0053	-0.0467	0.1468
198.146	-1.3792	0.3259	-0.0554	0.0189	0.2057	0.2613	-0.0085	-0.1040	0.1304
198.167	-1.5747	0.3315	-0.0697	0.0134	0.8068	0.3451	0.0037	-0.0403	0.1432
198.188	-1.3004	0.1894	-0.0119	0.0065	0.6798	0.2216	0.0057	-0.0549	0.1091
198.208	-1.2767	0.1790	-0.0285	0.0027	0.7340	0.2768	0.0042	-0.0590	0.0875

Table F.2: Period-by-period means and standard deviations of carbon dioxide density (ρ_{CO_2}) and water vapour density (ρ_{H_2O}) and covariances with the three wind components (u, v, w)

Julian Day	$\overline{\rho_{CO_2}}$ [mg m^{-3}]	$\overline{\sigma_{CO_2}}$ [mg m^{-3}]	$\overline{u'\rho_{CO_2}}$ [mg m^{-2}s^{-1}]	$\overline{v'\rho_{CO_2}}$ [mg m^{-2}s^{-1}]	$\overline{w'\rho_{CO_2}}$ [mg m^{-2}s^{-1}]	$\overline{\rho_{H_2O}}$ [g m^{-3}]	$\overline{\sigma_{H_2O}}$ [g m^{-3}]	$\overline{u'\rho_{H_2O}}$ [g m^{-2}s^{-1}]	$\overline{v'\rho_{H_2O}}$ [g m^{-2}s^{-1}]	$\overline{w'\rho_{H_2O}}$ [g m^{-2}s^{-1}]
193.417	674.004	7.3835	1.0931	-1.1295	0.2857	10.9240	0.5221	0.0711	0.0513	0.0396
193.438	665.512	4.2775	0.5039	-1.6654	0.0131	10.9756	0.5269	0.1259	-0.1037	0.0498
193.458	659.888	3.7418	0.0544	-0.2434	0.0952	10.2654	0.5471	0.1942	-0.2112	0.0790
193.479	658.513	3.4851	-0.3745	-0.3234	-0.0275	9.9349	0.4438	0.0951	-0.0327	0.0865
193.500	653.106	2.3344	-0.0505	0.2447	-0.0526	9.5854	0.6039	0.0791	-0.1296	0.0876
193.521	650.703	1.7084	0.1236	0.4669	0.1123	9.1884	0.4427	0.0551	0.0508	0.0774
193.542	650.246	2.3329	-0.5246	0.1779	0.0444	8.8155	0.4248	-0.0351	0.0553	0.0560
193.563	647.301	1.1291	-0.1819	0.3312	-0.0841	8.7707	0.3201	0.0601	0.0089	0.0596
193.583	646.096	2.2764	0.1194	-0.7728	-0.1657	8.9286	0.3073	0.0058	-0.0034	0.0438
193.604	644.318	0.6431	0.0720	0.0879	-0.0863	8.9433	0.3907	-0.0292	-0.0535	0.0577
193.625	643.512	3.0083	-0.3642	-0.4157	-0.0998	10.4823	0.3551	-0.1081	-0.0762	0.0562
193.646	643.185	0.6536	-0.0547	0.0219	-0.0519	9.8958	0.4005	-0.0767	0.0717	0.0394
193.667	642.639	0.7986	0.1606	-0.1334	-0.0825	10.0370	0.4178	0.0676	-0.0023	0.0661
193.688	643.949	0.8868	-0.3229	-0.0688	-0.1310	10.0047	0.4560	-0.0302	0.0723	0.0614
193.708	644.982	2.5834	-0.5071	1.2779	-0.1354	10.1384	0.5002	-0.0502	0.0877	0.0751
193.729	645.694	1.9225	0.0174	-0.5944	-0.1439	10.1295	0.3753	-0.0710	0.0389	0.0571
193.750	642.765	1.6862	-0.4277	0.5537	-0.0748	9.9147	0.3115	0.0116	0.0003	0.0393
193.771	644.187	0.8988	0.0518	0.1867	-0.0437	9.9308	0.5402	-0.0199	0.0707	0.0729
193.792	643.167	1.1486	0.0784	0.1688	-0.0183	9.8470	0.6173	-0.0270	0.0002	0.0817
193.813	638.664	6.7836	0.8081	-1.2307	0.0078	8.4821	0.8977	0.4047	0.5749	0.0891
193.833	636.741	5.2237	0.7225	0.1873	0.1045	7.5908	0.4931	0.0249	0.0949	0.0413
193.854	636.901	2.4170	-0.2496	-0.5099	0.0091	7.4574	0.4404	-0.1146	0.2215	0.0297
193.875	639.375	0.8614	0.3014	0.3982	-0.0078	7.0206	0.4311	-0.0213	0.1560	0.0458
193.896	641.344	0.5429	0.0434	0.0477	0.0158	7.0666	0.4319	0.0050	0.1152	0.0440
193.917	645.283	4.8264	0.2969	0.6371	0.0065	7.3092	0.4394	-0.0403	0.1061	0.0411
193.938	652.304	10.4851	0.9343	0.2283	0.0598	7.5491	0.5492	0.0035	0.1415	0.0886
193.958	657.451	11.3533	0.4600	0.3030	0.2956	8.0052	0.4844	-0.0180	0.1274	0.0743
193.979	658.844	1.3297	-0.2207	-0.0866	0.0212	7.9432	0.3847	-0.0206	0.0895	0.0428
194.000	664.598	3.0306	-1.9380	0.1332	0.0350	7.9906	0.4695	-0.1088	0.0882	0.0504

194.021	672.434	3.4749	-1.6700	-0.6757	-0.0797	8.2146	0.5288	0.0808	0.1486	0.0592
194.042	681.682	2.7974	-1.0039	-0.2341	-0.0086	8.3030	0.3964	0.0028	0.0187	0.0385
194.063	692.499	4.5051	0.2888	1.4272	-0.0678	8.4357	0.3069	0.0061	0.0264	0.0259
194.083	703.443	2.2778	0.6836	1.2198	0.0041	8.6207	0.2414	0.0361	0.0675	0.0100
194.104	704.019	6.2672	0.8763	1.9217	0.0692	8.7272	0.4160	0.0596	-0.0110	0.0246
194.125	702.101	4.3151	1.2688	-3.0115	0.2110	9.1580	0.5200	0.0950	-0.2429	0.0358
194.146	707.425	2.9036	-0.1849	0.2680	-0.0296	9.3651	0.3111	0.0487	-0.0875	0.0083
194.167	706.637	4.0704	-1.2202	0.2349	-0.0243	9.0336	0.4201	0.1503	-0.0207	0.0070
194.188	717.132	5.0769	-0.9110	1.2743	-0.0642	8.4411	0.2421	-0.0110	0.0305	0.0008
194.208	720.418	3.3280	0.5678	0.1232	0.0208	8.1593	0.2508	-0.0171	0.0239	0.0022
194.229	734.301	5.9517	-0.3381	-0.1604	-0.0116	8.4352	0.2955	-0.0073	0.0020	0.0058
194.250	743.283	6.7416	-2.3827	-1.0602	-0.0150	8.0518	0.2510	-0.0097	0.0371	0.0095
194.271	745.398	3.1152	-1.2420	0.0232	-0.0378	7.8706	0.3429	-0.0883	0.0135	0.0220
194.292	750.663	8.3128	2.4559	3.1970	-0.0252	8.4918	0.8084	0.2203	0.3764	0.0293
194.313	760.079	4.2027	0.6734	-0.0587	-0.0284	9.1295	0.2616	0.0374	-0.0439	0.0141
194.333	773.257	6.7524	1.1663	0.4766	0.0914	9.3200	0.2490	0.0421	0.0146	0.0069
194.354	754.802	11.9222	-1.1116	1.8259	-0.0058	8.3276	0.5071	-0.0241	0.0618	0.0205
194.375	761.887	8.5388	-3.9573	0.6829	-0.5243	9.2069	0.6107	-0.2162	-0.0854	-0.0124
194.396	745.312	2.2053	0.1947	-0.0797	-0.1492	8.9863	0.3211	-0.1448	0.0500	0.0261
194.438	718.043	2.7193	-0.4318	-0.6859	-0.2012	9.3005	0.1742	0.0185	0.0230	0.0196
194.500	696.486	5.6232	2.0518	2.1552	-0.0810	9.7749	0.3819	-0.1927	-0.2411	0.0023
194.521	700.725	4.0071	0.1934	3.6667	0.1299	10.3693	0.2981	-0.0124	0.2019	0.0156
194.542	696.966	2.7544	-0.4891	1.5421	-0.1636	9.8934	0.4283	0.0121	0.1236	0.0137
194.563	688.622	3.1401	-0.0175	0.2278	-0.2242	9.6359	0.3144	0.0148	0.0334	0.0454
194.583	672.160	6.1665	-0.3117	0.2340	-0.2317	9.7863	0.2966	-0.0116	-0.0089	0.0419
194.646	651.171	7.3787	-1.1452	-1.6364	-0.0712	9.8290	0.6022	0.1233	-0.0056	0.0393
194.667	638.841	6.9756	4.4939	2.8146	0.4087	7.2285	1.0661	1.2590	0.9030	0.1870
194.688	635.964	1.6024	0.3536	-0.2421	-0.1816	6.3339	0.9245	0.4583	0.8482	0.1580
194.708	636.138	0.8456	-0.1239	-0.5271	-0.0884	5.7033	0.8122	-0.0423	0.4887	0.1525
194.729	636.640	0.6747	-0.1197	-0.2863	-0.1090	5.6111	0.8459	0.1248	0.2950	0.1667
194.750	636.824	1.1310	0.1612	-0.5652	-0.1343	5.7947	0.8337	-0.1846	0.4428	0.1490
194.771	638.992	2.4061	-4.8173	-1.6777	-0.1940	6.3125	0.9904	-1.3387	-0.1580	0.1254
194.792	644.363	2.1214	-1.6047	-1.3920	-0.1110	7.1817	0.5179	0.1752	0.2132	0.0962
194.813	656.349	4.2091	-1.0550	3.0549	-0.3566	8.3919	0.8858	0.0372	0.7977	0.0506
194.833	653.853	7.3478	-0.3941	-2.2973	-0.2148	9.7627	0.3242	0.1697	0.0331	0.0489
194.854	639.289	1.2066	0.3639	0.2720	-0.0140	9.5626	0.3383	0.1279	-0.0250	0.0635

194.875	642.254	0.7956	0.1613	0.0460	0.0085	9.4175	0.2659	0.1087	0.0310	0.0297
194.896	642.548	0.6590	0.1932	0.0387	0.0194	9.4797	0.2323	0.1100	-0.0061	0.0254
194.917	643.900	0.7219	0.3994	-0.0966	0.0775	9.0041	0.1996	0.0484	-0.0030	0.0149
194.938	646.137	0.7911	0.3163	-0.0544	0.0627	9.1257	0.1888	0.0782	-0.0197	0.0179
194.958	651.263	2.7611	0.2816	-0.0646	0.0247	9.2978	0.1689	0.0235	0.0041	0.0103
194.979	659.511	2.9181	0.2404	-0.0428	0.1619	9.5327	0.1969	0.0276	0.0107	0.0123
195.000	665.007	3.9162	0.3949	-0.0192	0.1936	9.6808	0.2589	0.0308	-0.0063	0.0176
195.021	669.103	4.4248	0.2044	0.3522	0.2218	9.5498	0.3229	0.0402	-0.0070	0.0245
195.042	669.643	4.4422	0.2523	1.4389	0.1819	9.5372	0.3829	0.0421	0.0847	0.0386
195.063	667.586	2.2821	0.2574	0.1565	0.0152	9.2784	0.3450	0.0560	0.0283	0.0416
195.083	683.325	9.4859	2.9805	-3.0239	0.4109	9.8421	0.7456	0.2187	-0.1916	0.0665
195.104	707.001	6.5308	0.9980	-2.6417	-0.0300	10.6982	0.5261	0.0085	0.1252	0.0584
195.125	713.964	5.4086	0.0805	-1.2337	-0.1894	10.7909	0.5075	-0.0073	0.0067	0.0527
195.146	711.392	3.0263	-0.1637	1.2576	-0.0955	10.7398	0.4560	-0.0094	0.1573	0.0575
195.167	720.802	2.8403	0.1638	1.2749	-0.1442	10.8104	0.3867	0.0496	-0.0022	0.0463
195.188	723.735	2.8831	0.2203	1.0215	-0.1346	10.9307	0.4440	0.0033	0.1788	0.0606
195.208	719.993	2.7150	0.1884	0.3094	-0.0427	10.5823	0.4827	-0.0209	0.1004	0.0749
195.229	734.102	6.3748	0.2000	-0.2687	-0.2134	10.5735	0.4700	-0.0127	0.0646	0.0708
195.250	741.627	3.7800	-1.0866	0.2671	0.0249	10.2965	0.5170	0.0291	0.1120	0.0784
195.271	736.475	7.3124	-2.2746	1.3632	0.2711	9.7922	0.5703	-0.0929	0.1583	0.0841
195.292	735.759	2.3471	-0.5502	0.2023	-0.1020	9.6295	0.4814	-0.0073	0.1310	0.0825
195.313	735.897	2.2895	0.3896	-0.5177	-0.0847	9.4605	0.4249	0.0411	0.0410	0.0606
195.333	728.145	2.9051	-0.4640	-1.0785	-0.0378	9.4079	0.3585	0.0439	0.0908	0.0528
195.354	717.832	2.2411	-0.6686	-0.3171	-0.1183	9.6543	0.3887	0.0491	0.0744	0.0618
195.375	713.926	1.2167	0.0422	-0.1217	-0.1920	9.6761	0.3507	0.0245	0.0643	0.0634
195.396	706.059	3.3113	-0.8165	0.0114	-0.1814	9.9578	0.3798	0.0240	0.0378	0.0635
195.417	693.857	3.8336	-0.8752	1.5635	-0.2872	10.0600	0.3623	-0.0172	0.0706	0.0650
195.438	678.841	4.9770	1.5419	-1.0959	-0.1672	9.9890	0.4612	0.0112	0.0464	0.0704
195.458	661.539	5.6943	1.4343	-0.7671	0.0624	9.4821	0.5609	0.0934	-0.0283	0.0681
195.479	649.641	1.9753	1.7824	0.5313	-0.1263	8.1394	0.7770	0.8197	0.2527	0.0894
195.500	645.605	1.4613	-0.6488	0.4822	-0.1410	7.6968	0.4335	0.1274	0.0001	0.0540
195.521	641.177	1.7297	-0.1235	-0.9536	-0.1248	8.0104	0.4560	0.0191	0.0778	0.0707
195.542	639.307	1.0097	0.2189	-0.1094	-0.1320	7.7523	0.4857	0.2512	0.2172	0.0766
195.563	637.435	1.4038	-0.2835	0.0234	-0.1101	7.4942	0.4928	0.1746	0.1130	0.0753
195.583	636.372	1.2802	-0.5443	0.4939	-0.2332	7.3691	0.5056	0.0942	-0.0108	0.0963
195.604	635.583	3.1012	1.2996	-0.5608	-0.0324	7.2974	0.5154	-0.0913	0.2100	0.0808

195.625	635.344	1.3344	-0.0903	-0.3559	-0.1045	7.1264	0.4311	0.0336	-0.0712	0.0724
195.646	635.253	2.4521	0.1483	-0.7503	-0.0694	7.1112	0.4283	0.0866	-0.0062	0.0685
195.667	634.288	1.2552	-0.3148	0.7869	-0.1143	7.1641	0.4460	0.0637	-0.3155	0.0485
195.688	635.259	0.9404	-0.2783	0.2378	-0.0908	6.9158	0.3135	0.0196	-0.1362	0.0356
195.708	635.985	1.6908	-0.6179	0.6573	-0.0887	7.1028	0.4221	0.1262	-0.0238	0.0565
195.729	636.882	1.0346	-0.2454	0.2485	-0.0905	6.8140	0.4150	0.0605	0.0314	0.0527
195.750	635.694	1.0906	0.0531	0.1184	-0.0394	6.9762	0.4465	0.0375	0.0817	0.0443
195.771	636.105	1.4164	-0.1510	0.8429	-0.0729	7.1234	0.3831	0.0440	0.0596	0.0330
195.792	636.564	1.1413	-0.0946	0.0881	-0.0423	6.9662	0.3199	-0.0205	-0.1224	0.0312
195.813	635.991	1.4505	-0.0497	0.0923	-0.0286	7.2746	0.4237	-0.0089	0.0326	0.0392
195.833	636.122	1.2547	0.0041	0.0993	-0.0227	7.3508	0.3684	-0.0196	-0.0163	0.0343
195.854	636.656	0.8247	0.0497	0.1065	-0.0099	7.3230	0.3505	0.0104	0.0437	0.0258
195.875	638.244	2.0868	1.0128	0.3549	0.0099	8.0220	0.7609	0.2683	0.0464	0.0442
195.896	641.682	1.9002	-0.2829	0.2264	0.0167	8.3409	0.5086	-0.0614	0.0176	0.0097
195.917	642.750	2.2547	-0.0518	-0.1342	0.0083	8.3511	0.2746	-0.0260	-0.0134	0.0009
195.938	644.299	1.2054	0.1612	0.0577	0.0211	7.9098	0.1817	-0.0270	-0.0079	-0.0018
195.958	651.105	2.2371	-0.0878	-0.3203	0.0209	8.3864	0.3380	-0.0484	-0.0447	0.0033
195.979	656.139	1.9563	-0.4947	-0.0101	0.0195	8.6140	0.3789	-0.0781	0.0028	0.0121
196.000	658.966	2.0278	-0.2852	0.1094	-0.0037	8.5855	0.2018	-0.0282	-0.0006	0.0010
196.021	665.194	2.9019	0.4746	-0.7589	0.0378	8.8021	0.3232	0.0393	-0.0958	0.0093
196.042	673.821	2.4322	-0.3814	-0.0571	0.0009	9.4981	0.4719	-0.1231	-0.0759	0.0103
196.063	673.114	2.6699	-0.8715	-0.0658	-0.0253	9.6699	0.3684	-0.0746	0.0101	0.0166
196.083	680.050	1.6877	0.3283	0.0732	0.0580	10.0782	0.3815	-0.1320	0.0106	0.0232
196.104	686.649	1.9310	0.2240	0.0878	0.0830	9.8903	0.2501	-0.0348	-0.0007	0.0210
196.125	691.955	5.9554	-5.6791	-2.4978	-0.4749	10.0689	0.2679	0.0328	0.0613	0.0321
196.146	706.672	5.0011	-2.0956	-0.7783	-0.2521	10.1311	0.2645	-0.1122	-0.0130	0.0061
196.167	708.282	10.8605	-21.3267	-5.1660	-1.6097	10.3813	0.4685	-0.8410	-0.1607	-0.0411
196.188	709.666	3.5070	0.6446	-0.8060	0.0624	10.1764	0.1744	-0.0345	-0.0177	0.0083
196.208	710.209	4.1329	1.2763	1.3592	0.0451	10.3983	0.1781	-0.0029	0.0417	0.0093
196.229	715.621	2.8135	0.1948	-0.1643	-0.0430	10.7238	0.2172	-0.0422	0.0047	0.0212
196.250	720.507	2.2174	0.0665	0.0147	-0.0480	11.1046	0.1655	-0.0249	0.0104	0.0096
196.271	728.177	2.9624	1.1942	0.1603	0.0546	11.3125	0.1974	-0.0199	0.0245	0.0201
196.292	728.909	2.3218	0.2187	0.2541	0.0421	11.2505	0.2124	-0.0381	0.0183	0.0230
196.313	731.280	2.7694	-0.5535	0.4301	0.0762	11.1511	0.2098	-0.0448	0.0006	0.0235
196.333	728.520	4.0610	-0.5338	-0.2261	-0.1422	11.3306	0.1997	-0.0327	0.0150	0.0267
196.354	718.321	2.6490	0.7445	0.1399	-0.1117	11.3284	0.2143	-0.0365	0.0068	0.0287

196.375	707.606	3.1278	0.1833	0.3582	-0.2413	11.3700	0.1760	-0.0149	0.0273	0.0218
196.396	703.439	4.0962	0.7167	1.0606	-0.1417	11.2210	0.1927	-0.0099	0.0125	0.0290
196.417	689.399	6.2757	-2.0133	1.6195	-0.2447	11.3192	0.2394	-0.0113	-0.0144	0.0212
196.438	678.388	4.9969	-0.7793	0.8483	-0.3088	11.5276	0.2685	-0.0201	-0.0090	0.0317
196.458	671.225	3.1241	-0.3717	0.8302	-0.2373	11.8691	0.2394	-0.0830	0.0230	0.0213
196.479	660.491	8.0798	-1.7886	1.7686	-0.4016	12.2728	0.2312	-0.0013	-0.0110	0.0274
196.500	647.873	2.7589	0.0345	-0.2699	-0.3760	12.3444	0.2606	0.0038	-0.0347	0.0267
196.521	635.447	6.5441	-1.6594	1.4939	-0.3399	12.1923	0.3217	-0.0530	0.0244	0.0401
196.542	622.195	4.2346	-1.1289	1.8866	-0.5715	11.4472	0.6771	-0.0864	0.2433	0.0491
196.563	614.197	5.3495	0.7541	-0.0472	-0.3439	10.1667	0.6552	0.1559	0.0676	0.0896
196.583	610.151	4.2612	-0.5998	-1.5801	-0.4545	9.6868	0.5019	0.0308	-0.1392	0.0593
196.604	609.201	2.5229	-0.0230	-0.5651	-0.4060	9.5628	0.5992	0.0344	-0.1400	0.0499
196.625	608.056	1.5173	-0.0045	-0.3655	-0.3559	9.6177	0.5074	-0.0675	-0.1175	0.0631
196.646	608.429	1.7829	0.2272	-0.3536	-0.3440	9.4817	0.5852	0.0613	-0.2464	0.0688
196.667	607.552	1.3601	0.2998	-0.0502	-0.3654	9.0461	0.2925	0.0113	0.0271	0.0390
196.688	608.253	1.2006	0.0995	-0.0679	-0.3036	8.9749	0.4503	0.0699	-0.2429	0.0297
196.708	609.484	1.3307	0.1229	0.1132	-0.2953	8.9770	0.4308	0.0576	-0.0591	0.0425
196.729	608.494	1.3902	0.0848	0.2567	-0.2496	8.5958	0.3054	0.0513	-0.0198	0.0234
196.750	608.974	1.3785	-0.1144	0.2853	-0.2372	8.7633	0.4544	-0.0784	-0.1244	0.0421
196.771	609.221	1.6665	0.1297	-0.0104	-0.2075	8.8994	0.3214	0.0432	-0.0442	0.0261
196.792	611.635	1.7565	0.2187	0.2342	-0.1715	9.1310	0.4094	-0.0521	-0.0130	0.0340
196.813	614.033	0.8037	0.0029	-0.0341	-0.1097	9.4437	0.6377	-0.0449	-0.1786	0.0266
196.833	613.879	0.6818	-0.1150	-0.0682	-0.0297	10.1154	0.8522	-0.0906	-0.1046	0.0184
196.854	614.418	0.5760	-0.3041	0.0414	-0.0190	10.8896	0.9815	-0.2242	0.0478	0.0082
196.875	618.706	3.5398	-0.7771	0.6792	-0.0122	11.3991	0.6273	-0.0660	0.0023	0.0014
196.896	617.700	2.9148	-0.0942	0.0184	-0.0096	9.7077	0.2722	0.0287	-0.0225	0.0016
196.917	636.218	12.2187	-2.4432	-2.1722	0.2603	11.8329	1.5083	-1.0851	0.0196	-0.0263
196.938	642.255	3.0140	1.1238	-0.1394	0.3343	13.8404	0.1778	0.0787	-0.0121	0.0168
196.958	644.456	3.7892	1.9668	-0.2843	0.2429	13.2952	0.1426	0.0740	-0.0211	0.0132
196.979	655.662	3.7314	-0.7397	0.1165	0.0363	13.3470	0.1264	0.0460	-0.0152	0.0094
197.000	662.817	4.3238	0.3614	-0.3414	0.1522	13.1276	0.1242	0.0485	-0.0167	0.0068
197.021	653.751	2.9568	0.7040	-0.3942	0.1872	13.1308	0.1921	0.0457	-0.0763	0.0093
197.042	658.180	2.8903	0.2459	0.1355	0.1884	13.6152	0.1075	0.0145	-0.0138	0.0106
197.063	665.897	6.3421	1.7739	-0.5148	0.1958	13.8381	0.1262	0.0423	-0.0230	0.0060
197.083	680.162	7.8258	0.3878	-0.6347	-0.0218	14.2355	0.2084	0.0113	-0.0140	0.0002
197.104	681.473	5.2063	-0.0532	-0.5589	0.1132	14.5584	0.0602	0.0131	-0.0042	0.0040

197.125	673.675	1.4156	0.1413	-0.1886	0.0400	14.4774	0.0492	0.0161	-0.0105	0.0040
197.146	680.390	2.8867	-0.0902	-0.0959	0.0497	14.4124	0.0522	0.0096	-0.0028	0.0037
197.167	682.696	3.0627	0.0255	-0.5754	0.1750	14.3387	0.0699	0.0191	-0.0067	0.0044
197.188	678.824	4.5447	0.1648	-0.5496	0.1341	14.1327	0.0773	0.0096	-0.0104	0.0047
197.208	683.643	1.8977	-0.2198	-0.1091	0.0624	13.9567	0.1195	0.0301	-0.0185	0.0040
197.229	682.277	3.7494	0.9528	-0.5029	0.2048	13.6648	0.1168	0.0401	-0.0072	0.0070
197.250	681.207	5.7512	1.6996	0.7336	0.3080	13.4188	0.0626	0.0247	-0.0062	0.0055
197.271	683.631	4.6165	-0.0583	-0.4045	0.0773	13.3651	0.0774	0.0312	-0.0113	0.0059
197.292	676.821	7.8272	0.6440	0.3993	-0.0058	13.1773	0.0922	0.0210	-0.0086	0.0046
197.313	671.242	2.7317	0.6861	-0.0138	0.2067	12.9961	0.0977	0.0286	-0.0302	0.0066
197.333	672.080	3.1587	0.7955	-0.0535	0.1845	12.8545	0.0898	0.0330	-0.0197	0.0052
197.354	669.697	2.4303	0.3969	0.2051	0.1552	12.7006	0.0658	0.0322	-0.0289	0.0066
197.375	670.305	3.4742	0.2130	1.1164	0.1111	12.7383	0.0956	0.0357	-0.0247	0.0131
197.396	667.982	1.6026	0.1590	0.3136	0.0876	12.6783	0.0950	0.0201	-0.0253	0.0078
197.417	667.361	2.3565	0.3188	0.0030	0.1015	12.5537	0.0885	0.0343	-0.0355	0.0096
197.438	664.705	2.2248	-0.0399	0.6730	0.0575	12.5165	0.0833	0.0280	-0.0102	0.0130
197.458	662.162	1.8713	-0.5207	0.8683	-0.0366	12.4170	0.0908	0.0371	-0.0261	0.0126
197.479	660.614	2.5750	-0.2640	0.8248	0.0305	12.4362	0.0900	0.0337	-0.0201	0.0137
197.500	660.375	3.5988	0.5573	-0.0549	0.0632	12.5501	0.0966	0.0254	-0.0224	0.0125
197.521	654.366	1.8905	-0.1292	0.1972	0.0218	12.7062	0.0896	0.0385	-0.0262	0.0109
197.542	650.798	1.8613	-0.0394	0.6672	0.0569	12.8248	0.1143	0.0527	-0.0642	0.0106
197.563	649.516	1.6469	0.3117	-0.0368	0.1374	12.8433	0.0786	0.0384	-0.0276	0.0120
197.583	646.168	1.9714	0.3193	-0.0901	0.1014	12.9064	0.0953	0.0532	-0.0381	0.0141
197.604	641.552	1.8616	-0.2201	0.9104	0.1069	12.9789	0.1269	0.0702	-0.0701	0.0098
197.625	636.771	1.2978	-0.2195	0.3068	-0.0408	13.2637	0.1124	0.0603	-0.0255	0.0194
197.646	635.507	0.8222	0.0038	0.1842	0.0247	13.4936	0.1165	0.0496	-0.0159	0.0150
197.667	635.074	1.2028	0.0840	0.2347	0.0350	13.3943	0.1004	0.0493	-0.0328	0.0136
197.688	633.038	1.8176	-0.1145	0.7054	0.0512	13.3668	0.1331	0.0608	-0.0605	0.0084
197.708	630.188	1.3385	0.0147	0.2505	0.0892	13.5863	0.0911	0.0298	-0.0055	0.0132
197.729	626.171	1.5367	0.1863	0.2917	0.1528	13.7003	0.1193	0.0357	-0.0197	0.0091
197.750	620.398	0.8138	0.0478	-0.0293	0.0114	14.0824	0.1405	0.0344	-0.0012	0.0158
197.771	618.213	0.9451	-0.0122	0.1664	0.0404	14.4104	0.1441	0.0458	-0.0194	0.0119
197.792	616.724	0.9720	0.2163	0.0575	0.0619	14.7267	0.1042	0.0330	0.0001	0.0103
197.813	616.098	0.8076	-0.1426	0.0615	-0.0243	14.7924	0.2024	0.0911	-0.0256	0.0170
197.833	621.005	1.0737	0.0862	-0.0121	0.0243	14.0732	0.2139	0.0540	-0.0055	0.0142
197.854	623.225	0.6326	0.0608	-0.0699	0.0453	13.8413	0.1102	0.0471	0.0013	0.0111

197.875	625.797	0.9717	0.2600	-0.0921	0.0499	13.5790	0.1345	0.0371	-0.0077	0.0140
197.896	628.003	0.5525	0.0928	0.0319	0.0384	13.5691	0.1832	0.0548	-0.0497	0.0155
197.917	630.574	1.3413	0.2585	0.0261	0.0320	13.2269	0.1220	0.0205	-0.0059	0.0093
197.938	633.380	0.6041	0.2220	-0.0240	0.0785	12.9169	0.1328	0.0569	-0.0182	0.0074
197.958	636.385	2.4266	-0.0589	0.7788	0.2455	12.7074	0.1339	0.0559	-0.0389	0.0073
197.979	641.454	2.0514	0.1786	0.0906	0.1732	12.4231	0.0926	0.0122	0.0069	0.0088
198.000	643.843	1.8087	0.2334	0.1449	0.0903	12.0986	0.1528	0.0487	0.0133	0.0180
198.021	649.645	4.6403	1.5970	0.6898	0.3826	11.9029	0.0983	0.0242	-0.0022	0.0081
198.042	661.823	6.0073	0.1332	0.7617	0.1715	11.8678	0.1341	0.0188	-0.0289	0.0048
198.063	655.866	2.2996	-0.0048	0.0522	0.0188	11.8880	0.1191	0.0113	-0.0066	0.0036
198.083	653.915	1.7902	-0.0111	0.0232	0.0119	11.7335	0.1140	0.0062	-0.0014	0.0036
198.104	659.481	6.2085	-0.9549	2.7649	0.2596	11.6261	0.1497	0.0316	-0.0191	0.0076
198.125	667.924	5.6990	-1.0061	2.0297	0.0597	11.7566	0.1325	0.0266	-0.0264	0.0047
198.146	667.759	3.3998	-0.1565	0.0662	0.0496	11.8084	0.1330	-0.0084	0.0062	0.0004
198.167	679.679	6.6070	-0.4605	1.3650	0.0531	11.7312	0.1108	0.0187	-0.0252	0.0006
198.188	686.231	4.9598	0.1047	0.6632	0.0801	11.7100	0.0848	0.0014	-0.0122	-0.0013
198.208	698.195	4.1328	-0.1181	0.5829	0.0621	11.7726	0.0987	0.0095	-0.0199	-0.0004

Table F.3: Period-by-period means and standard deviations of methane density (ρ_{CH_4}) and covariances with the three wind components (u, v, w) and signal strength (RSSI). NA values for signal strength indicate an LI-7700 signal strength less than 10%.

Julian Day	$\overline{\rho_{CH_4}}$ [mmol m^{-3}]	$\overline{\sigma_{CH_4}}$ [mmol m^{-3}]	$\overline{u'\rho'_{CH_4}}$ [mmol m^{-2} s^{-1}]	$\overline{v'\rho'_{CH_4}}$ [mmol m^{-2} s^{-1}]	$\overline{w'\rho'_{CH_4}}$ [mmol m^{-2} s^{-1}]	RSSI [%]
193.417	0.0818	4.99E-07	8.51E-05	-1.20E-04	1.62E-05	29.31
193.438	0.0819	5.87E-07	-1.94E-04	2.92E-04	-3.16E-05	29.50
193.458	0.0810	2.25E-06	4.38E-04	-7.90E-04	-2.73E-05	29.99
193.479	0.0794	2.72E-07	6.69E-05	1.99E-05	-3.95E-05	29.97
193.500	0.0793	9.17E-08	2.77E-05	-6.32E-05	-2.46E-05	29.80
193.521	0.0794	1.40E-07	-2.93E-05	-7.39E-05	-4.64E-05	29.74
193.542	0.0795	1.57E-06	-4.43E-05	1.66E-05	-2.40E-06	29.40
193.563	0.0789	3.41E-07	-1.32E-04	2.10E-04	9.96E-06	29.00
193.583	0.0778	1.25E-07	-3.52E-05	-1.79E-04	-4.49E-05	28.69
193.604	0.0774	3.77E-08	-9.90E-06	3.27E-05	-1.90E-05	26.57
193.646	0.0773	2.89E-08	2.69E-05	-3.47E-05	-1.38E-05	26.55
193.667	0.0780	7.63E-07	2.02E-04	-9.76E-05	-7.06E-07	26.50
193.688	0.0800	3.72E-07	-2.58E-04	-5.50E-05	-5.78E-05	26.19
193.708	0.0787	1.82E-07	-6.06E-05	3.15E-04	1.73E-05	26.17
193.729	0.0782	1.28E-07	8.45E-05	-5.36E-05	-6.29E-06	25.89
193.750	0.0791	1.51E-07	-6.30E-06	-1.53E-04	-9.49E-06	25.54
193.771	0.0784	1.93E-07	3.57E-05	-9.88E-05	-2.03E-05	25.10
193.792	0.0784	1.04E-07	2.27E-05	-3.27E-05	-6.56E-06	24.64
193.813	0.0777	3.14E-07	2.74E-04	3.71E-04	1.87E-05	24.48
193.833	0.0767	1.66E-07	5.48E-05	1.14E-04	5.61E-06	24.84
193.854	0.0763	4.72E-08	-1.69E-04	-6.90E-05	-5.61E-06	24.90
193.875	0.0767	4.17E-08	6.43E-05	6.10E-05	-1.05E-05	24.89
193.896	0.0770	3.18E-08	4.10E-05	-7.06E-06	-7.38E-06	24.49
193.917	0.0774	3.17E-08	1.55E-05	4.21E-06	-6.18E-06	24.50
193.938	0.0779	5.64E-08	1.56E-05	3.01E-06	-3.08E-06	24.66
193.958	0.0784	5.79E-08	-1.04E-05	-2.72E-05	-1.49E-05	24.61
193.979	0.0789	4.00E-08	-1.57E-05	-2.25E-05	-6.50E-06	24.49
194.000	0.0796	1.09E-07	-1.65E-04	1.87E-05	-8.16E-06	24.51
194.021	0.0802	1.49E-07	6.55E-06	-9.56E-05	-1.74E-05	24.44
194.042	0.0807	3.53E-08	-2.03E-05	1.36E-05	-5.96E-06	24.39
194.063	0.0812	7.50E-08	1.21E-05	6.14E-05	-9.67E-06	24.32
194.083	0.0830	1.14E-06	7.84E-05	5.27E-04	-4.21E-05	24.23
194.104	0.0850	1.32E-06	-2.21E-05	-2.25E-04	2.15E-05	24.07
194.125	0.0838	1.42E-06	-2.90E-04	8.36E-04	-1.08E-05	23.85
194.146	0.0823	3.15E-08	-1.77E-05	2.39E-05	-4.85E-06	23.69
194.167	0.0823	2.58E-08	-2.84E-05	7.95E-06	-3.21E-07	23.66
194.188	0.0827	1.59E-07	-8.66E-05	1.09E-04	-9.56E-06	23.52
194.208	0.0829	5.01E-08	2.57E-05	1.46E-05	8.60E-07	23.28
194.229	0.0839	3.59E-07	-8.04E-06	-2.83E-05	-2.39E-06	23.09
194.250	0.0850	2.68E-07	-1.91E-04	-1.17E-04	-4.61E-06	23.15
194.271	0.0852	5.50E-08	-7.87E-05	1.05E-07	-7.96E-06	23.08
194.292	0.0856	2.39E-07	1.25E-04	2.38E-04	-7.06E-06	22.96
194.313	0.0857	4.30E-08	1.47E-05	8.04E-06	-8.67E-06	22.78
194.333	0.0867	5.64E-07	1.28E-04	4.66E-05	1.12E-05	22.35
194.354	0.0864	5.55E-07	3.26E-06	1.03E-04	-3.10E-06	21.53
194.375	0.0865	2.08E-07	-1.49E-04	-2.98E-05	-3.76E-05	21.11
194.396	0.0898	4.99E-06	-8.61E-04	1.93E-04	-1.08E-04	20.97
194.438	0.0948	7.45E-05	2.10E-04	8.53E-04	5.72E-05	21.55
194.500	0.0927	6.87E-07	-1.52E-04	-4.59E-04	-7.47E-05	23.16
194.521	0.0956	2.37E-06	5.00E-05	-3.72E-04	-8.07E-05	23.45

194.542	0.0920	1.54E-06	-1.98E-04	6.35E-04	-3.10E-05	23.08
194.563	0.0890	1.19E-06	-3.42E-04	-1.66E-04	-4.15E-05	22.54
194.583	0.0852	1.84E-06	-1.39E-04	-1.89E-04	-7.06E-05	21.90
194.646	0.0795	6.81E-07	-3.30E-04	2.46E-04	-5.06E-05	29.99
194.667	0.0764	7.05E-08	4.62E-05	9.67E-05	-3.76E-05	31.61
194.688	0.0763	3.86E-08	-3.69E-05	-1.58E-04	-3.86E-05	30.31
194.708	0.0767	7.86E-08	-6.10E-05	-1.54E-04	-2.33E-05	28.02
194.729	0.0774	3.71E-08	5.38E-05	-4.11E-06	-2.55E-05	25.32
194.750	0.0775	3.16E-08	-2.62E-05	1.04E-05	-2.43E-05	23.93
194.771	0.0780	4.16E-07	-1.45E-03	-3.28E-04	-4.59E-05	22.93
194.792	0.0814	6.72E-06	-2.02E-03	-1.16E-03	-6.75E-05	17.08
194.813	0.0941	1.62E-05	-8.63E-04	3.52E-03	-2.68E-04	10.80
194.833	0.0998	1.18E-06	8.77E-05	-3.40E-04	6.35E-06	NA
194.854	0.0989	6.70E-07	4.00E-04	2.76E-04	2.21E-05	NA
194.875	0.0998	2.92E-07	1.42E-04	1.03E-04	3.98E-06	NA
194.896	0.0994	5.97E-08	4.23E-05	-6.58E-06	6.52E-06	NA
194.917	0.0993	3.74E-07	-1.93E-04	1.26E-04	-1.93E-05	NA
194.938	0.0992	1.01E-07	3.91E-05	1.23E-05	5.06E-06	NA
194.958	0.0999	1.41E-06	1.96E-04	-4.16E-05	5.45E-05	NA
194.979	0.1022	3.44E-06	2.69E-04	-4.34E-05	1.43E-04	NA
195.000	0.1042	4.91E-06	2.24E-04	-1.45E-04	1.17E-04	NA
195.021	0.1044	5.13E-06	2.09E-04	-1.10E-04	9.88E-05	NA
195.042	0.1050	6.92E-06	1.32E-04	3.98E-04	-4.49E-05	NA
195.063	0.1024	4.48E-07	2.86E-05	3.51E-06	3.20E-06	NA
195.083	0.1060	8.36E-06	9.10E-04	-9.48E-04	1.76E-04	NA
195.104	0.1083	3.51E-06	-5.37E-04	4.03E-04	1.73E-05	NA
195.125	0.1074	7.73E-07	1.21E-05	-2.00E-04	-3.27E-05	NA
195.146	0.1070	2.55E-07	-1.94E-05	1.77E-04	2.15E-06	NA
195.167	0.1081	4.17E-07	-1.72E-05	1.02E-04	2.77E-05	NA
195.188	0.1083	1.89E-07	-2.51E-05	-3.42E-05	1.17E-05	NA
195.208	0.1089	3.42E-07	3.18E-05	-7.05E-05	-3.70E-05	NA
195.229	0.1103	6.26E-07	-2.90E-05	-5.72E-05	-3.25E-05	NA
195.250	0.1117	1.23E-06	-5.15E-04	4.11E-05	-2.37E-06	NA
195.271	0.1112	1.24E-06	-4.25E-04	1.64E-04	2.29E-05	NA
195.292	0.1116	1.60E-06	-5.33E-04	4.14E-04	-2.46E-05	NA
195.313	0.1127	1.73E-06	-4.07E-04	2.05E-04	-1.04E-04	NA
195.333	0.1131	1.76E-06	1.04E-04	-4.16E-06	-8.22E-06	NA
195.354	0.1126	1.37E-06	-1.70E-04	-6.29E-05	-1.10E-04	NA
195.375	0.1155	2.33E-06	-3.97E-04	-3.05E-04	-1.10E-04	NA
195.396	0.1169	1.04E-06	-1.32E-04	-5.59E-05	-8.17E-05	NA
195.417	0.1188	1.05E-06	1.98E-04	-3.74E-04	-2.55E-05	NA
195.438	0.1179	1.52E-06	3.28E-04	-2.94E-04	-4.48E-05	NA
195.458	0.1134	5.59E-06	2.22E-04	-3.62E-05	-5.08E-06	NA
195.479	0.1066	5.21E-06	2.61E-03	4.54E-04	5.22E-05	NA
195.500	0.1044	2.77E-07	3.01E-05	6.00E-05	-7.69E-06	NA
195.521	0.1023	9.41E-06	-2.29E-05	-2.24E-04	2.93E-06	NA
195.542	0.1005	3.14E-07	2.51E-04	5.26E-04	-1.99E-05	NA
195.563	0.0998	1.39E-05	4.61E-05	4.49E-05	-1.24E-05	NA
195.583	0.0995	1.21E-07	-5.45E-05	-6.33E-05	-4.37E-05	NA
195.604	0.0992	1.03E-07	8.99E-05	-8.30E-05	-1.81E-05	NA
195.625	0.0990	1.19E-07	-2.07E-05	-1.88E-04	-1.92E-05	NA
195.646	0.0989	1.10E-07	3.66E-05	-1.70E-05	-1.10E-05	NA
195.667	0.0988	1.53E-07	7.78E-05	1.46E-04	-1.95E-05	NA
195.688	0.0986	8.93E-08	-2.88E-06	4.43E-05	-2.16E-05	NA
195.708	0.0991	1.42E-07	-1.25E-04	1.39E-06	-2.58E-05	NA
195.729	0.0998	2.70E-07	-2.25E-05	4.02E-05	-2.48E-05	NA
195.750	0.0993	1.20E-07	4.53E-05	-1.96E-04	-7.26E-06	NA
195.771	0.0996	1.03E-07	4.71E-05	-1.68E-04	2.72E-06	NA
195.792	0.1001	2.26E-05	-1.27E-05	-4.04E-05	-2.52E-05	NA
195.813	0.1007	1.38E-07	-9.41E-06	-3.96E-06	-9.97E-06	NA

195.833	0.1009	1.68E-07	1.52E-05	3.99E-07	-8.56E-06	NA
195.854	0.1009	2.89E-07	5.37E-05	3.47E-05	-9.37E-06	NA
195.875	0.1015	4.17E-07	2.64E-04	-1.46E-05	3.36E-06	NA
195.896	0.1028	3.15E-07	-2.91E-05	1.00E-04	4.27E-06	NA
195.917	0.1042	2.49E-07	-6.05E-05	-7.95E-06	-4.24E-06	NA
195.938	0.1044	1.84E-07	6.28E-05	2.63E-05	5.59E-06	NA
195.958	0.1058	1.50E-07	7.16E-05	-6.35E-05	4.29E-06	NA
195.979	0.1072	3.80E-07	-2.91E-06	2.23E-05	7.95E-06	NA
196.000	0.1085	3.24E-07	-4.99E-05	1.87E-05	-1.07E-05	NA
196.021	0.1093	5.49E-07	2.41E-04	-2.87E-04	8.84E-06	NA
196.042	0.1127	3.08E-06	-2.80E-04	-1.98E-04	-2.60E-05	NA
196.063	0.1146	1.84E-06	-3.09E-04	-1.05E-05	-2.83E-05	NA
196.083	0.1206	1.99E-06	4.78E-04	5.37E-05	2.66E-05	NA
196.104	0.1254	9.52E-07	1.48E-04	6.95E-05	2.81E-05	NA
196.125	0.1219	1.44E-06	6.61E-04	4.44E-04	4.85E-05	NA
196.146	0.1203	4.40E-07	-4.47E-04	-1.84E-04	-2.06E-05	NA
196.167	0.1210	1.31E-06	-1.76E-03	-4.51E-04	-1.26E-04	NA
196.188	0.1206	1.95E-07	-2.54E-05	-4.92E-06	1.88E-05	NA
196.208	0.1205	2.07E-07	6.86E-05	1.31E-04	9.46E-06	NA
196.229	0.1217	4.04E-07	-1.94E-05	-3.82E-05	4.13E-06	NA
196.250	0.1242	8.74E-07	1.46E-05	8.06E-05	-3.31E-05	NA
196.271	0.1263	7.47E-07	3.18E-04	3.30E-07	-2.98E-05	NA
196.292	0.1278	1.28E-06	-1.82E-04	2.45E-04	-7.00E-05	NA
196.313	0.1306	3.97E-06	3.10E-04	-7.85E-04	-1.53E-04	NA
196.333	0.1361	7.34E-06	4.94E-04	1.11E-04	-5.57E-05	NA
196.354	0.1383	6.36E-06	8.77E-04	1.03E-04	2.27E-06	NA
196.375	0.1341	5.69E-07	-6.89E-05	-1.34E-04	-3.26E-05	NA
196.396	0.1326	1.23E-06	1.20E-04	3.57E-04	-8.07E-06	NA
196.417	0.1301	2.59E-06	-5.04E-04	4.16E-04	-3.94E-05	NA
196.438	0.1285	9.47E-07	2.35E-04	-1.75E-04	-3.44E-05	NA
196.458	0.1314	2.06E-06	-2.16E-04	-2.26E-04	-5.96E-05	NA
196.479	0.1313	4.99E-07	-5.51E-05	-8.17E-05	-4.84E-05	NA
196.500	0.1303	4.65E-06	9.12E-05	-1.27E-04	-2.16E-05	NA
196.521	0.1331	1.46E-06	-2.65E-04	1.33E-04	-4.18E-05	NA
196.542	0.1309	1.16E-06	-3.76E-04	4.53E-04	-7.55E-05	NA
196.563	0.1285	7.31E-07	1.32E-04	1.46E-04	1.17E-06	NA
196.583	0.1274	1.23E-06	-4.37E-04	-3.91E-04	-1.06E-04	NA
196.604	0.1275	5.41E-07	-2.56E-05	2.55E-04	-3.35E-05	NA
196.625	0.1274	3.20E-07	-1.33E-04	4.62E-05	-3.44E-05	NA
196.646	0.1274	3.16E-07	-1.64E-04	1.34E-04	-5.49E-05	NA
196.667	0.1277	3.70E-07	-2.09E-04	8.08E-05	-1.46E-05	NA
196.688	0.1288	1.08E-06	-1.95E-04	7.90E-06	-2.84E-05	NA
196.708	0.1296	6.24E-07	-4.66E-04	-8.51E-05	-3.29E-05	NA
196.729	0.1302	8.51E-07	-1.35E-04	-2.38E-04	-4.99E-05	NA
196.750	0.1310	1.37E-06	-3.01E-04	-1.44E-04	-3.64E-05	NA
196.771	0.1311	7.19E-07	-1.18E-04	-1.54E-05	-1.20E-05	NA
196.792	0.1309	5.00E-07	-1.47E-04	-1.93E-05	-1.01E-05	NA
196.813	0.1314	2.16E-06	-3.93E-05	-7.77E-05	-1.29E-05	NA
196.833	0.1328	4.94E-07	5.16E-05	-3.19E-05	6.60E-06	NA
196.854	0.1343	6.19E-07	-3.58E-04	3.10E-05	-2.43E-05	NA
196.875	0.1359	8.25E-07	-1.00E-04	1.09E-04	-3.03E-06	NA
196.896	0.1380	1.46E-06	-1.25E-04	3.46E-05	-1.00E-05	NA
196.917	0.1498	7.06E-05	-4.98E-03	-3.48E-05	9.42E-05	NA
196.938	0.1595	3.09E-06	7.61E-04	-5.43E-05	1.25E-04	NA
196.958	0.1573	2.09E-06	8.58E-04	-2.46E-04	4.84E-05	NA
196.979	0.1689	2.29E-05	-9.49E-04	3.71E-04	-4.01E-05	NA
197.000	0.1740	3.14E-05	1.37E-03	1.71E-04	9.27E-05	NA
197.021	0.1553	6.06E-06	5.79E-04	-6.50E-04	1.95E-05	NA
197.042	0.1623	3.66E-06	-1.34E-04	3.38E-05	1.63E-05	NA
197.063	0.1722	2.43E-05	1.29E-03	-5.29E-04	1.14E-04	NA

197.083	0.1914	3.50E-05	1.35E-04	-2.97E-04	-7.52E-05	NA
197.104	0.2013	1.71E-05	-6.73E-04	4.75E-04	2.99E-05	NA
197.125	0.1903	2.56E-06	1.90E-04	-1.43E-04	3.02E-05	NA
197.146	0.1996	1.50E-05	-2.61E-04	-1.39E-04	3.68E-05	NA
197.167	0.2093	5.53E-05	-1.68E-03	-6.87E-04	1.14E-04	NA
197.188	0.2136	2.27E-05	-4.66E-04	-4.73E-04	4.37E-05	NA
197.208	0.2110	5.32E-06	5.26E-04	-4.81E-04	7.27E-06	NA
197.229	0.2108	5.01E-06	2.29E-04	-3.08E-04	6.04E-05	NA
197.250	0.2050	7.59E-06	1.24E-04	-7.63E-04	4.12E-05	NA
197.271	0.2014	2.96E-06	9.64E-05	-5.65E-04	8.35E-05	NA
197.292	0.1997	1.23E-05	3.60E-04	3.07E-04	-3.64E-05	NA
197.313	0.1943	4.14E-06	5.67E-04	-4.45E-04	8.63E-05	NA
197.333	0.1931	3.42E-06	7.80E-04	-2.67E-04	9.07E-05	NA
197.354	0.1902	1.40E-06	1.66E-05	-3.88E-05	1.03E-05	NA
197.375	0.1909	2.49E-06	7.91E-05	3.21E-05	1.12E-05	NA
197.396	0.1916	2.10E-06	1.86E-04	1.23E-05	4.82E-05	NA
197.417	0.1921	1.45E-06	2.80E-04	-1.41E-04	-3.11E-06	NA
197.438	0.1926	1.25E-06	2.66E-04	-3.76E-04	1.46E-05	NA
197.458	0.1921	8.93E-07	1.35E-04	-1.22E-04	4.59E-06	NA
197.479	0.1902	1.31E-06	1.82E-04	-1.64E-04	1.94E-06	NA
197.500	0.1894	3.22E-06	3.87E-04	-3.73E-04	1.33E-05	NA
197.521	0.1790	8.75E-07	5.06E-04	-2.30E-04	1.23E-04	NA
197.542	0.1784	1.13E-06	6.24E-04	-4.60E-04	1.25E-04	NA
197.563	0.1780	1.78E-06	5.75E-04	-3.85E-04	1.36E-04	NA
197.583	0.1760	3.45E-06	7.16E-04	-7.16E-04	1.32E-04	NA
197.604	0.1728	1.02E-06	5.07E-04	-2.84E-04	1.15E-04	NA
197.625	0.1717	6.34E-07	3.58E-04	-2.20E-04	7.50E-05	NA
197.646	0.1738	1.14E-06	3.79E-04	-2.01E-04	4.26E-05	NA
197.667	0.1752	1.13E-06	4.68E-04	-3.69E-05	1.22E-04	NA
197.688	0.1758	1.24E-06	5.88E-04	-4.90E-04	7.28E-05	NA
197.708	0.1795	2.19E-06	3.31E-04	1.95E-05	1.31E-04	NA
197.729	0.1830	1.38E-06	4.61E-04	-1.66E-04	8.67E-05	NA
197.750	0.1843	1.56E-06	2.35E-04	-1.35E-04	4.49E-05	NA
197.771	0.1849	1.85E-06	2.81E-04	-2.09E-04	3.75E-05	NA
197.792	0.1855	1.71E-06	5.30E-04	-1.31E-06	1.13E-04	NA
197.813	0.1821	1.20E-06	1.44E-04	1.09E-04	1.07E-05	NA
197.833	0.1827	7.18E-07	3.23E-04	-1.79E-05	5.91E-05	NA
197.854	0.1828	1.00E-06	3.20E-04	8.23E-05	6.09E-05	NA
197.875	0.1833	8.44E-07	3.26E-04	-2.75E-05	7.37E-05	NA
197.896	0.1845	6.29E-07	6.90E-05	1.28E-04	1.73E-05	NA
197.917	0.1865	1.21E-06	2.17E-04	4.44E-05	2.80E-05	NA
197.938	0.1873	6.93E-07	2.53E-04	2.86E-05	6.09E-05	NA
197.958	0.1911	5.95E-06	-1.92E-04	8.11E-04	1.80E-04	NA
197.979	0.1948	1.90E-06	2.40E-05	1.76E-04	8.12E-05	NA
198.000	0.1972	1.18E-06	9.87E-05	3.91E-05	3.69E-05	NA
198.021	0.2008	4.58E-06	7.82E-04	2.75E-04	1.61E-04	NA
198.042	0.2075	4.92E-06	1.29E-04	1.96E-04	6.07E-05	NA
198.063	0.2106	8.66E-06	-4.30E-05	3.58E-04	2.26E-05	NA
198.083	0.2112	7.35E-06	1.26E-04	-2.85E-05	3.44E-05	NA
198.104	0.2154	1.07E-05	-1.87E-04	6.19E-04	6.55E-05	NA
198.125	0.2134	1.54E-05	-8.93E-04	1.99E-03	-5.14E-05	NA
198.146	0.2181	1.69E-05	-6.85E-04	5.21E-04	-6.54E-05	NA
198.167	0.2319	4.67E-05	2.80E-04	4.31E-04	1.37E-05	NA
198.188	0.2441	1.12E-05	-4.81E-05	2.75E-04	1.05E-05	NA
198.208	0.2650	8.50E-05	-2.89E-04	1.03E-03	8.46E-05	NA

Table F.4: Period-by-period mean, standard deviation, and covariances with the three wind components (u, v, w) of sonic temperature (T_s), and mean pressure ($\overline{P}$).

Julian Day	$\overline{T_s}$ [K]	$\overline{\sigma_{T_s}}$ [K]	$\overline{u'T_s'}$ [K m s^{-1}]	$\overline{v'T_s'}$ [K m s^{-1}]	$\overline{w'T_s'}$ [K m s^{-1}]	$\overline{P}$ [kPa]
193.417	295.136	0.3211	0.0090	0.0712	0.0402	96.975
193.438	295.809	0.3978	0.0215	0.1256	0.0444	96.994
193.458	296.250	0.2872	0.0395	0.0037	0.0495	97.000
193.479	296.623	0.2827	0.0564	-0.0156	0.0567	96.992
193.500	297.096	0.3315	0.0749	-0.0132	0.0620	96.998
193.521	297.332	0.3590	0.0573	-0.0215	0.0696	97.006
193.542	297.715	0.3065	0.0155	0.0531	0.0422	96.995
193.563	298.077	0.2576	-0.0065	0.0140	0.0197	96.973
193.583	298.326	0.2514	-0.0188	0.0647	0.0458	96.951
193.604	298.722	0.2227	-0.0151	-0.0440	0.0329	96.934
193.625	299.567	0.2694	0.0594	0.0417	0.0556	96.925
193.646	299.723	0.2252	0.0057	0.0134	0.0278	96.914
193.667	300.205	0.2895	0.0725	0.0549	0.0462	96.883
193.688	300.664	0.2987	-0.0228	0.1231	0.0369	96.848
193.708	301.233	0.2852	-0.0204	0.0983	0.0449	96.815
193.729	301.665	0.2894	-0.0195	0.0166	0.0431	96.786
193.750	302.071	0.2840	-0.0378	0.0547	0.0392	96.766
193.771	302.403	0.2327	-0.0385	0.0019	0.0299	96.735
193.792	302.654	0.1749	-0.0135	-0.0303	0.0209	96.711
193.813	302.969	0.1673	-0.0562	-0.0558	0.0160	96.704
193.833	303.132	0.1454	0.0042	0.0070	0.0184	96.697
193.854	302.722	0.3191	0.2740	0.3589	0.0044	96.705
193.875	302.077	0.1410	-0.0434	-0.0394	0.0098	96.722
193.896	301.534	0.1997	-0.0701	-0.0113	0.0079	96.745
193.917	300.709	0.2230	-0.0231	-0.0265	0.0092	96.760
193.938	300.015	0.2128	-0.0295	-0.0084	0.0061	96.784
193.958	299.052	0.4351	0.0231	0.0435	0.0245	96.800
193.979	297.984	0.2007	0.0169	0.0396	0.0119	96.811
194.000	297.464	0.3290	0.1578	0.0214	0.0121	96.832
194.021	296.196	0.5368	0.2789	0.1553	0.0324	96.849
194.042	295.084	0.2793	0.0996	0.0064	0.0151	96.857
194.063	294.085	0.2902	-0.0172	-0.0688	0.0127	96.860
194.083	293.731	0.1631	-0.0306	-0.0323	-0.0031	96.885
194.104	294.152	0.4882	-0.0505	-0.2011	0.0003	96.905
194.125	294.331	0.4383	-0.1429	0.3443	-0.0077	96.932
194.146	293.431	0.2879	0.0498	-0.0827	0.0053	96.934
194.167	293.308	0.4703	0.1966	-0.0264	0.0061	96.921
194.188	291.837	0.3187	0.0754	-0.1033	0.0092	96.946
194.208	291.359	0.2062	-0.0422	-0.0112	-0.0015	96.970
194.229	290.710	0.3160	0.0291	-0.0047	0.0025	97.016
194.250	289.827	0.5013	0.1940	0.1182	0.0094	97.024
194.271	289.792	0.3262	0.1338	0.0009	0.0224	97.036
194.292	290.506	0.3348	0.0419	0.1554	0.0255	97.052
194.313	290.474	0.2347	0.0003	-0.0377	0.0286	97.056
194.333	290.311	0.2621	-0.0027	-0.0113	0.0281	97.048
194.354	290.740	0.3638	0.0329	-0.0411	0.0568	97.050
194.375	290.945	0.4194	-0.0824	0.1172	0.0721	97.051
194.396	290.931	0.4602	-0.1368	0.0647	0.0759	97.050
194.438	293.102	0.4696	0.0360	0.0939	0.1017	97.024
194.500	295.479	0.4367	0.0619	0.0975	0.0910	96.948
194.521	296.228	0.7109	-0.0352	0.7523	0.1572	96.877
194.542	297.276	0.3584	0.0024	-0.0935	0.0663	96.842

194.563	297.949	0.6891	0.0767	0.0662	0.1672	96.816
194.583	298.966	0.7742	-0.0372	0.1055	0.1639	96.784
194.646	301.005	0.5183	0.0323	0.0361	0.1146	96.711
194.667	301.731	0.3679	0.2288	0.2408	0.0879	96.682
194.688	301.774	0.3588	0.1885	0.4393	0.0684	96.685
194.708	301.361	0.3046	0.0583	0.2746	0.0460	96.699
194.729	301.127	0.2540	-0.0033	0.1915	0.0407	96.736
194.750	300.759	0.2266	0.0065	0.1424	0.0453	96.765
194.771	300.644	0.3055	0.5196	0.2057	0.0582	96.784
194.792	299.823	0.4197	0.3566	0.3349	0.0542	96.826
194.813	298.519	0.4277	0.2354	-0.2239	0.0856	96.918
194.833	297.032	0.5212	0.0611	-0.0379	0.0202	97.030
194.854	295.724	0.4280	-0.0350	-0.0035	0.0332	97.109
194.875	294.632	0.4307	0.0476	-0.0085	0.0203	97.181
194.896	293.761	0.3245	0.0192	-0.1253	0.0181	97.237
194.917	292.759	0.2168	-0.0709	0.0203	-0.0094	97.308
194.938	292.326	0.1292	-0.0218	-0.0020	-0.0018	97.360
194.958	291.804	0.2144	-0.0012	-0.0019	0.0075	97.405
194.979	291.340	0.1578	0.0064	0.0009	0.0049	97.442
195.000	291.089	0.1727	0.0041	-0.0014	0.0088	97.451
195.021	290.619	0.1785	0.0175	-0.0062	0.0110	97.496
195.042	290.355	0.1870	0.0177	0.0190	0.0215	97.513
195.063	289.933	0.2767	0.0182	-0.0168	0.0270	97.548
195.083	289.374	0.4026	-0.0926	0.1173	0.0160	97.567
195.104	288.185	0.6100	-0.0481	0.3609	0.0559	97.577
195.125	287.581	0.3639	-0.0175	0.0938	0.0616	97.589
195.146	287.551	0.3954	0.0220	-0.0075	0.0526	97.613
195.167	286.806	0.3262	0.0185	-0.0201	0.0425	97.640
195.188	286.484	0.3662	-0.0163	0.0889	0.0589	97.652
195.208	286.465	0.3787	-0.0310	0.0347	0.0592	97.652
195.229	285.610	0.5564	-0.0283	0.0636	0.0671	97.668
195.250	285.342	0.4177	0.0274	0.0667	0.0614	97.685
195.271	285.626	0.4892	0.0857	0.0155	0.0486	97.709
195.292	285.325	0.4540	0.0425	0.0791	0.0769	97.725
195.313	285.070	0.3982	0.0016	0.0789	0.0662	97.755
195.333	285.556	0.4329	0.0600	0.1537	0.0563	97.780
195.354	286.516	0.4535	0.0970	0.0939	0.0660	97.809
195.375	287.531	0.4442	-0.0540	0.0175	0.0675	97.816
195.396	288.402	0.4994	0.0842	0.0372	0.0727	97.828
195.417	289.896	0.6239	0.1074	-0.1644	0.0862	97.839
195.438	291.324	0.5206	-0.1199	0.1205	0.0652	97.843
195.458	292.515	0.4680	-0.0947	0.0878	0.0428	97.832
195.479	293.511	0.4652	-0.2083	0.0323	0.0742	97.825
195.500	293.767	0.3242	0.0407	0.0830	0.0456	97.811
195.521	294.049	0.3576	-0.0012	0.2165	0.0550	97.797
195.542	294.560	0.3556	-0.0885	-0.0444	0.0563	97.784
195.563	295.081	0.3820	0.0321	0.1088	0.0590	97.764
195.583	295.571	0.4024	0.1239	-0.0979	0.0876	97.746
195.604	295.933	0.3745	-0.0991	0.2145	0.0642	97.731
195.625	296.180	0.3363	0.0050	0.1315	0.0536	97.714
195.646	296.413	0.3131	0.0636	0.1558	0.0558	97.697
195.667	296.910	0.3768	-0.0418	-0.1844	0.0543	97.678
195.688	297.273	0.3466	0.0124	-0.0018	0.0429	97.659
195.708	297.502	0.2931	0.0026	0.0921	0.0335	97.634
195.729	297.550	0.2068	0.0381	0.0101	0.0305	97.608
195.750	297.770	0.2311	0.0201	0.1297	0.0223	97.589
195.771	297.853	0.2283	0.0129	0.1258	0.0151	97.583
195.792	297.828	0.1662	0.0222	0.0154	0.0237	97.582
195.813	297.910	0.1800	0.0035	0.0190	0.0190	97.567
195.833	297.905	0.1338	0.0040	0.0047	0.0133	97.556

195.854	297.896	0.1101	-0.0166	-0.0013	0.0097	97.551
195.875	297.763	0.2050	-0.1032	-0.0313	0.0071	97.550
195.896	297.107	0.2517	0.0247	-0.0662	-0.0021	97.560
195.917	296.276	0.1456	0.0245	0.0007	0.0008	97.563
195.938	296.073	0.1885	-0.0374	-0.0159	-0.0044	97.569
195.958	294.967	0.3327	-0.0980	0.0377	-0.0067	97.577
195.979	294.260	0.2398	0.0358	0.0019	-0.0035	97.566
196.000	293.760	0.3454	0.0498	-0.0221	0.0023	97.564
196.021	292.990	0.3253	-0.0989	0.1204	-0.0028	97.570
196.042	292.135	0.2549	0.0203	-0.0131	0.0015	97.567
196.063	292.171	0.2116	0.0301	-0.0067	0.0052	97.557
196.083	291.562	0.2201	-0.0692	-0.0013	0.0041	97.539
196.104	290.926	0.1403	-0.0249	-0.0068	-0.0016	97.530
196.125	291.147	0.2435	0.0535	0.0298	0.0342	97.533
196.146	290.981	0.2029	0.0502	0.0156	0.0159	97.529
196.167	290.490	0.5295	1.0183	0.2099	0.0805	97.521
196.188	290.670	0.1453	0.0035	0.0348	0.0064	97.520
196.208	289.943	0.1781	-0.0620	-0.0749	-0.0061	97.506
196.229	289.536	0.2119	-0.0318	0.0256	0.0117	97.503
196.250	289.163	0.2153	-0.0126	0.0029	0.0140	97.503
196.271	288.601	0.2497	-0.0987	-0.0066	0.0138	97.481
196.292	288.464	0.2208	-0.0520	-0.0173	0.0260	97.467
196.313	288.315	0.2070	-0.0290	0.0033	0.0259	97.472
196.333	288.594	0.3466	-0.0209	0.0228	0.0532	97.474
196.354	289.286	0.4207	-0.1525	-0.0071	0.0441	97.463
196.375	290.285	0.5480	-0.0006	0.1852	0.0983	97.458
196.396	291.503	0.5810	-0.1205	-0.0673	0.1008	97.450
196.417	292.375	0.5909	0.0283	-0.0351	0.1104	97.441
196.438	293.402	0.6777	-0.0005	-0.0063	0.1434	97.422
196.458	294.392	0.6518	-0.1632	0.0506	0.1309	97.404
196.479	295.929	0.8692	0.0594	-0.0181	0.2190	97.379
196.500	297.080	0.7648	-0.1128	0.1006	0.2018	97.363
196.521	298.195	0.7606	0.0602	-0.0522	0.2001	97.344
196.542	299.249	0.8119	0.0483	-0.0700	0.2260	97.317
196.563	299.800	0.7223	-0.1803	0.0508	0.1528	97.290
196.583	300.181	0.7812	-0.0390	0.3812	0.1992	97.259
196.604	300.567	0.7768	-0.1704	0.1204	0.2042	97.241
196.625	300.874	0.7516	-0.1163	0.0204	0.1797	97.213
196.646	301.171	0.7642	-0.0956	0.1553	0.1936	97.186
196.667	301.567	0.7402	-0.1746	-0.0046	0.2017	97.167
196.688	301.720	0.6552	-0.0842	0.0513	0.1683	97.144
196.708	302.012	0.6276	-0.1106	-0.0356	0.1554	97.127
196.729	302.102	0.5472	0.0020	-0.0062	0.1364	97.116
196.750	302.050	0.4881	0.0140	0.0137	0.1148	97.093
196.771	302.189	0.3702	-0.0086	0.0171	0.0835	97.078
196.792	302.279	0.3749	-0.0112	0.0223	0.0804	97.069
196.813	302.301	0.3102	-0.0336	0.0305	0.0551	97.069
196.833	301.991	0.1555	-0.0114	0.0204	0.0061	97.090
196.854	301.739	0.1053	0.0614	-0.0036	0.0029	97.093
196.875	301.599	0.0662	0.0012	-0.0051	-0.0005	97.102
196.896	301.458	0.1682	0.0531	-0.0363	0.0025	97.094
196.917	299.558	1.1272	0.8214	-0.0065	0.0228	97.082
196.938	297.718	0.2947	-0.1262	-0.0083	-0.0137	97.100
196.958	297.103	0.2629	-0.1747	0.0461	-0.0140	97.143
196.979	296.307	0.2296	0.0675	-0.0279	0.0023	97.176
197.000	295.645	0.2658	-0.0809	0.0192	-0.0055	97.169
197.021	295.083	0.2585	-0.0554	0.0930	-0.0050	97.170
197.042	294.398	0.2072	0.0125	-0.0105	-0.0045	97.181
197.063	293.562	0.2923	-0.1032	0.0195	-0.0087	97.180
197.083	293.017	0.1551	-0.0111	0.0136	-0.0023	97.176

197.104	292.635	0.1191	-0.0179	-0.0006	-0.0015	97.172
197.125	292.261	0.1577	0.0081	-0.0181	0.0037	97.180
197.146	291.848	0.0819	0.0084	-0.0006	0.0022	97.180
197.167	291.592	0.0857	0.0054	-0.0067	0.0020	97.184
197.188	291.399	0.1318	-0.0257	-0.0108	0.0036	97.187
197.208	291.092	0.0844	0.0205	-0.0164	0.0049	97.201
197.229	290.842	0.0993	0.0233	-0.0132	0.0081	97.228
197.250	290.456	0.1548	-0.0218	-0.0370	0.0041	97.239
197.271	290.175	0.0917	0.0240	-0.0146	0.0132	97.266
197.292	289.958	0.1270	0.0371	-0.0171	0.0173	97.287
197.313	289.753	0.1517	0.0701	-0.0390	0.0309	97.288
197.333	289.540	0.1612	0.0690	-0.0346	0.0263	97.297
197.354	289.426	0.1913	0.1212	-0.0740	0.0384	97.300
197.375	289.724	0.2555	0.1104	-0.0749	0.0536	97.324
197.396	289.904	0.2227	0.0944	-0.0235	0.0498	97.317
197.417	289.934	0.2444	0.1041	-0.0710	0.0520	97.348
197.438	289.975	0.3081	0.1585	-0.0540	0.0814	97.348
197.458	289.985	0.3353	0.1876	-0.0787	0.0863	97.377
197.479	290.361	0.3723	0.1414	-0.0069	0.0822	97.385
197.500	290.702	0.3112	0.1539	-0.0778	0.0804	97.384
197.521	291.092	0.2909	0.1621	-0.0618	0.0697	97.389
197.542	291.654	0.3137	0.1732	-0.1478	0.0638	97.405
197.563	292.060	0.2445	0.1063	-0.0445	0.0578	97.408
197.583	292.698	0.3197	0.1797	-0.0822	0.0770	97.401
197.604	293.366	0.3762	0.2423	-0.1848	0.0761	97.392
197.625	293.969	0.3856	0.2575	-0.0428	0.1221	97.394
197.646	293.940	0.3624	0.2000	-0.0069	0.1009	97.401
197.667	294.123	0.3553	0.2139	-0.0397	0.1022	97.402
197.688	294.276	0.3019	0.1846	-0.1024	0.0704	97.384
197.708	294.568	0.2797	0.1342	-0.0102	0.0798	97.401
197.729	294.798	0.2568	0.1364	-0.0293	0.0619	97.404
197.750	294.930	0.2237	0.1000	-0.0039	0.0535	97.410
197.771	295.064	0.1825	0.0888	-0.0108	0.0421	97.402
197.792	295.271	0.1637	0.0515	-0.0071	0.0257	97.395
197.813	295.170	0.1768	0.0406	0.0002	0.0159	97.396
197.833	294.751	0.1824	0.0565	-0.0159	0.0192	97.385
197.854	294.400	0.1685	0.0368	0.0111	0.0076	97.386
197.875	294.067	0.1437	0.0024	0.0007	0.0069	97.396
197.896	293.631	0.1303	0.0161	-0.0276	0.0072	97.409
197.917	293.261	0.1188	-0.0138	-0.0009	0.0010	97.420
197.938	292.861	0.1010	0.0085	-0.0057	-0.0045	97.434
197.958	292.627	0.0585	-0.0022	-0.0014	-0.0025	97.425
197.979	292.340	0.1547	-0.0137	0.0312	0.0011	97.427
198.000	291.883	0.1729	0.0038	0.0305	0.0042	97.424
198.021	291.427	0.1435	-0.0579	-0.0121	-0.0126	97.421
198.042	291.401	0.1816	-0.0419	0.0389	-0.0065	97.417
198.063	291.262	0.3322	-0.1334	0.1071	-0.0161	97.413
198.083	290.726	0.2183	-0.0139	0.0219	-0.0044	97.416
198.104	290.597	0.1752	-0.0307	0.0572	-0.0007	97.394
198.125	290.022	0.3687	-0.1005	0.1927	-0.0022	97.402
198.146	289.720	0.2146	-0.0362	0.0321	-0.0095	97.392
198.167	289.766	0.1417	-0.0165	0.0087	-0.0038	97.392
198.188	289.583	0.1472	-0.0095	-0.0148	-0.0046	97.404
198.208	289.658	0.1803	-0.0081	0.0222	0.0001	97.412